Characterisation and modeling of precipitation kinetics and yield strength in variously treated 7000-series aluminum alloys

by

Negar Baghbanaghaie

A thesis
presented to the University of Waterloo
in fulfilment of the
thesis requirement for the degree of
Master of Applied Science
in
Mechanical and Mechatronics Engineering

Waterloo, Ontario, Canada, 2021

Author's declaration

I hereby declare that I am the sole author of this thesis. This is a true copy of the thesis, including any required final revisions, as accepted by my examiners.

I understand that my thesis may be made electronically available to the public.

Abstract

This thesis investigates the effects of: (a) various aging practices, and (b) deformation during a warm-forming cycle, on the precipitation hardening response and aging kinetics of AA7050 and AA7075, respectively. The investigations were conducted through an extensive experimental study and analytical modeling techniques.

Two heat treatment routes were examined for AA7050: direct and multi-step aging. The direct aging considered exposing the as-quenched samples to temperatures of 150 and 177°C until the peak aged condition is achieved. The multi-step aging considered pre-aging of the as-quenched samples at 100°C for 4 hours, followed by final aging at 150 and 177°C until the peak-aged condition is identified. The precipitation behaviour and the mechanical properties of the as-quenched and pre-aged alloys were evaluated through differential scanning calorimetry (DSC) and hardness measurements. The comparative study of the DSC results showed that three precipitates, namely GP zones, η', and η precipitates, are the main precipitates that are formed during the considered artificial aging process routes. The combination of GP zones and η' precipitates were suggested to be responsible for the maximum hardening at the peak aged condition. It was found that the material hardness is improved by conducting a pre-aging treatment before the final artificial aging process. This behavior was related to the formation of fine and closely-spaced GP zones during the pre-aging process which are beneficial for accelerated nucleation of higher amounts of η' during the final artificial aging. The kinetics of precipitation were determined by conducting isothermal calorimetry (IC) experiments in the range of 135 to 190°C.

Two thermal processing histories were studied for AA7075, starting with a pre-aging (PA) treatment, followed by either (a) final aging, or (b) warm forming of the pre-aged material (PA+WF), followed by final aging. In both cases, the final aging was performed at a typical automotive paint bake temperature, *i.e.* 177°C. The warm forming process for the PA+WF case was represented as a strain to 0.1 at a temperature of 150°C. The effect of deformation on the precipitation hardening response of the multi-step aged alloy was investigated by performing DSC and hardness tests on the PA and PA+WF materials. The combination of the hardness and calorimetry results suggested the potential dissolution of some pre-aging GP zones during the warm-forming stage which increases the solid solution hardening contribution in the as-

deformed material. It was found that the hardness of the PA+WF material following final aging at 177°C is always higher than that of the PA material. It was proposed that this result can be due to strain hardening as well as the improvement in precipitation hardening in the presence of dislocations.

The precipitation kinetics for the two processing histories were experimentally analysed through IC tests considering three temperatures (*i.e.* 150, 165 and 177°C). The results showed similar peak aging times (t_f values) for final aging of the deformed *versus* non-deformed materials for each of the final aging temperatures. The IC results were consistent with the hardness measurements which showed that the peak hardening for both deformed and non-deformed materials is achieved after 1 hour of aging at 177°C. It is suggested that this similarity in the peak aging time can be due to the offsetting factors that control the precipitation rate: (i) the presence of dislocations as well as the GP zone dissolution occurring during the WF stage (which increases the matrix supersaturation), both of which will tend to increase the precipitation rate; while, (ii) annihilation of vacancies by dislocations is likely operative and is expected to decrease the rate of precipitation in the PA+WF material.

The measured kinetics and yield strength data for AA7050 was integrated within the models developed by Esmaeili [1], [2] to predict the precipitation behaviour for a broad range of aging histories. In order to expand the range of applicability of the yield strength predictions, in particular for a weak obstacle assumption, a new model was developed and validated that predicts the evolution of precipitate radius during concurrent nucleation and growth of precipitates.

To simulate warm forming processes, the existing kinetic model due to Esmaeili [2] was extended to account for the effect of deformation on the precipitation kinetics. The improved kinetic model incorporates a theoretical description of the effect of dislocation core diffusion on the precipitation kinetics. In this respect, a simple relationship was also introduced to predict the dislocation density as a function of the imposed plastic strain. Finally, the yield strength evolution during multi-step aging processes coupled with an intermediate warm-forming stage was predicted, accounting for the summation of the precipitation and strain hardening strengthening mechanisms.

The combined experimental and modeling results from the present work contribute to the area of process modeling of aluminum alloys for artificial aging with or without a deformation cycle. The work advances the understanding of the process-property-relationships for 7000-series aluminum alloys and provides a basis for industrial process and property optimization.

Acknowledgement

First and foremost, I would like to express my sincere gratitude and appreciation to my patient and supportive supervisor, Prof. Shahrzad Esmaeili, for her endless support, guidance, enthusiasm, and encouragement throughout this research project. Her productive suggestions, invaluable advice, and deep insights in this field helped me tremendously in all the time of research and writing this thesis. I would also like to thank my co-supervisor, Prof. Michael Worswick, for giving me the great opportunity to be part of his group and to work on this project. I truly appreciate his patience, understanding, unrelenting support and inspiring supervision which made possible the successful completion of this thesis. Thank you both for teaching me and inspiring me throughout this research. Working with you has been a great honor for me.

I would like to thank my committee, Prof. Adrian Gerlich and Prof. Kaan Inal for their valuable feedback. I highly appreciate their time and effort in reading my thesis.

I would like to extend my deepest acknowledgement to the project supporting organizations: Honda R&D Americas Inc., Arconic Ground Transportation Group, Promatek Research Centre, the Natural Sciences and Engineering Research Council (NSERC), the Canada Foundation for Innovation, the Ontario Research Fund, the Ontario Centres of Excellence, the Ontario Advanced Manufacturing Consortium.

I would like to thank Professor Alexis Deschamps for kindly sharing his SAXS results on AA7030 alloy to help me validate my modeling work. I really appreciate your help and support.

Many thanks to another PhD student and my true friend, Atekeh Abolhasani, for her wonderful help, contributions, and trainings from the first day of my master's program to the final thesis writing. Her advice and consultation are greatly appreciated. I would like to thank Hossein Pishyar, for being a helpful and great teammate who has generously helped me with my warm-forming experiments. Also, thanks to Mark Whitney, Dr. Massimo Di Ciano and Sante DiCecco for their help and assistance particularly during my early days of working as a student.

A special thanks to the lab technologists: Eckhard Budziarek and Tom Gawel, as well as Research Associates Ryan George, Amir Zhumagulov and Dr. José Imbert-Boyd, for their precious help and support.

I would like to thank my friends and colleagues: Dr. Pedram Samadian, Steven Lee, Dr. Tamjeed Rahman, Raphael Boulis, Farinaz Jeyranpourkhameneh, Farzad Sharifpour, Dr. Zohreh Asaee, Dr. Armin Abedini, ChiHsiang-Liao, and the rest who are too many to name, for their friendship and willingness to help.

A big shout-out goes to my dear friends: Jacqueline Noder, Katayoon Taherkhani and Niloufar Eftekhari for their presence and support - Thank you so much for going through these two years together!

The last but the most, I would like to extend my deepest appreciation to my family. I am greatly thankful to my dear brother, Amirmohamad, for always being there for me. There are no words to express my sincere gratitude for my parents, Saeedeh and Mohsen, who were and still are the reason behind my achievements. Their continuous and unconditional love, trust, support, prayers, encouragement, and efforts are things I can never pay back.

Finally, I owe an immense gratitude to my husband, Alireza Mohamadizadeh, for his valuable discussions and comments during my research. His unparalleled love, endless supports and constant trust are deeply appreciated. Thank you so much for believing in me and standing by my side during the tough times, from start to end.

Dedication

To My family

Table of Contents

List of Figures

List of Tables

1. Introduction

7000-series aluminum alloys are used for structural applications in the aerospace industry and have a wide range of potential applications in the automotive sector due to their combination of high strength, toughness, light weight and corrosion resistance [3]–[5]. Most of these properties can be controlled through a combination of appropriate processing and alloying. The high strength of the 7000-series aluminum alloys is commonly obtained by a fine distribution of precipitates promoted by appropriate thermal processing that usually consists of multi-step aging treatment [6].

A common thermal processing used in automotive industries is paint-bake cycling [2] which results in simultaneous curing of the paint and increasing the strength of the panels. However, the paint-bake response of aluminum alloys has been significantly enhanced by the application of commercial pre-aging processes [2], [7]–[9].

An important challenge in utilizing 7000-series aluminum alloys is their poor formability at room temperature [10]. To overcome this limitation, W-temper forming (*i.e.* forming shortly after quenching) and die quenching (*i.e.* forming during quenching) have been proposed [11]. However, the economic feasibility of both processes is limited by the requirement of solution heat treatment immediately prior to the deformation as well as the complexity and cost of the die quenching tooling and material handling. An alternative process to W-temper forming and die-quenching is the warm-forming process [12], [13]. Reportedly, the heat treatment of the 7000-series aluminum alloys usually consists of multi-step aging, coupled with various degrees of plastic deformation [4]. The influence of strain on the precipitation process has been analysed by many authors [14]–[17]. Indeed, the presence of dislocations due to the plastic deformation can alter the precipitation process in various ways. In alloys where homogenous nucleation of hardening precipitates is difficult, a plastic deformation step can enhance the hardening response by promoting the heterogenous nucleation of precipitates on dislocations. However, in some 7000-series alloys in which the precipitates that nucleate on dislocations are not the most efficient at strengthening, the presence of dislocations may decrease the hardening response of the alloys [15], [16].

Upon warm forming of an under-aged alloy, the straining and precipitation processes occur together, leading to a complicated dynamic microstructural transformation. In such cases, the effect of plastic deformation on the precipitation process involves a balance between possible mechanisms: acceleration of nucleation in presence of dislocations [18], acceleration of precipitate growth or coarsening due to solute transport toward the dislocations and pipe diffusion [19], and partial or complete precipitate dissolution due to shearing by dislocations [20]. Moreover, dislocations can also act as vacancy sinks. Due to the important role of the vacancy concentration in the precipitation process in 7000-series aluminum alloys, the presence of dislocations can influence a large volume of the material around them [16]. Considering these various possible interactions, the effect of the presence of dislocations on the precipitation process and mechanical properties strongly depends on the conditions used for thermal processing, matrix supersaturation, precipitate type and morphology, and the characteristics of the applied strain (strain level, strain rate and forming temperature).

One part of the present work focuses on characterizing the effects of various aging routes, *i.e.* direct or multi-step aging practices, on the precipitation hardening response of AA7050 aluminum alloy sheet through a comprehensive modeling-experiment approach. This part of the work aims at modeling the evolution of precipitate size during artificial aging and expanding the applicability of a previously developed yield strength model [1].

The present study also examines the effects of a processing sequence comprising pre-aging, warm-forming and subsequent aging at temperatures typical of paint bake cycling (PBC) on the precipitation hardening response and aging kinetics of AA7075. In particular, the work aims to (i) characterize precipitation hardening behaviour in the presence of dislocations induced during warm forming through experimental methods; and (ii) expand the viability of a previously developed precipitation hardening model by including the effects of dislocations on the precipitation kinetics and strengthening. The model is then implemented for AA7075 to predict the evolution of yield strength of the pre-aged and warm-formed alloy during aging at PBC temperatures.

2. Literature review

In this chapter, the strengthening mechanisms of aluminum alloys will be briefly reviewed. Then, an overview of previous studies on the precipitation hardening behaviour in 7000-series aluminum alloys, which is the main focus of the current work, will be presented. The precipitation sequence and transitions in 7000-series aluminum alloys, the effects of various aging routes and the effect of deformation on the precipitation hardening response of 7000-series alloys will be reviewed next. Finally, a summary of the relevant modeling approaches used by previous authors to predict the precipitation kinetics and the yield strength evolution during aging will be presented.

2.1. Strengthening mechanisms

It is well known that when a crystalline material is mechanically stressed beyond its yield strength, a large number of dislocations are generated in the material. The movement and multiplication of dislocations allows plastic deformation to occur [21]. The material's response to the dislocation movement determines its strength. The common strengthening mechanisms are explained in the following sections:

Grain size effect

It is generally believed that the grain boundaries act as barriers to dislocation motion. In fact, moving dislocations pile-up at grain boundaries. So, the stress required for their motion to continue across the grain boundary must exceed a critical stress value [21], [22]. It is well known that in fine-grained materials a larger applied stress is required to cause slip than that in large-grained materials [22]. Accordingly, the Hall-Petch relationship was found by empirical curve fitting to yield strength versus grain size data. According to the Hall-Petch relationship [22], [23], *i.e.* Eq. (2.1), an increase in the grain size (which reduces the total density of grain boundaries), has an adverse effect on strengthening in aluminum alloys:

$$\sigma_y = \sigma_i + k_1 D^{-1/2} \qquad (2.1)$$

in which σ_y is the yield strength, σ_i is the frictional stress of the lattice, D is the grain diameter and k_1 is constant for a given alloy system. It is reported that k_1 is approximately $0.22\,\frac{MPa}{\sqrt{m}}$ for 7000-series aluminum alloys [24]. According to the previous studies, grain-size strengthening is not very strong in aluminum alloys due to the small value of k_1 which is approximately five times smaller than that in ferrous alloys. However, the effects of grain size on strengthening of aluminum alloys can become important at very fine grain sizes [23], [25].

Solid solution strengthening

Solid solution strengthening occurs due to the differences in atomic size or elastic modulus between the solute and matrix atoms [23]. The contribution from the solid solution to the yield strength is given as [1], [26]:

$$\sigma_{ss} = \alpha C^{2/3} \qquad (2.2)$$

in which α is a constant parameter related to size, modulus, and mismatch of the solute with Al matrix and C is the average solute concentration in the matrix.

Dislocation hardening

Forming operations can cause considerable hardening in aluminum alloys due to the increased dislocation density, ρ. This phenomenon is known as dislocation hardening (or strain hardening) which hinders the glide of dislocations due to the build up of the dislocation density in the material. The contribution of dislocation hardening to the yield strength is considered to be related to the square root of the dislocation density [27]:

$$\sigma_y = \sigma_i + k_2 \rho^{1/2} \qquad (2.3)$$

in which k_2 is constant for a given alloy system related to the shear modulus and the Burgers vector [5].

Precipitation hardening

Small second-phase particles distributed in a ductile matrix act as effective barriers to dislocation movement and therefore have a significant strengthening effect [21]. Due to the importance of precipitation hardening in the current work, this strengthening mechanism will be discussed in greater detail in the following section.

2.2. Precipitation hardening

Precipitation of hardening phases in aluminum alloys is a diffusion-controlled process and a thermally activated phenomenon. The process results in strengthening the material due to the formation of fine and closely-spaced precipitates within the matrix that impede dislocation motion [22]. Figure 2.1 outlines the general heat treatment process for precipitation (*i.e.* age) hardening of aluminum alloys. The process starts with a solution heat treatment stage to allow dissolution of the dissolvable second phase particles and to transform the matrix into a supersaturated solid solution [28]. During the solutionizing process, the alloy is heated up to a temperature above the solvus temperature to form a homogenous solid solution. As the solution heat treatment is completed, the alloy is quenched very quickly to room temperature to suppress any nucleation and precipitation on the potential nucleation sites. Following quenching, the supersaturated solid solution is generally unstable and thus will gradually (depending on the temperature) decompose into a more stable solid solution matrix and finely dispersed precipitates. Age hardening practices are usually conducted at intermediate temperatures, well below the solvus line, resulting in a controlled precipitation and desirably fine dispersion of second phases in the matrix that can act as effective obstacles to the dislocation movement [29].

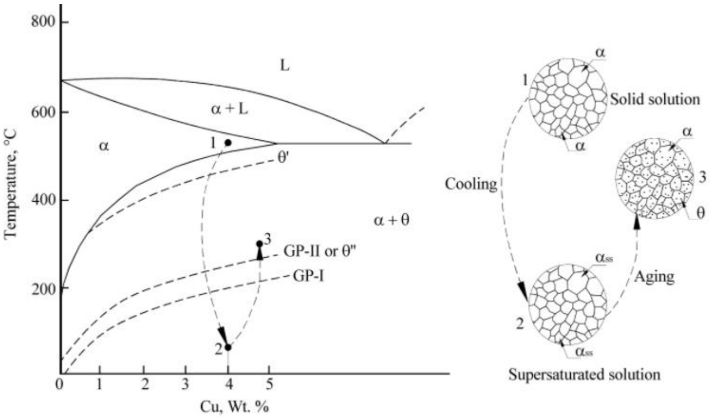

Figure 2.1. Aluminum rich Al-Cu phase diagram showing precipitation hardening process [29].

There are several mechanisms allowing a particle to hinder dislocation motion and thereby harden the material. Ardell [30] has outlined the following mechanisms: chemical strengthening, modulus strengthening, coherency strengthening, stacking fault strengthening and order strengthening. For some materials, only one of these mechanisms is active but for most materials several of these mechanisms are involved in determining the degree of strengthening.

It is observed that the critical stress at which the obstacles (precipitates) are overcome by dislocations highly depends on the nature of the obstacles, coherency, size, and their distribution in the matrix. When a gliding dislocation encounters an obstacle, it bows to some angle (see Figure 2.2) [30], [31].

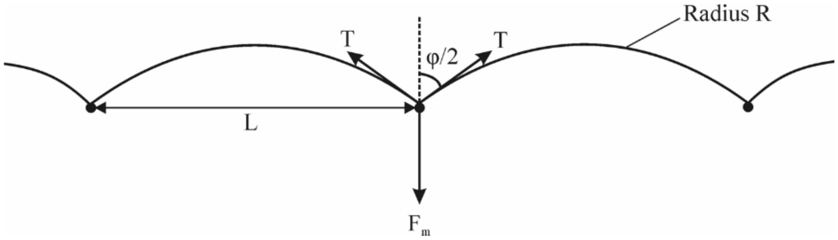

Figure 2.2. A dislocation line pinned by obstacles with a distance L apart [31].

As the applied stress increases, the bowing angle decreases until reaches a critical value φ_c when the obstacle is overcome, and the dislocation line is passed [32]. Based on a simple force balance, the obstacle strength will be [30], [32]:

$$F_m = 2T\,cos\left(\frac{\varphi_c}{2}\right) \qquad (2.4)$$

in which F_m is the obstacle strength, φ_c is the critical breaking angle and T is the dislocation line tension. Reportedly, when the bending angle is larger than 120°($\varphi > 120°$), F is small and the obstacle is classified as weak and shearable [1], [30], so it is more easily passed by dislocations through the cutting mechanism [1], [30] (see Figure 2.3 as an example of the cutting mechanism). It is reported that when the particles are small, closely spaced, and coherent, they can be cut by moving dislocations. In this case, the yield strength increases with increase in the volume fraction and size of the precipitates [33].

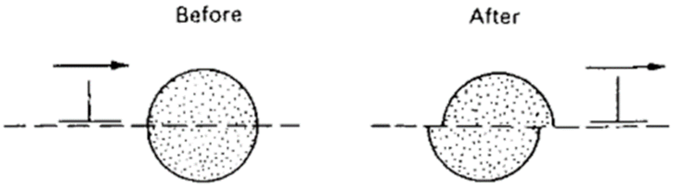

Figure 2.3. Dislocation motion continues through cutting mechanism [28].

On the other hand, for a smaller bending angle ($\varphi < 120°$), F is large and the obstacle is denoted as strong and shearable, but applies larger resistance to dislocation motion before being cut [29], [32]. Finally, if the bending angle equals to zero ($\varphi = 0$), the obstacle becomes non shearable and dislocations bypass the obstacle through the so-called Orowan mechanism (Figure 2.4) [28], [29], [32]. In presence of coarse and non-shearable precipitates, dislocations bulge in the spaces between the precipitates and bypass them. In this case, the strength decreases with increase in the particle radius [1].

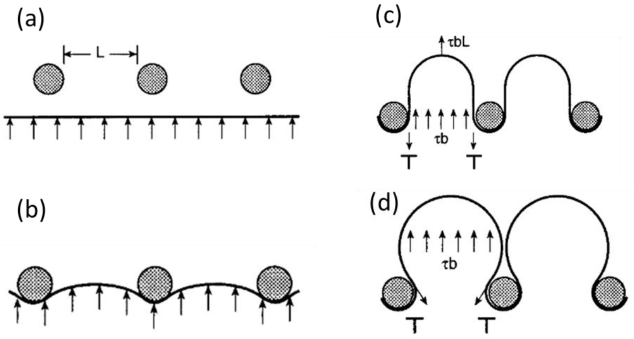

Figure 2.4. Dislocation meets hard and non-shearable obstacles: dislocation release at higher stresses occurs by Orowan looping [28].

2.3. Precipitation hardening in 7000-series aluminum alloys

2.3.1. Precipitation sequence

The precipitation sequence in 7000-series aluminum alloys has been subject of many studies using different methods of investigation such as: calorimetry tests, electrical resistivity, transmission electron microscopy, and X-ray methods [3], [34]–[37]. It has been found that the complex precipitation sequence and microstructural features are dependent on the alloy composition, solute content, Zn/Mg ratio, presence of impurities, solutionizing temperature, quench rate and aging path [38]. The following precipitation sequence has been reported in multiple references [3], [34], [39], [40]:

$$\text{Supersaturated solid solution} \rightarrow \text{GP zones} \rightarrow \text{metastable } \eta' \rightarrow \text{stable } \eta$$

Furthermore, it has been indicated that coherent GP zones and semi-coherent η' precipitates form to strengthen the alloy up to the peak aged condition while stable and incoherent η precipitates form during over-aging [3], [41].

GP zones are formed during natural aging at room temperature or during the early stages of artificial aging [41]. Two types of GP zones appear during the early stages of aging, GP I and GP II. The spherical GP I zones are formed for a wide temperature range from RT to 140-150°C and are independent of quenching temperature. Vacancy-rich clusters that transform to GP II zones are formed after quenching from a high temperature above 450 °C and upon aging at temperatures above 70°C [41], [42]. As indicated in Figure 2.5, there are two different routes for the formation of η′ precipitates. At higher aging temperatures (above the GP zones solvus), GP II zones transform to η′, whereas, GP I zones dissolve or transform into η′ if they grow past the critical size of dissolution [3]. Based on three-dimension atom probe investigations by Chen *et al.* [33] on an AA7055 alloy, the mechanism for transformation of GP I zones to η′ during aging can be as follows: Zn atoms diffuse from the matrix to small GP I zones to help them grow. During this process, GP I zones grow preferentially along certain directions to reduce the strain induced by atom diffusion. Then, another direction of growth may be activated. Therefore, small GP I zones develop into a two-dimensional structure and then transform into η′ phase [33]. η′ precipitate can be formed during aging at up to around 180-200°C before it is replaced by η equilibrium phase during the isothermal heat treatment [3]. The presence of Cu may introduce additional Cu-bearing precipitates, such as S or T phase depending on Cu content and ageing temperature [35].

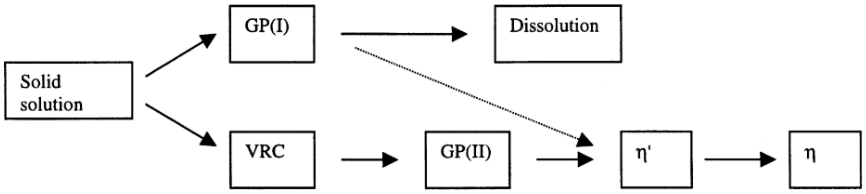

Figure 2.5. Sequence of precipitation in 7000-series aluminum alloys [3].

To have a better understanding of precipitate evolution and their effects on material properties for various aging practices, some pertinent studies are reviewed.

Li *et al.* [43] reported that, based on their high resolution electron microscopy (HRTEM) performed on a 7000-series aluminum alloy, coherent GP I and GP II zones are the main strengthening phases in the matrix after 7 hours of aging at 115°C (see Figure 2.6(a)). Reportedly, after further aging at 160°C for 12 hours, the microstructure of the alloy mainly consists of semi-coherent η' and incoherent η precipitates along with a small amount of GP II zones (see Figure 2.6 (b-d)).

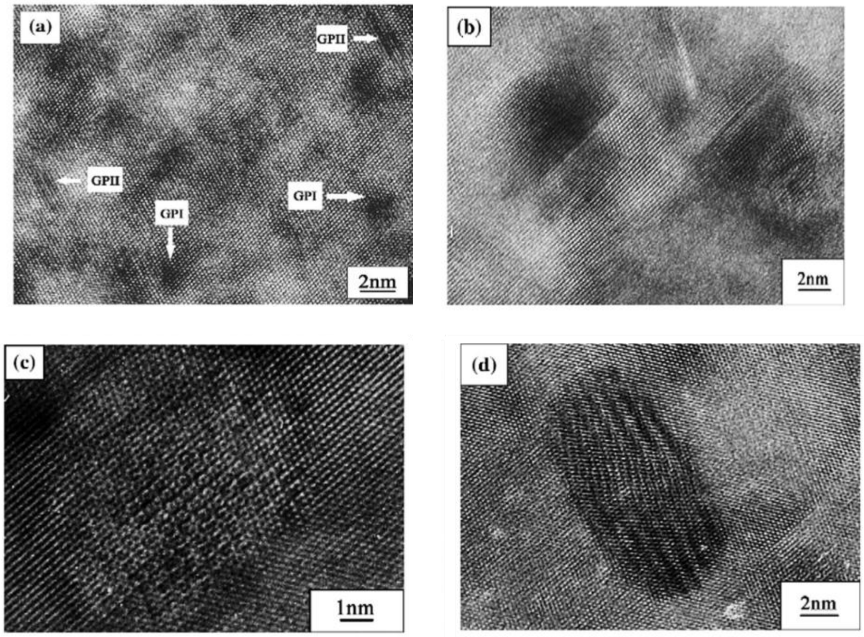

Figure 2.6. (a) GP I and GP II zones after aging for 7h at 115°C, (b) image of the GP II zones, (c)image of the semi-coherent η′ and (d) image of the incoherent η phase after ageing for 7h at 115°C plus 12h at 160 °C [43].

Rout *et al.* [38] investigated the age hardening response of an AA7017 alloy during aging at 120°C. Their results indicated that by increasing the aging time to about 24h (T6 state), the material hardness increased progressively and reached a maximum value which was attributed to the extensive formation of fine η′ precipitates. Subsequent reduction of the material strength occurred with the prolonged aging time (T7 state) which was reported to be due to the continued growth of η′ or transformation of the η′ precipitates to the stable η phase.

It is commonly accepted that increasing the aging temperature in the range that corresponds to the lower segment of the alloy’s TTT curves, accelerates the kinetics of precipitation [44]. According to the TTT diagram that was calculated for an AA7075 [45], the upper limits of that range for GP zones and η' precipitates are about 150°C and 325°C, respectively (See Figure 2.7).

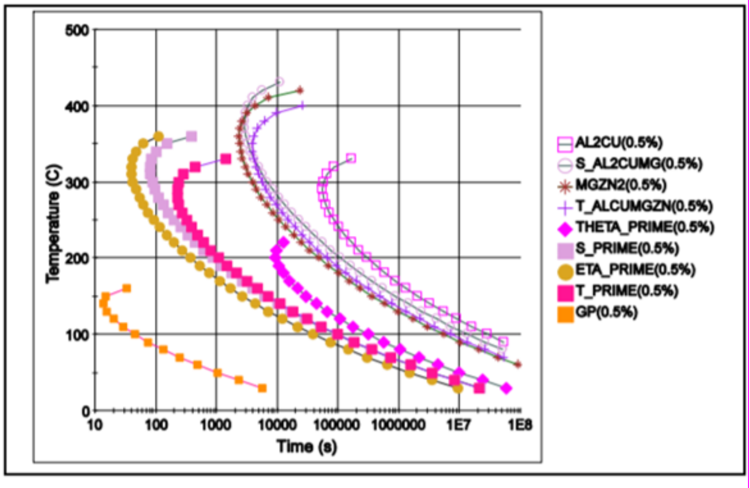

Figure 2.7. JMATPro calculated TTT curves for AA7075 [45].

Accordingly, the studies of Chen *et al.* [33] on an AA7055 alloy revealed that, the precipitation process is significantly promoted during aging at 160°C compared to 120°C. This observation was reported to be due to the rapid formation of small GP I zones as well as earlier formation of η′ during aging at 160°C compared to 120°C. They also reported that η′ can be easily transformed to η at higher temperatures such as 160°C. The earlier formation of coarse and incoherent η phase can induce over-aging to occur at shorter times.

2.3.2. Effects of aging practices on precipitation hardening

Although the kinetics of precipitation is slow at room temperature, it is well-known that natural aging (aging at RT) causes significant hardening in 7000-series aluminum alloys due to the formation of GP zones. Fuller *et al.* [46] reported that in an AA7050 alloy, the tensile and yield strengths increase continuously with natural aging time (see Figure 2.8). A similar result was also reported by Staley [47] for AA7075 and AA7050 alloys in which the yield strength continued to increase for up to 2 years of natural aging.

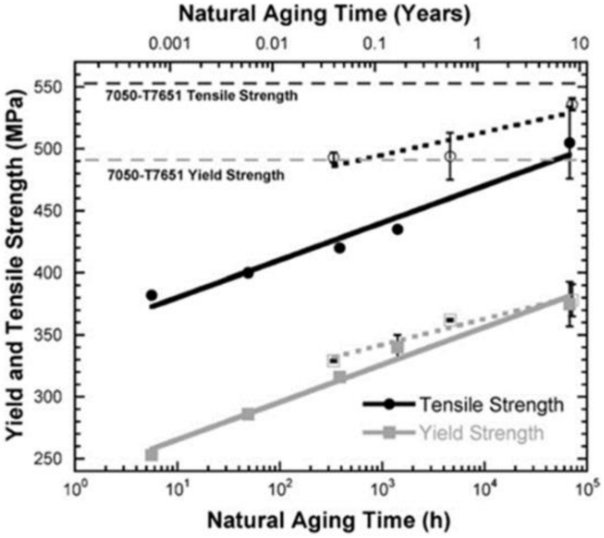

Figure 2.8. Tensile properties of naturally aged AA7050 samples [46].

In practice, keeping the alloys at room temperature between solution treatment and artificial ageing is usually inevitable. In some cases, it is reported that the formation of clusters/ GP zones during natural aging and possible dissolution of these precipitates during subsequent artificial aging can adversely affect the hardening potential of the alloys subjected to the initial natural aging step [48]. On the other hand, in some cases, the initial natural aging has positive effects on the hardening potential of the alloys [47]. According to Staley's analysis on AA7050 and AA7075 alloys [47], GP zones that are formed in the natural aging stage dissolve during a fast heating to the artificial aging temperature. However, if the heating rate is reduced, GP zones do not dissolve but grow during the heating process. The larger and more stable GP zones can act as nuclei for formation of strengthening η' precipitates, providing a larger volume fraction of strengthening particles which improves the strength of the material.

Despite the high strengthening potential of the age-hardenable alloys, in some cases processing factors, such as high temperature and short duration of artificial aging, impede the level of hardening that can be achieved. For example, for automotive body panel applications, aluminum alloys are typically held at RT after quenching and are artificially aged at 160-180°C for 20-60 min afterwards (referred to the paint bake treatment). Sometimes this aging time is not sufficient and, as a result, the precipitation-hardening potential of the alloy is not entirely exploited by the paint bake process. To broaden the application of the age-hardenable alloys and suppress the detrimental effect of natural aging, while improving the kinetics of precipitation and the hardening potential of the alloys, the aging procedures for 7000-series aluminum alloys usually consist of multi-step heat treatments [9]. Due to the multi-step aging practices, simultaneous improvement in the tensile properties, ductility and fracture toughness can be also achieved [35].

Investigations show that the improved precipitation hardening response of the alloys upon multi-step aging is due to modifications to the microstructure of the precipitates. It is reported that vacancy rich clusters or GP zones that are mostly formed during ageing at low temperatures (100-120°C), serve as nuclei or heterogenous nucleation sites for hardening precipitates during aging at higher temperatures which improves the paint bake response of the alloys [49].

Emani *et al.* [50] investigated the effect of pre-aging heat treatment on the artificial aging response of an AA7075 alloy by sequential aging at two temperatures of 121 and 177°C. As illustrated in Figure 2.9, single step aging at 121°C resulted in a hardness comparable to the hardness obtained by the multi-step aging. However, the kinetics of precipitation was accelerated in the later case. This kinetic improvement suggested that the lower total times associated with multi-step aging treatment can have a positive influence in energy savings and increased industrial productivity for the age-hardenable alloys.

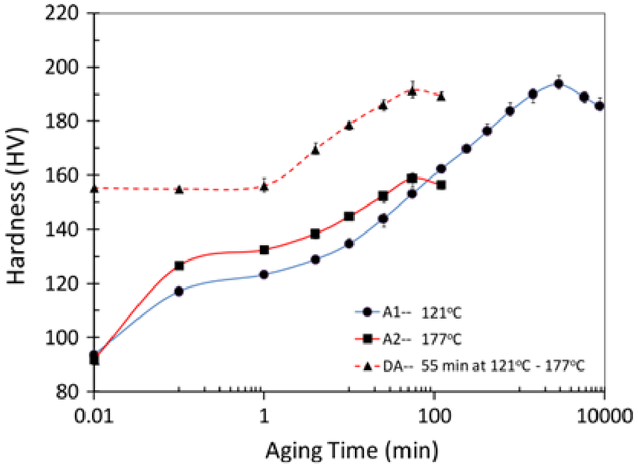

Figure 2.9. Effect of multi-step aging process on the hardness and kinetics of hardening of an AA7075 alloy [50].

Similar to Emani's investigation, Cao *et al.* [7] reported that by applying a pre-aging treatment (80°C/12h) before the final aging step at 180°C on an 7000-series aluminum alloy, a higher peak hardness value is achieved in a shorter time (Figure 2.10). Likewise, their TEM analysis showed a fine and uniform distribution of GP zones in the matrix after the pre-aging step (Figure 2.11 (a)) which had resulted in the formation of fine and equiaxed strengthening η' precipitates after the subsequent artificial aging process (the peak-aged condition (Figure 2.11 (b)). The precipitate microstructure (*i.e.* size and distribution) was reported to be responsible for the enhanced strengthening properties. In contrast, the microstructure of the peak-aged condition of the directly-aged alloy (Figure 2.11 (c)) consisted of coarse needle/lath-like precipitates which were shown to be less effective in hardening improvement [7].

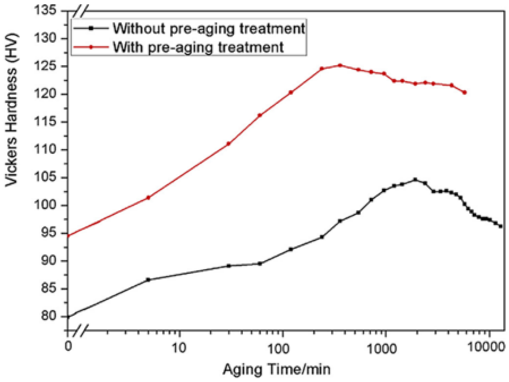

Figure 2.10. Improved age-hardening response of the alloy due to the pre-aging treatment [7].

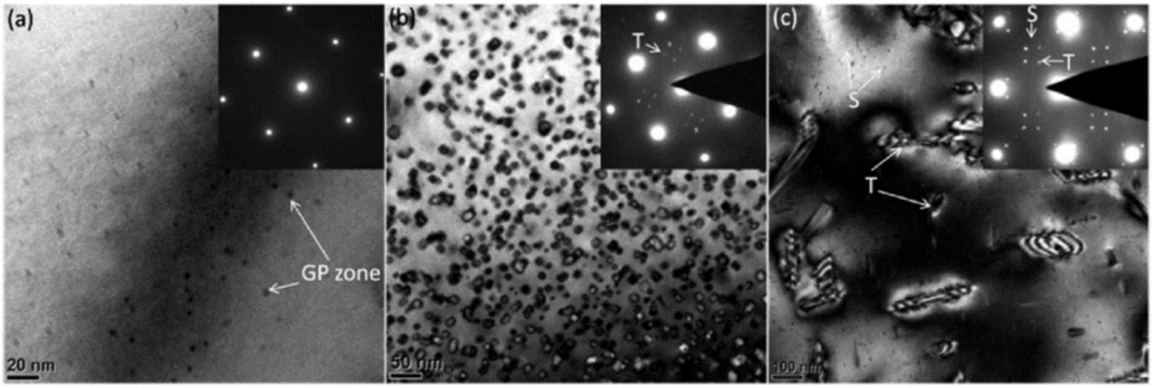

Figure 2.11. TEM images and SAED patterns from the alloy (a) after pre-aging, (b) peak aged condition of the pre-aged alloy, (c) peak condition without a pre-aging treatment [7].

Lee *et al.* [9] examined the effect of various pre-aging treatments on the paint bake hardening response of an AA7075 alloy. Based on the hardness values measured after the paint bake process, the suitable pre-aging condition was determined to be 120℃/30min. As the pre-aging duration was increased from 30min to 240min, although it exhibited higher strength after the paint bake cycle, the pre-aged sample showed a lower elongation during the tensile test before the paint bake treatment, which resulted in poor formability. Based on their TEM observations (Figure 2.12), GP zones are the main precipitates after the pre-aging process which grow in size and density by increasing the pre-aging time from 30 to 240min (Figure 2.12 (a) and (b)). After the final artificial aging step, η' particles are the dominant precipitates in the matrix (Figure 2.12 (c) and (d)) which appear relatively finer and more closely-spaced in the sample with the pre-aging step (Figure 2.12 (d)). Similar results were also observed by Werenskiold *et al.* [3] in that a multi-step aging resulted in a smaller precipitate size compared to a single-aging process.

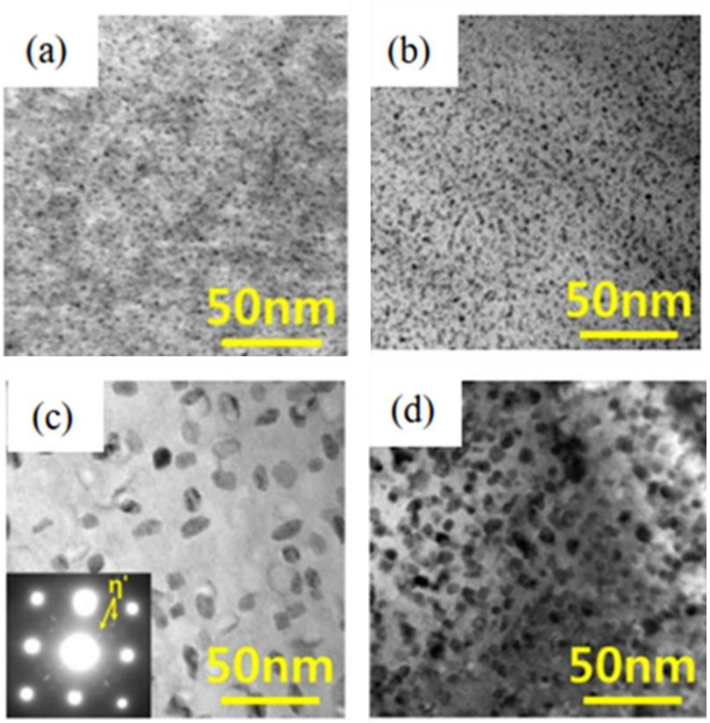

Figure 2.12. TEM micrographs after the pre-aging process (a)120C/30min, (b) 120C/240min, (c) artificial aging without pre-aging, d) artificial aging with pre-aging process [25].

To summarise, the pre-aging treatment is considered an effective method for the formation of fine, closely spaced and stabilized GP zones as the precursors to the strengthening η′ phase. Such treatment improves the bake-hardening responses of 7000-series aluminum alloys during subsequent artificial aging processes.

2.3.3. Effect of deformation on precipitation hardening

A considerable number of studies have focused on the effect of deformation on the precipitation hardening response of 7000-series aluminum alloys [5], [13], [15], [16], [51]. Those studies have examined the change in alloy properties through thermomechanical treatment consisting of plastic deformation after quenching at room temperature or forming the material at artificial aging temperatures (*i.e.* warm-forming processes). The deformation step introduces a large density of dislocations within the material that can alter the precipitation behaviour in various ways [15], [16], [52]. The primary effect of dislocations is to reduce the energy barrier of nucleation [53]. Indeed, dislocations are favorable heterogeneous nucleation sites leading to a faster precipitation kinetics [16]. Also, it is observed that dislocations are fast diffusion paths resulting in an accelerated growth and coarsening of precipitates through pipe diffusion [11], [15], [53]. The interaction between solute and dislocations leads to a solute flux toward the dislocations [16], [24] resulting in a lower solute fraction available for homogeneous precipitation [16]. Dislocations are also vacancy sinks. Annihilation of vacancies through their interactions with dislocations has an adverse effect on the precipitation process [16]. Therefore, in the cases where the formation of small-size homogeneous precipitates is easily possible, the presence of dislocations can deteriorate the mechanical properties [16]. It is reported that the kinetics of precipitation during natural aging is slowed down by the presence of dislocations that act to progressively annihilate vacancies which normally assist in the formation of GP zones during natural aging [16], [54]. On the other hand, in alloys in which the homogenous formation of hardening precipitates (such as η') is difficult, prior plastic deformation can greatly enhance the hardening response [15].

Deschamps *et al.* [16] investigated the artificial aging behaviour of a 7000-series aluminum alloy that was subjected to sequential natural-aging, pre-straining and artificial aging at 160℃. Their TEM analysis showed that, in contrast to the non-deformed material which had a homogenous distribution of fine precipitates (Figure 2.13 (a)), there was a spatial gradient in the precipitate size and distribution in the deformed material after 1 hour of artificial aging (Figure 2.13 (b)). Precipitates formed on dislocations were coarse while far from dislocations, finer precipitates were homogeneously distributed. In fact, due to the progressive annihilation of vacancies through dislocations, GP zone structures in the vicinity of dislocations were poorly developed.

Thus, nucleation of η' precipitates was difficult and resulted in larger precipitate size (see Figure 2.13 (a-b)). They also observed large precipitate-free zones (PFZ) around dislocations during the later stages of aging which was related to the solute flux to the dislocations resulting in a rapid growth and coarsening of precipitates during over-aging (compare Figure 2.13 (c) and (d)).

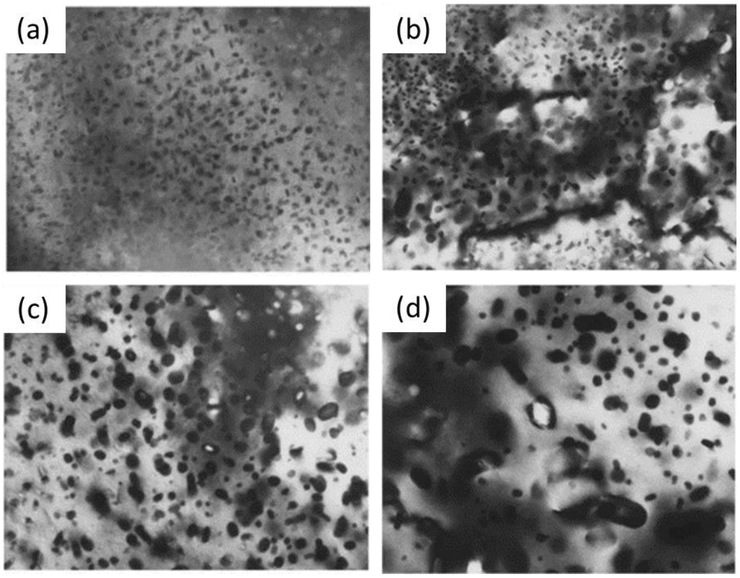

Figure 2.13. TEM images of the 7000-series aluminum alloy aged for 1 hour at 160℃ (a) no pre-deformation, (b) 10% pre-deformation, and aged for 50h at 160℃ (c) no pre-deformation (d) 10% pre-deformation [16].

Deschamps *et al.* [16] have also examined the effect of deformation on the precipitation kinetics of naturally-aged 7000-series aluminum alloy using differential scanning calorimetry (DSC) tests. The DSC results along with the TEM observations suggested that an increased amount of deformation promotes the formation of $\boldsymbol{\eta}$ phase on the dislocations. Reportedly, the pre-deformation decreased the peak-strength value (*i.e.* loss of ~ 60 MPa) after natural aging. They concluded that deforming a naturally-aged material, significantly alters the precipitates' microstructure and decreases the peak strength of the alloy upon the subsequent artificial aging.

Poole *et al.* [51] reported a reduction in hardening kinetics upon natural aging of AA7030/AA7108 alloys for cases with high levels of pre-deformation. They attributed this effect to the progressive annihilation of vacancies through dislocations which inhibit GP zones formation. An accelerated coarsening of precipitates during over-aging was also observed for higher levels of pre-deformation which was related to the short-circuit diffusion along dislocations.

The progressive growth and coarsening of precipitates induced by solute diffusion along dislocations was also reported by Deschamps *et al.* [15]. They applied a warm-forming cycle through a multi-step aging process of an AA7449 alloy. As illustrated in Figure 2.14, precipitates are larger in the deformed materials compared to those in the un-deformed ones in under-aged (Figure 2.14 (a-b)) or over-aged conditions (Figure 2.14 (c-d)).

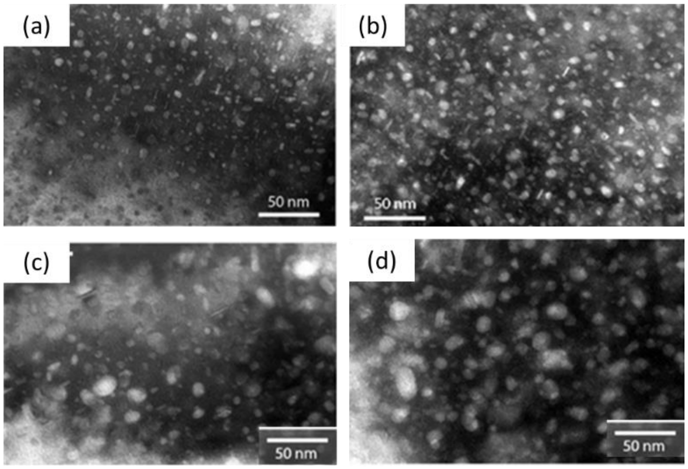

Figure 2.14. TEM micrographs of AA7449 material before and after straining (a) Under-aged/undeformed, (b) under-aged 6% deformation, (c) over-aged/undeformed, (d) over-aged 6% deformation [15].

In contrast to the results of Deschamps *et al.* [16] and Poole *et al.* [51], an experiment performed by Emani *et al.* [50] on AA7075 showed that deforming a pre-aged material improves its strength during the final aging step (@177℃). This result was related to the combined effects of strain hardening and the heterogeneous nucleation of fine η' precipitates on the dislocations. It was observed that the material's hardness increased with a delay (~20 min) during the final aging step due to the competition between the dislocation recovery and the precipitation process.

A similar result was reported by Wang and Ma [55] who found that 5 % pre-straining of an as-quenched AA7050 alloy improves the material strength after the subsequent artificial aging process (*i.e.* solution heat treatment + water quench + 5% pre-strain + aging at 120℃ for 24 hours). It is evident in their reported TEM images that the matrix of the T6 samples (*i.e.* aged at

120°C for 24 hours after quenching) shows a homogenous distribution of precipitates in the un-deformed sample, which is not the case in the pre-deformed case (Figure 2.15 (a-b)). It is observed in Figure 2.15 (b) that many dislocations had remained in the matrix of the pre-deformed sample after the aging process which reportedly had contributed to the improved strength of the material. Their DSC analysis of the as-quenched material (Figure 2.15 (c)) revealed that the exothermic peaks II and III have moved to the lower temperatures for the pre-deformed sample. This effect was attributed to the presence of dislocations that act as effective nucleation sites leading to the formation of η' and η at lower temperatures. Accelerated formation of the hardening precipitates η' was believed to be one of the reasons for the increase in the peak-strength. It is worth noting that the larger area associated with the endothermic event I (the dissolution peak) and its shift to a lower temperature in the pre-deformed sample were related to the accelerated dissolution of GP II zones (as vacancy-rich clusters) in the presence of dislocations. This phenomenon was reported to be due to the annihilation of vacancies on the dislocations[55].

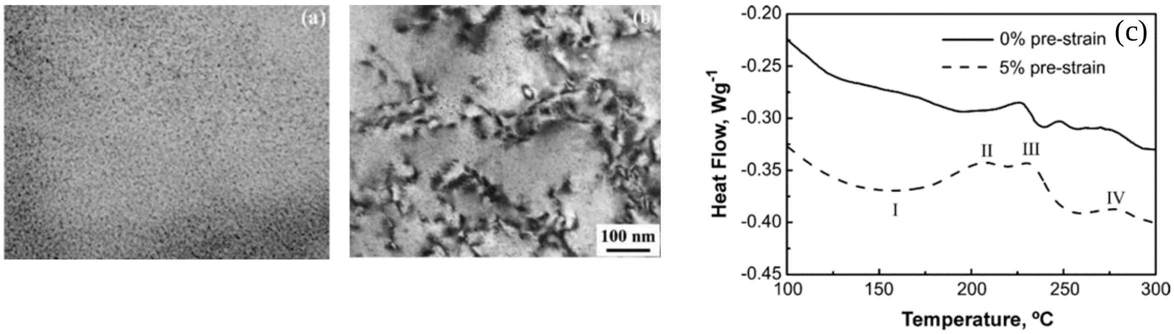

Figure 2.15. TEM images of the AA7050 samples in the T6 condition with (a) 0% pre-straining (b) 5% pre-straining after quenching and (c) DSC results of the as-quenched samples with and with out the pre-straining effect [55].

Considering the above-mentioned experiments, due to the variety of possible interactions, the effect of dislocations on precipitation and mechanical properties strongly depends on the alloy type and ageing sequence. A complete understanding of the effect of deformation on the material properties can be achieved through considering the detailed relationships between the microstructure and the mechanical properties all along the ageing treatment.

2.4. Process modeling

Modeling of precipitation kinetics and mechanical properties of aluminum alloys has always been an area of great interest in physical metallurgy [1]–[3], [26], [48], [51], [56], [57]. The main purposes of the modeling approaches are to (a) predict the strengthening behaviour, (b) optimise the heat-treatment procedures and (c) obtain a better understanding of the process-structure-property relationships. To achieve the intended goals, process models have been developed to capture the major effects of various processing parameters on the precipitation hardening behaviour of these alloys. A concise review of the basic modeling approaches that will be pursued in this thesis is provided in the following.

2.4.1. Precipitation kinetics

Precipitation kinetics have been previously evaluated using various approaches [1], [2], [56]. This work is concentrated on the methodologies developed by Esmaeili *et al.* [1], [2] to predict the precipitation kinetics during single and multi-step aging processes. Although the kinetic models were originally developed for 6xxx-series aluminum alloys, the underlying theory of precipitation kinetics can be applied to 7xxx-series alloys as well [58].

2.4.1.1. Modeling of precipitation kinetics

Esmaeili and Lloyd [2] have developed a general model to describe the precipitation kinetics upon multi-step and non-isothermal aging processes:

$$f_r = 1 - (1 - f_r^0)\, exp[-\textstyle\sum_i k_{iv}^n (t_i^n - t_{i-1}^n)] \qquad (2.5)$$

in which, $f_r = \frac{f}{f_{peak}}$ is the fraction of precipitation reactions completed, *i.e.* the relative volume fraction of precipitates, at time t_i, f_r^0 is the relative volume fraction of precipitates at the start of final artificial aging step, k_{iv} is the temperature dependent constant value describing the reaction rate within the bulk (volume) and *n* is a numerical time exponent and is mostly defined as a shape factor. Bratland *et al.* [59] have reported that for a diffusion-controlled growth the *n* value attains a value between 0.5 and 2.5 depending on the assumptions of the model. however, the *n* value is related to the particular nucleation and growth conditions which have been discussed in detail by Christian [60].

It is reported that the rate constant k_v has an Arrhenius relationship with temperature [1]:

$$k_{iv} = k_{0v} exp\ (\frac{-Q_v}{RT_i}) \qquad (2.6)$$

in which k_{0v}, Q_v and R are the frequency factor, apparent activation energy and the universal gas constant (8.314 $\frac{kJ}{mol.K}$), respectively.

To describe the precipitation kinetics upon (a) multi-step aging in isothermal conditions, and (b) direct-aging processes, the general model, *i.e.* Eq. (2.5), can be simplified into the following forms:

(a) Multi-step aging under isothermal conditions

$$f_r = 1 - (1 - f_r^0)\ exp(-k_v t)^n \qquad (2.7)$$

(b) Direct-aging

In a direct aging process, f_r^0 equals to zero. So, Eq. (2.5) can be expressed as:

$$f_r = 1 - exp\ (-k_v t)^n \qquad (2.8)$$

It is worth mentioning that Eq. (2.8) is a generalized form of the well-known "Johnson-Mehl, Avrami, Kolmogorov (JMAK)" model [61]–[63] and has been commonly used in kinetic-related studies (direct aging in particular) [64]–[70].

The kinetic parameters n and k_v should be obtained pursuing the approach of Esmaeili *et al.* [1], by utilizing isothermal calorimetry (IC) test results. To implement the non-isothermal kinetic model (Eq. (2.5)), the kinetic parameters obtained from the isothermal calorimetry tests on any pre-aged condition, as well as the as-quenched condition, of the material in the isokinetic temperature range of interest are required [2].

2.4.1.2. Isothermal calorimetry data analysis for modeling

It has been well-stablished that the precipitation kinetics of aluminum alloys during direct or multi-step aging processes can be analysed through the isothermal calorimetry (IC) technique [2], [58], [71].

According to Esmaeili and Lloyd's approach [2], the relative volume fraction of precipitates f_r during the multi-step aging process is estimated as:

$$f_r = f_r^0 + \frac{f_{V|AA}}{f_{V|peak}} \qquad (2.9)$$

in which, $f_r = \frac{f_V}{f_{V|peak}}$ and $f_r^0 = \frac{f_{V|PA}}{f_{V|peak}}$ is the relative volume fraction of precipitates at the start of final artificial aging (AA) step or at the end of the pre-aging (PA) step. The second term on the right hand side of Eq. (2.9) is determined as [2]:

$$\frac{f_{v|AA}}{f_{V|peak}} = \frac{\int_0^t \frac{dQ}{dt} dt|_{PA+AA}}{\int_0^{t_f} \frac{dQ}{dt} dt|_{AQ+AA}} \qquad (2.10)$$

in which Q is the heat flow that is recorded versus time t during the IC test, $\int_0^t \frac{dQ}{dt}\ dt|_{PA+AA}$ is the area under the IC trace up to time t for the pre-aged material and $\int_0^{t_f} \frac{dQ}{dt}\ dt|_{AQ+AA}$ is the area under the IC trace up to the peak aged condition (up to time t_f) for the as-quenched material, when the heat flow becomes too small and close to zero. The f_r^0 value can be determined from the two equations of (2.9) and (2.10) for $t = t_f$ and $f_r = 1$ [2]:

$$f_r^0 = \frac{\int_0^{t_f} \frac{dQ}{dt} dt|_{AQ+AA} - \int_0^{t_f} \frac{dQ}{dt} dt|_{PA+AA}}{\int_0^{t_f} \frac{dQ}{dt} dt|_{AQ+AA}} \qquad (2.11)$$

To find the kinetic parameters *n* and k_v during multi-step and isothermal aging process, Eq. (2.7) is expressed in the following form [2]:

$$ln ln \frac{(1-f_r^0)}{1-f_r} = n ln t + n ln k_v \qquad (2.12)$$

By plotting $ln ln \frac{(1-f_r^0)}{1-f_r}\ vs\ n ln t$ and substituting the experimental values of f_r^0 and f_r obtained from the IC tests (Eqs. (2.9) - (2.11))), the kinetic parameters can be determined.

Furthermore, based on Esmaeili *et al.*'s [1], [32] methodology, the relative volume fraction of precipitates f_r after time *t* during the direct aging process is calculated as:

$$f_r = \frac{\int_0^t \frac{dQ}{dt} dt}{\int_0^{t_f} \frac{dQ}{dt} dt} \qquad (2.13)$$

in which, $\int_0^t \frac{dQ}{dt}dt$ is the area under the IC trace of the as-quenched material up to time t and $\int_0^{t_f} \frac{dQ}{dt}dt$ is the total amount of heat evolved during the whole aging period up to time t_f, when the heat flow becomes too small and close to zero.

Similar to the case of multi-step aging, to find the kinetic parameters n and k_v during the direct aging process, Eq. (2.8) is expressed in the following form [1]:

$$lnln\left(\frac{1}{1-fr}\right) = nlnt + nlnk_v \qquad (2.14)$$

By substituting the experimental values of f_r from Eq. (2.13) in Eq. (2.14) and plotting $lnln\left(\frac{1}{1-fr}\right)\ vs\ lnt$, the constant parameters n and k_v are determined.

Finally, having obtained the values of k_v for various aging temperatures, the constant parameters of k_{0v}, Q_v can be calculated through the Arrhenius relationship, Eq. (2.6) [1], [2].

2.4.2. Yield strength model

Esmaeili and coworkers [1] have used a linear addition law to account for the contributions from precipitation hardening (σ_{ppt}), solid solution strengthening (σ_{ss}), and the intrinsic strength of aluminum matrix (σ_i) to the overall yield strength in the absence of deformation:

$$\sigma_y = \sigma_i + \sigma_{ss} + \sigma_{ppt} \qquad (2.15)$$

It is worth noting that the grain size effect is considered as part of the intrinsic strength of aluminum [32]. Moreover, considering the concepts of weak and strong obstacles (as were explained in section 2.2), the individual contributions of σ_{ss}, $\sigma_{\mathrm{ppt|Strong}}$, and $\sigma_{\mathrm{ppt|Weak}}$ to the yield strength were defined as [1], [2]:

$$\sigma_{ss} = \sigma_{0ss}(1 - \alpha f_r)^{2/3} \qquad (2.16)$$

$$\sigma_{ppt|Strong} = C_1(f_r)^{1/2} \qquad (2.17)$$

$$\sigma_{ppt|Weak} = C_2(rf_r)^{1/2} \qquad (2.18)$$

in which, α is the fraction of initial solute concentration depleted from the matrix when f_r approaches unity (i.e. at the peak-aged condition), σ_{0ss} is the contribution from solid solution to the yield strength when the material is in the as-quenched state ($f_r = 0$), C_1 and C_2 are constant parameters which can be determined using the experimental values of yield strength and precipitate radius (r) at the peak aged condition: $\mathrm{C}_1 = \sigma_{\mathrm{ppt|Strong}}$ & $\mathrm{C}_2 = \frac{\sigma_{\mathrm{ppt|Weak}}}{(r)^{1/2}}$.

The weak obstacle model, Eq. (2.18), was further modified by Sepehrband and Esmaeili [58] for the multi-step aging process assuming that pure growth of precipitates (and not nucleation of new nuclei) is the dominant controlling mechanism in the presence of pre-existing precipitates:

For pure growth [58]: $$\sigma_{ppt|Weak} = C_1(f_r)^{2/3} \qquad (2.19)$$

Cheng *et al.* [5] considered the effect of deformation on the yield strength of AA6111 and AA7030 alloys and proposed the following superposition law to account for the dislocation hardening contribution under varied conditions:

$$\sigma_y = \sigma_i + \sigma_{ss} + \left(\sigma_{ppt}^m + \sigma_d^m\right)^{1/m} \qquad (2.20)$$

in which the term σ_d denotes the extra strengthening due to the increase of the dislocation density. Also, the exponent m describes the interaction between σ_{ppt} and σ_d. Some authors have considered $m = 2$ in Eq. (2.20) [56], [72]. However, it is reported that the m value can vary between 1 and 2, i.e. being 1 for shearable precipitates and increasing to 2 for non-shearable precipitates [5], [73], [74]. Accordingly, Cheng *et al.* [5] have used $m = 1.5$ in their calculations, which was due to the presence of a combination of shearable and non-shearable precipitates at the peak-aged condition.

Moreover, the contribution of dislocation hardening, σ_d, to the yield strength was defined as [5], [15], [44], [75], [76]:

$$\sigma_d = \alpha_d M \mu b \rho^{1/2} \qquad (2.21)$$

Where, α_d is a constant of order 0.3, M is the Taylor factor (equal to 3.06 for the fcc metals), μ is the shear modulus (25.4 GPa), b is the magnitude of the Burgers vector (0.286 nm for Al) and ρ is the dislocation density [5].

2.5. Summary and objectives

Considerable research has been conducted on the precipitation hardening behavior of 7000-series aluminum alloys. Most prior studies have focused on the effect of various aging practices, *e.g.* natural aging, direct aging and multi-step aging, on the precipitation hardening behaviour and microstructural evolution of these alloys. It has been reported that multi-step heat treatments are used to broaden the commercial application of 7000-series aluminum alloys by improving the kinetics of precipitation and the hardening potential of these alloys. The influence of dislocations induced by plastic deformation on the precipitation hardening response of 7000-series aluminum alloys has also been analysed by many authors. It is evident that dislocations act as favorable heterogenous nucleation sites and can greatly enhance the hardening response of the material, acting in combination with conventional dislocation hardening. However, in some cases in which homogenous precipitation is easily activated (*e.g.* during natural aging), the presence of dislocations can degrade the resulting mechanical properties. Accelerated growth and coarsening of precipitates due to solute transport towards dislocations and pipe diffusion has also been reported for 7000-series aluminum alloys.

Over the past years, physically-based models have been developed to predict the precipitation kinetics and resulting mechanical properties of 6000/7000-series aluminum alloys for various aging treatments. A general model has been developed by Esmaeili and Lloyd [2] to predict the relative volume fraction of precipitates (which is a representation of the precipitation kinetics) upon multi-step and non-isothermal aging processes of 6000-series aluminum alloys. Esmaeili and Lloyd's model [2] drastically reduced the number of input parameters that are usually needed for modelling of precipitation hardening in 6000-series aluminum alloys. Although the model was later implemented on a 7000-series aluminum alloy, *e.g.* AA7030 [58], further evaluation of the model's applicability to other 7000-series aluminum alloys is needed to confirm the usefulness of the model to predict precipitation hardening behaviour of 7000-series alloys in general. The yield strength of variably aged aluminum alloys has also been modeled by considering the concepts of weak and strong obstacles [2], [48]. However, the original models developed by Esmaeili *et al.* [48] and Esmaeili and Lloyd [5] do not include (a) the modelling of precipitate size when nucleation is as important as growth and its influence in reducing the number of parameters needed for a weak obstacle formulation, and (b) the effect of strain hardening on precipitation kinetics and yield strength.

To understand and model aging behaviour in variably heat-treated aluminum alloys (with or without deformation), there first exists a need to qualitatively analyze precipitation evolution and resulting mechanical properties, which strongly depend on the alloy type and heat treatment condition. Such knowledge can be used as reliable basis for formulations describing the evolution of precipitation kinetics and yield strength during various heat treatments. To this end, and considering the previously-mentioned gaps within the current literature, the objectives of this thesis are to: (i) qualitatively investigate the effects of (a) various aging practices, and (b) deformation during a warm-forming cycle, on the precipitation hardening response and aging kinetics of AA7050 and AA7075, respectively; (ii) use the simplified versions of the kinetic model developed by Esmaeili and Lloyd [5] to predict the precipitation kinetics of AA7050 upon multi-step aging under isothermal conditions as well as direct aging processes; (iii) expand the viability of the weak obstacle formulation by developing a new model that predicts the evolution of precipitate radius as a function of the relative volume fraction of precipitates; and, (iv) expand Esmaeili and Lloyd's model [5] to include the effect of dislocations (deformation) on the precipitation kinetics, particularly in the context of warm forming and thus, model the yield strength evolution during the multi-step aging process coupled with a warm-forming stage.

The balance of this thesis is organized as follows: Chapter 3 provides information about the material, the heat treatment procedure, and the characterization experiments. The experimental results and discussion associated with various heat treatment and processing conditions of the alloys are presented in Chapter 4. In Chapter 5, the results of the precipitation kinetic analysis and the yield strength modeling for each heat treatment procedure are presented. Finally, the conclusions stemming from this research and recommendations for future work are in Chapter 6.

3. Experimental methodology

This chapter includes information on the materials under the investigation, the heat treatment procedures, and the experimental techniques which have been used in this study.

3.1. Material

Two common Cu-containing 7000-series aluminum alloys, AA7050 and AA7075, with different ratios of Cr/Zr (*i.e.* varied quench sensitivities) and precipitate forming solute contents (*i.e.*, Zn, Mg and Cu), were provided by Arconic in T6 condition and in the form of 2.0 mm thick sheet. The chemical compositions of the alloys were analyzed by inductively-coupled plasma atomic emission spectrometry, according to ASTM E1097-12 [77]. The analysis results are reported in Table 3.1.

Table 3.1. The chemical compositions of AA7075 and AA7050 (wt%).

	Mn	Si	Cr	Mg	Ti	Cu	Zn	Fe	Zr
AA7050	0.01	0.03	0.01	2.04	0.02	2.15	6.44	0.04	0.11
AA7075	0.04	0.08	0.19	2.27	0.03	1.38	5.63	0.15	0.01

The initial focus of this research was on AA7050, which was utilized in evaluating the effects of various heat treatments (*i.e.* natural aging, direct aging and multi-step aging) on age hardening response through experimental and modeling methods. This alloy was of initial interest due to its lower Cr content (compared to AA7075). It was determined in related studies by Pishyar *et al.* [78] that the formability of AA7050 was inferior to that of the current AA7075. As a result, the experiments and the modeling analysis considering the effect of a warm forming thermal cycle followed by an artificial aging process on final properties were limited to AA7075.

3.2. Processing

3.2.1. Heat treatments - AA7050

Square-shaped AA7050 samples (of size 7 mm x 7 mm x 2 mm) were cut from the as-received sheet for heat treatment, hardness measurement and calorimetry tests. The optimum solutionizing time and temperature were confirmed to be 10 minutes at 470°C by performing a set of comparative DSC tests on the water-quenched samples with various solution heat treatment histories. The solution heat treatment, which was followed by water quenching to room temperature, and the aging processes were carried out in a Techne FB-08C fluidized sand bath furnace. The heat treatment paths of the directly aged or multi-step aged alloys are outlined in Table 3.2.

Table 3.2. Various aging routes considered for the AA7050 alloy.

Natural aging	Solution heat treatment (SHT)+ Water quench + Natural aging up to one year (NA)
Artificial aging	Direct aging: SHT + Water quench + aging @ 150 and 177℃
	Multi step aging: SHT + Water quench + 2 days natural aging + 4h @ 100℃ + aging @ 150 and 177℃

3.2.2. Thermo-mechanical processing - AA7075

Experiments were also performed on the AA7075 sheet. The samples were cut from the as-received sheets in accordance with a modified version of the mini JIS [79] (MJIS) tensile specimen designed by Pishyar [80]. The dimensions of this geometry are shown in Figure 3.1. The samples for warm-forming were heat treated according to the time-temperature profile that is shown in Figure 3.2. The warm-forming process was accomplished using a thermomechanical simulator (Gleeble-3500, Dynamic Systems Incorporated). Certain modifications were made to the Gleeble grippers to accommodate these specimens, as described by Pishyar [80].

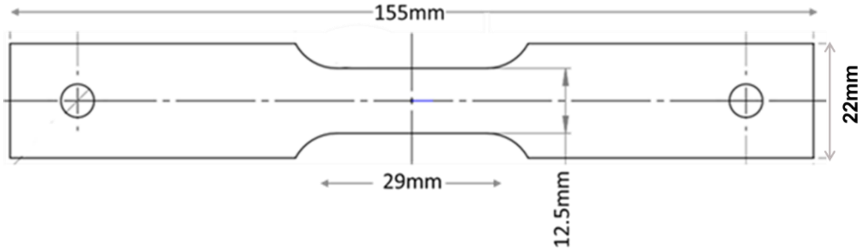

Figure 3.1. Modified Gleeble sample geometry [80].

The process was started with solution treatment (470℃ for 20 min) followed by immediate water quenching and room temperature storage (*i.e.* natural aging) for two days. The naturally-aged samples were then aged for 4 hours at 100℃ to achieve the pre-aged sample condition. The pre-aged samples were subjected to warm deformation by heating to 150℃ in 10 s followed by tensile deformation at this temperature to reach a total uniaxial strain of approximately 10% in the central region of the samples. A strain rate of 0.01 (s^{-1}) was used during the tensile deformation. The sample temperature during deformation was 150℃. The sample was held at temperature 50 s and then pulled for 10 s, such that the total time at 150℃ was approximately 60 s. Digital image correlation (DIC) techniques were used to analyse the Gleeble test results to confirm that the level of strain in the central region within the gauge area reached 10%. The DIC analysis was performed by Pishyar [80] and the details of the DIC methodology can be found in reference [80]. A schematic presentation of the warm-forming procedure and a plot of the major true strain contours from one of the tested samples is shown in Figure 3.2. After warm-forming, the samples were artificially aged in the sand-bath furnace at 177℃ for various times up to 90 minutes. This final aging temperature was chosen for its relevance to automotive paint-bake cycling (PBC) process, which is usually simulated in the laboratory as 30-60 minutes of aging at ~177℃ [9], [71], [81]. Samples were stored in dry ice (-78.5 °C) between the pre-aging and warm forming stage, and prior to the final artificial aging process. The maximum period of time that samples were stored in the dry ice before testing was two weeks. It should be noted that all the samples for the subsequent aging and experimental tests were extracted from the uniform region in the gauge area of the warm-formed specimens (the purple area in Figure 3.2).

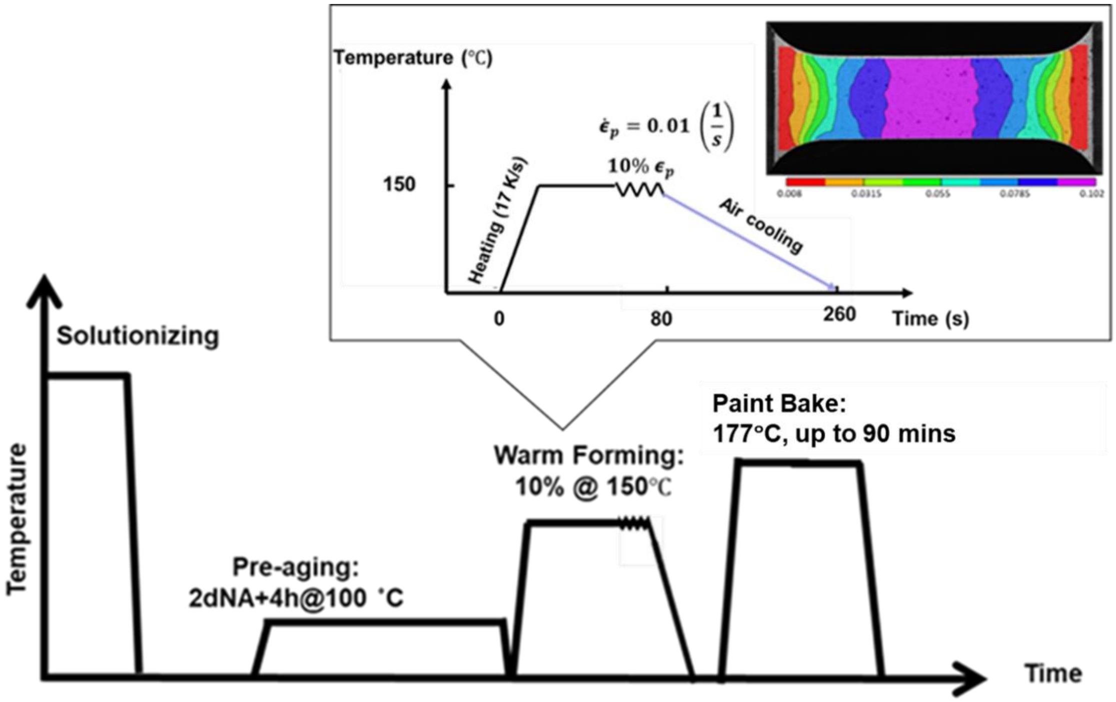

Figure 3.2. Time-temperature history for the experimental procedure performed on AA7075.

It is important to note that in this work, the pre-aged material (that is subjected to “2 days natural aging + 4h @ 100°C") is designated as “PA”, and the pre-aged material that is subjected to the warm-forming process, is designated as “PA+WF”.

3.3. Characterization

3.3.1. Hardness measurements

To assess the effect of various aging treatments on the precipitation hardening response of the alloys, Vickers micro-hardness tests were conducted on 7 mm x 7 mm x 2 mm samples using a Leco micro-hardness tester with a 300 g load. To avoid further aging (due to high temperatures of hot-mounting or a 1-day duration of cold-mounting), the heat-treated samples were glued directly to a mount block before grinding and polishing. Five measurements were made on each sample and the average values were reported. It is worth mentioning that in this study, the measured Vickers micro hardness values are multiplied by 3 to acquire a rough estimation of the yield strength.

3.3.2. Differential scanning calorimetry (DSC)

To characterize the effect of various aging practices on the precipitate development, differential scanning calorimetry (DSC) experiments were carried out on the AA7050 and AA7075 samples using a heating rate of 1℃/min within the range of 30-300 ℃. The DSC tests were performed with a SETARAM C80 calorimeter in an air atmosphere. For each test, multiple 7 mm x 7 mm x 2 mm samples with a total mass of 900-950 mg were placed in the test vessel. A second DSC test was run on pure aluminum samples with identical mass to obtain a baseline trace. The heat released or absorbed was recorded as a function of temperature corresponding to a precipitation or dissolution reaction, respectively. The final DSC trace (the net trace) was obtained by subtracting the trace of the pure aluminum (*i.e.* the baseline trace) from the trace acquired for the alloy sample. It is worth mentioning that in this study, the exothermic reactions are plotted upwards and the endothermic reactions downwards on the DSC thermographs. The test repeatability was checked by conducting at least two repeats for each testing condition.

3.3.3. Isothermal calorimetry (IC)

To analyze the precipitation kinetics during the artificial aging process, isothermal calorimetry (IC) tests were conducted on AA7050 and AA7075 samples. The IC tests were done in a SETARAM C80 calorimeter in an air atmosphere. The test procedure followed the methodology published by Esmaeili and Lloyd [2] and Esmaeili *et al.* [1], and consisted of tests on the alloy and pure Al samples of identical mass (total mass ~ 900-950 mg). The heat flow versus time data obtained from the tests on pure Al samples at each artificial aging temperature was subtracted from the corresponding alloy sample data. The repeatability of the IC test results was confirmed by running multiple tests on each alloy condition. The heat treatment histories of the samples, as well as the IC test temperatures, are outlined in Table 3.3.

Table 3.3. Isothermal calorimetry testing conditions of AA7050 and AA7075 alloys.

Alloy	**Sample heat treatment history**	**IC Test temperature**
AA7050	As quenched: SHT + Water quench	135, 150, 165, 177, 190℃
	Pre-aged: SHT+ Water quench + 2days NA+4h@100℃	135, 150, 165, 177 ℃
AA7075	As quenched: SHT + Water quench	150, 165,177 ℃
	Pre-aged: SHT + Water quench + 2days NA + 4h@100℃	150, 165,177 ℃
	Pre-aged + Warm deformed: SHT + Water quench + 2days NA + 4h@100℃ + WF @ 150°C	150, 165,177 ℃

4. Experimental results and discussion

This chapter presents the experimental results and discussion associated with the heat treatment and processing described in Chapter 3, by means of two main categories: the effects of (a) various aging practices, and (b) deformation during a warm-forming cycle, on the precipitation hardening response and aging kinetics of AA7050 and AA7075, respectively.

4.1. Effect of varied aging treatments on age hardening - AA7050

In this section, the effect of various aging treatments on the age hardening behavior of AA7050 is investigated through hardness measurements and calorimetry analysis. As was described in Section 3.2.1, the studied heat treatment routes are natural aging, direct aging, and multi-step aging. The results and discussion associated with each heat treatment are separately presented in the following sections.

4.1.1. Natural aging

4.1.1.1. Hardness test results

The hardness evolution of AA7050 over a period of up to one-year of natural aging is presented in Figure 4.1. The hardness increase is attributed to the formation of GP zones within the matrix during the natural aging process. It can be observed from the figure that the hardness of the material tends to reach a plateau after certain natural aging times, which can be due to a reduction in the supersaturation of the matrix and associated lower driving force for precipitation of GP zones in the matrix. The increase in hardness due to natural aging in AA7050 and AA7075 was well-documented by Staley [47]. According to his electrical resistivity measurements, the hardness increment was attributed to the formation of GP zones during natural aging. Additionally, Staley showed that the hardness of the material does not change significantly upon longer natural aging times (more than 1 year).

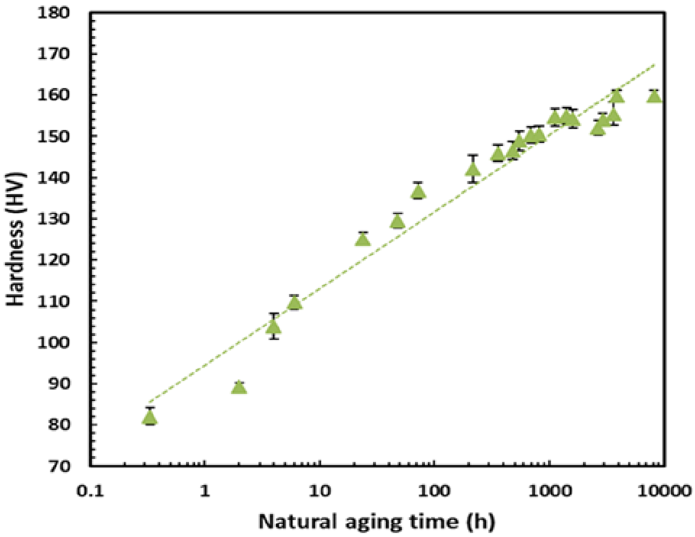

Figure 4.1. Hardness evolution of AA7050 up to 1-year natural aging.

4.1.1.2. DSC results

To investigate the changes in the precipitation state during natural aging, DSC tests were conducted on the as quenched and naturally aged AA7050 samples. The results are presented in Figure 4.2.

The first three exothermic peaks on the DSC trace of the as-quenched material (the blue trace), presented as peaks A, B and C, are most likely related to the formation of GP zones, η' and η precipitates, respectively, during the DSC run [35], [82]. Comparison of the DSC traces of the naturally aged and as-quenched samples clearly shows the absence of the GP zone formation peak (*i.e.* peak A) on the DSC traces of the naturally aged materials. This result suggests that substantial level of GP zones are formed even during one day of natural aging prior to the DSC run. The initial endothermic troughs on the DSC traces of the naturally aged materials, designated as D, are associated with the dissolution of GP zones formed by natural aging during the DSC run [83]. It is observed in the figure that this endothermic trough shifts to higher temperatures and the associated area becomes larger for longer natural aging times. Such behavior has also been observed by Abolhasani [84], examining natural aging in AA7075. The observed shift in the endothermic trough can be due to the extensive formation of GP zones with larger sizes and/or more stable structures during longer natural aging times. The other noticeable difference in the DSC traces of the naturally aged materials is the presence of a small exothermic peak around 80℃ on the DSC traces of the 1 and 2 day naturally aged samples (indicated by an arrow in Figure 4.2). This peak can be associated with the formation of GP II zones which are reported to nucleate at temperatures above 70℃ [41]. This small exothermic peak appears to decrease in magnitude with increasing natural aging time until it is barely visible in the trace of the 4-day naturally aged sample and then not visible anymore. This observation can be due to the higher amount of solute remaining in the matrix after shorter natural aging times which can give rise to the small exothermic peak during the DSC run.

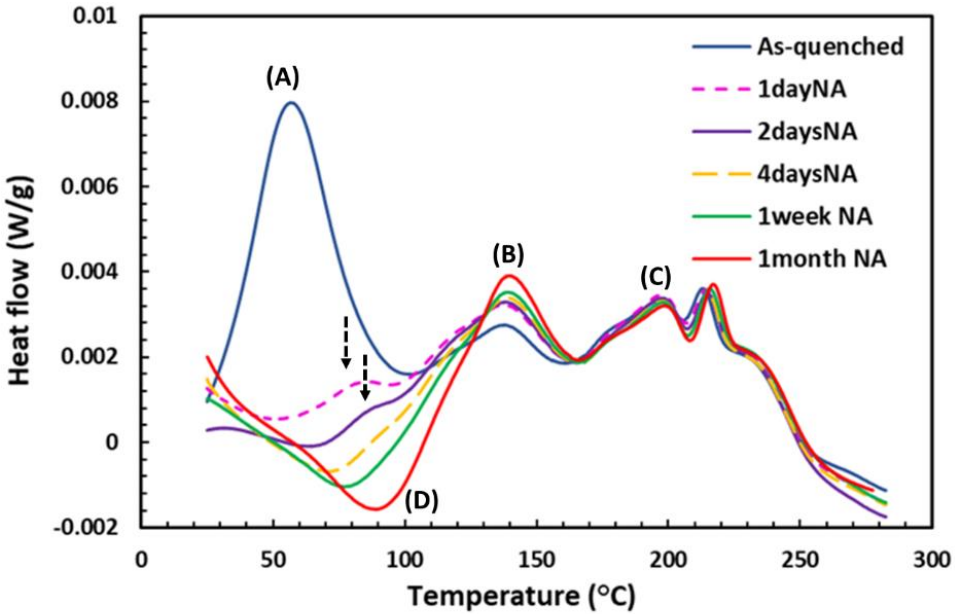

Figure 4.2. Comparison of the DSC traces of the as-quenched and naturally aged AA7050 material (up to 1-month natural aging).

4.1.2. Artificial aging

4.1.2.1. Hardness test results

The age hardening responses of the directly-aged and multi-step aged AA7050 were examined for the aging temperatures of 150 and 177℃. The results are presented in Figure 4.3.

Direct aging

The results of the hardness experiments on the directly aged samples (AQ+AA@150/177℃) show that the hardness increases with aging time until the peak hardness is achieved after 4 hours (a broad peak starting from 4 h) at 150 ℃ and 1 hour of aging at 177℃.

As expected, during aging at higher temperature of 177°C, the peak hardness is achieved earlier which is due to the faster rate of precipitation at the higher temperature.

Also, direct aging at 177℃ leads to a reduced peak hardness value compared to 150℃. The increased precipitate spacing due to the lower driving force for nucleation during aging at the higher temperature [53], likely resulted in the reduced peak hardness value compared to the lower aging temperature. A similar result was observed by Fan [85] in that the direct aging of an AA7150 alloy at a higher aging temperature led to a reduced peak hardness value compared to the lower aging temperature.

Multi-step aging

Figure 4.3 shows hardness versus secondary aging time for pre-aged AA7050 (PA+AA@150/177℃). Here, the pre-aging step comprised two days of natural aging, followed by 4 hours of aging at 100°C. It is observed from the multi-step aged sample's hardness curves (Figure 4.3) that the peak hardness during the final step of aging at 150 and 177°C is achieved after about 6 hours and 1 hour, respectively.

It is also observed that the multi-step aging at both temperatures results in hardness values comparable to the T6 hardness value of the current AA7050 alloy (~186HV). Likewise, Emani *et al.* [50] reported similar peak hardness values after multi-step (1h at 120℃ + 1h at 177℃) and single-step (T6) heat treatments of AA7075 alloy.

It is shown in Figure 4.3 that for both aging temperatures, the hardness of the material after multi-step aging is higher in every stage in comparison with the direct aging. However, this effect is much more significant for the case of 177℃ than 150℃, since the difference in the peak hardness value after multi-step aging and direct-aging at 177℃ is relatively large. These results can be explained based on the precipitation process during such a multi-step heat treatment. It is reported that pre-aging of an age-hardenable alloy at a temperature (*i.e.* 100℃) lower than the final aging temperature (*i.e.* 150 or 177℃), causes the formation of a dense GP zones structure with a very fine and closely-spaced distribution within the matrix (see section 2.3.2). These pre-aging GP zones are beneficial for accelerated nucleation of higher numbers of η' precipitates during the final artificial aging treatment, especially for high temperatures such as 177℃ [35], [50], [85], [86].

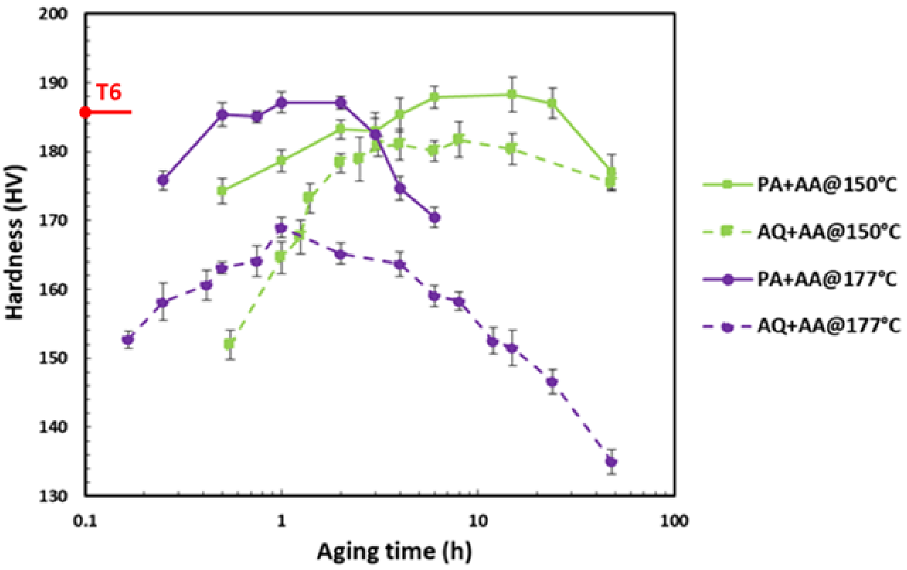

Figure 4.3. Effect of direct aging (AQ+AA) and multi-step aging (PA+AA) on the hardness of AA7050 alloy during aging at 150 and 177°C.

4.1.2.2. DSC results

In order to investigate the changes in the precipitation state during the various aging routes, DSC tests were conducted on the direct-aged and multi-step aged samples at their peak aged condition as well as on samples immediately following natural aging as well as the two-step pre-aging process of 2 days natural aging followed by 4 hours aging at 100°C. DSC analysis of each individual aging process is separately explained in the following subsections. The relationship between the hardness evolution and DSC results is also discussed.

Direct aging

The comparison of the DSC thermograms of the as-quenched and directly-aged materials, shown in Figure 4.4, highlights the following findings (in correlation with the hardness results in Figure 4.3):

- The first two exothermic peaks (A) and (B) on the DSC trace of the as-quenched material are not present on the DSC traces of the aged specimens which suggests that the phases associated with these two peaks (GP zones and η' precipitates) have already been formed during aging prior to the DSC run and are most likely responsible for the maximum strength.

- The endothermic troughs starting from 150℃ on the DSC traces of the aged samples (*i.e.* C) can be attributed to the dissolution of existing precipitates that have been formed prior to the DSC test.
- The dissolution event (C) has shifted to a higher temperature on the DSC trace of the sample aged at 177℃ compared to that of 150°C. This shift in temperature suggests that aging at 177℃ results in the formation of larger precipitates. Since the peak aged condition commonly represents the state of the highest volume fraction of precipitates, a larger precipitate size would suggest larger average spacing between precipitates and thus lower hardness [1]. This interpretation matches well with the reduced peak hardness of the sample direct aged at 177°C compared to 150°C (Figure 4.3).
- The smaller area associated with the dissolution trough (C) in the DSC trace of the sample aged at 177℃ may indicate that a lower volume fraction of precipitates has been formed during aging prior to the DSC run. This interpretation is consistent with the following theoretical consideration: according the curvature of solvus line in the phase diagram and the lever rule [53], [87], the volume fraction of precipitates that form within the matrix during aging at the higher temperature of 177°C is lower than that for 150℃. In addition, the matrix supersaturation and therefore, the driving force for precipitation are reduced for aging at 177°C. As a result, during aging at the higher temperature of 177°C, the precipitation capacity of the matrix is smaller. Moreover, the lower potential of the matrix for precipitation at higher aging temperature of 177°C leads to a more solute-rich matrix which may have given rise to the small exothermic peak between 110 and 160℃ (as indicated by the arrow) on the DSC trace of the sample aged at 177℃.

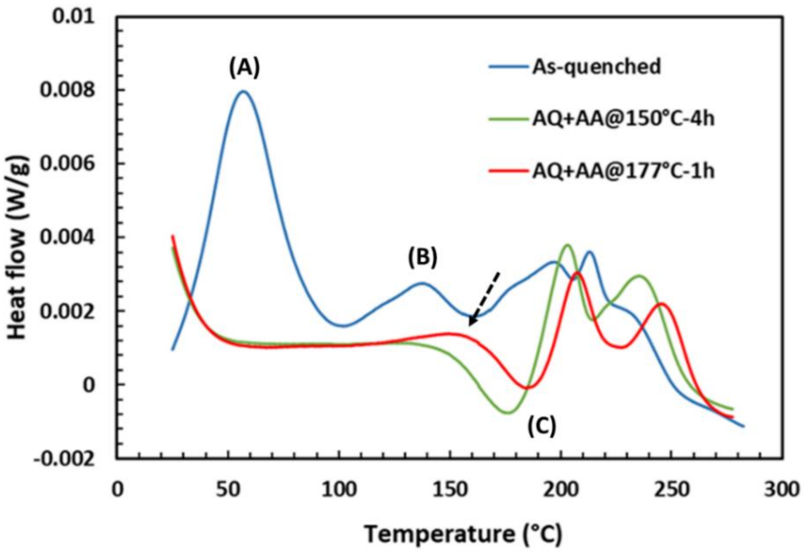

Figure 4.4. Comparison of the as-quenched DSC trace and the DSC thermograms of the directly-aged samples at 150 and 177°C up to the peak aged condition.

Multi-step aging

The comparison of the DSC traces of the multi-step aged samples at their peak aged condition with those of the pre-aged materials after one or two prior aging steps are presented in Figure 4.5, as follows:

- The absence of the first two exothermic peaks (A) and (B) on the DSC traces of the peak-aged materials, suggests that GP zones and η' precipitates have already been formed in the matrix during aging prior to the DSC run and are responsible for maximum hardening.
- The temperature associated with the minimum heat flow of the endothermic trough (C) is shifted to a higher temperature for the pre-aged sample that was aged at 177°C compared to 150 °C . Although in both cases, nucleation happens during pre-aging at 100°C, precipitates are still larger during final aging at higher temperature of 177°C compared to 150°C.
- The areas associated with the dissolution reaction (C) on the DSC traces for 177°C and 150°C are similar in magnitude.
- Another observation is the small exothermic peak on the 177°C DSC trace between 130°C and 160°C (indicated by arrow). It is speculated that the higher aging temperature of 177°C, may have dissolved some of the pre-aging GP-zones resulting in a more solute-rich matrix

and thus precipitation during the DSC run. This understanding explains the observed exothermic peak on the DSC trace of 177°C aged sample.

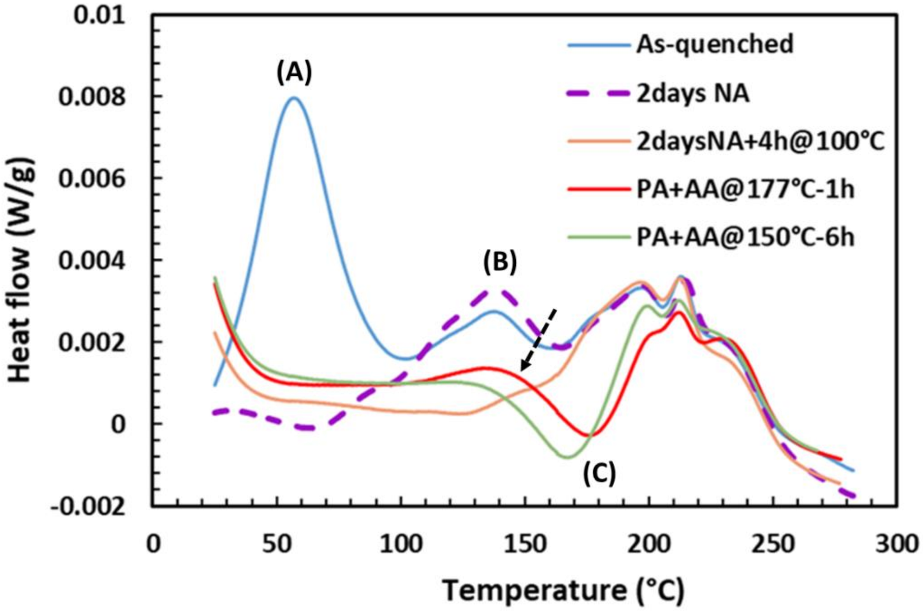

Figure 4.5. The DSC thermograms of the multi-step aged samples at 150 and 177°C up to the peak aged condition along with the DSC traces of: As-quenched, 2days naturally-aged and 2days naturally aged + 4h @ 100°C samples.

4.1.2.3. IC results

To study the precipitation kinetics associated with the direct and multi-step aging processes, isothermal calorimetry tests were done on the as-quenched and the pre-aged AA7050 aluminum alloys at the defined temperatures (see Table 3.3). The data recorded during the first 500 seconds of aging was considered to be erroneous, since the calorimeter was disturbed by the introduction of the sample. Therefore, each trace was corrected by subtracting this initial time shift (500 s) from the time axis of the trace, *i.e.* $t_{final} = t - 500$. As reported by Esmaeili *et al.* [1], [2], [71], the precipitation process gives rise to an exothermic peak (which is a representation of the released heat) during the IC runs. The exothermic peak rises to a maximum point, then gradually decreases and eventually reaches the baseline after the reactions are complete or the released heat becomes too small to be distinguished. It is reported that the time associated with reaching that final level of the released heat (t_f) is very close to the time to reach the peak aged condition at the aging temperature [71]. For the current measurements, t_f was taken as the time at which the heat flow dropped below $(5-10)\times 10^{-5}$ W/g. Isothermal calorimetry results for the direct and multi-step aged materials are presented separately in the following sections.

Direct aging

Figure 4.6 shows the resultant IC traces of the as-quenched AA7050 at various aging temperatures. According to Esmaeili *et al*. [71], the area under each IC trace ($\int_0^{t_f} \frac{dQ}{dt}\,dt$) represents the total heat released due to the precipitation reactions. The values of t_f and total heat released obtained for each temperature are listed in Table 4.1.

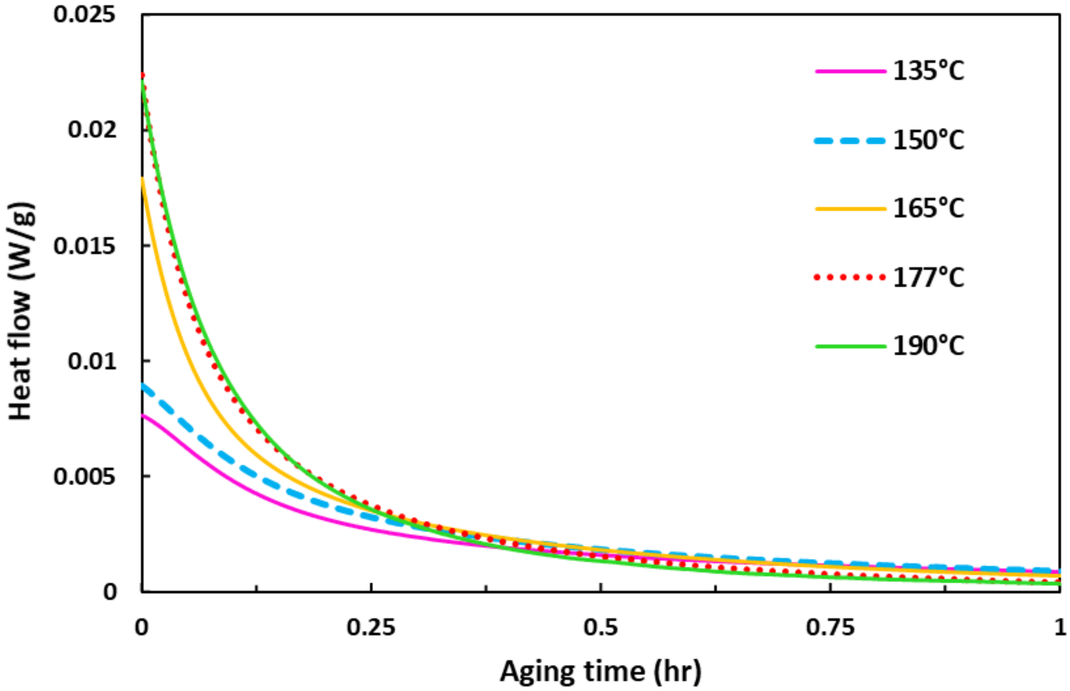

Figure 4.6. The isothermal calorimetry traces for the as-quenched AA7050 during aging at various temperatures.

Table 4.1. Isothermal calorimetry data for direct aging of AA7050: t_f and the corresponding total heat released during aging.

Temperature (℃)	t_f**(h)**	**Total heat (J/g)**
135	8	12.3
150	5	12.6
165	3	12.4
177	2	12.3
190	1	11.5

It is obvious from the above table that the t_f values have a decreasing trend with respect to the aging temperature, However, the total heat released during aging for t_f are very similar for all testing temperatures.

Multi-step aging

The isothermal calorimetry results of the pre-aged AA7050 in the temperature range of 135-177℃ are shown in Figure 4.7. The values obtained for t_f and the corresponding total heat released are listed in Table 4.2.

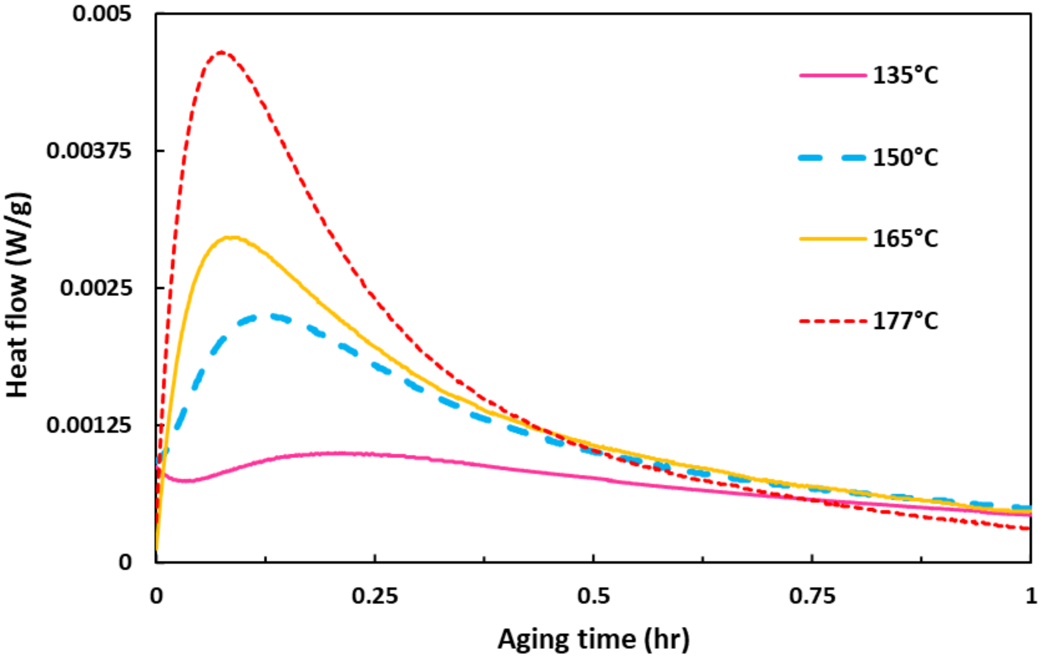

Figure 4.7. The isothermal calorimetry traces of the pre-aged AA7050.

Table 4.2. Isothermal calorimetry data for multi-step aging of AA7050: t_f and the corresponding total heat released during aging

Temperature (℃)	**t_f(h)**	**Total heat (J/g)**
135	8.6	5.02
150	5.6	6.4
165	3.2	6.1
177	1.6	6.4

Similar to the direct aging case, it is shown in the above table that the t_f values have a decreasing trend with respect to the aging temperature, while the heat released for t_f are almost similar for all testing temperatures in the current range.

4.2. Effect of deformation on age hardening – AA7075

The focus of this section is to report the experimental investigation on the effects of deformation, through warm-forming (WF), on the aging response and precipitation behavior of the pre-aged (PA) AA7075. The hardness measurements, DSC and IC results, along with the corresponding discussion will be presented. The heating profile of the warm forming stage and the details of the entire heat treatment process are summarized in Section 3.2.2, Figure 3.2.

4.2.1. Hardness test results

Figure 4.8 shows the hardness test results for the PA and PA+WF AA7075 samples considering the final artificial aging at 177°C. For reference, the WF cycle comprised heating to 150℃ and deforming the sample to 10% strain.

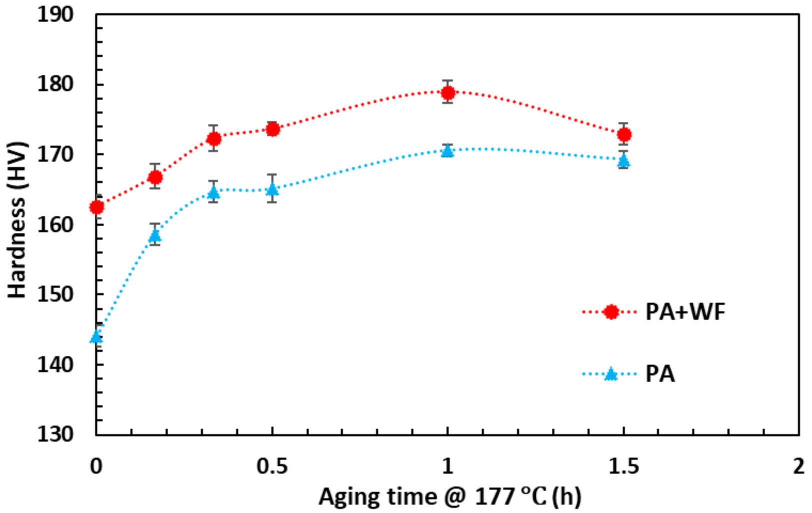

Figure 4.8. Influence of the pre-straining on the evolution of microhardness of AA7075 during ageing at 177°C.

As Figure 4.8 shows, the hardness values of the warm-deformed material (PA+WF) are higher than those for the non-deformed material (PA) during aging at 177°C (up to 1.5 hours tested). To a good approximation, the hardness value of the as-deformed material is 18 HV (~55 MPa) higher than the hardness value for the as-PA alloy (*i.e.* 162 vs. 144 HV), which is more likely due to the strain hardening effect caused by the generation of dislocations at the warm-forming stage as well as potentially, some increased solid solution hardening. The increased solid solution hardening is explained according to the possible dissolution of some pre-aging GP zones during the forming procedure [55]. Reportedly, a proportion of small GP zones are sheared by dislocations during the forming stage [15], [20] and therefore their size becomes smaller than the critical size for their survival (stability). The GP zone dissolution during the forming stage will be also discussed in Section 4.2.2 through comparing the DSC results of the PA and PA+WF materials shown in Figure 4.9. Additionally, this dissolution effect can be inferred from the comparison of the evolution of the relative volume fraction of precipitates obtained from the IC tests (performed at 177℃) on both PA and PA+WF materials: As will be presented in Figure 5.17, Section 5.3.1, the volume fraction of precipitates for the PA+WF material at the start of aging at 177°C, is ~ 20% less than that for the PA material, which can be due to the GP zone dissolution during the warm-forming stage prior to the IC run.

As a result of the GP zones dissolution, some of the solutes are brought back into solution which increases the solid solution hardening while decreasing the precipitation hardening contribution at the early stages of aging at 177°C (due to the reduced volume fraction of precipitates).

However, the difference between the hardness of the PA and PA+WF materials decreases from the initial 18 HV to ~8 HV (~ 25 MPa) within 10 minutes of aging at 177°C and remains the same until the peak-aged condition is achieved. The smaller difference between the hardness values of the PA and PA+WF materials for the later stages of aging, can be due to potential dislocation recovery and associated reduction of strain hardening. The higher hardness of the deformed material for the later stages of aging, can be due to the combination of the remaining strain hardening and the improved precipitation hardening contribution due to the dislocations [16]. The latter case can be explained from the calorimetry results which will be presented in Figure 5.17, Section 5.3.1. According to Figure 5.17, despite the lower volume fraction of precipitates at the start of aging at 177°C in the PA+WF material compared to the PA condition, the PA+WF material achieves similar precipitation rate and volume fraction as the PA material within ~ 2 minutes of aging at 177°C. It is speculated that this effect is due to the increased driving force for precipitation (due to the GP zone dissolution during the WF process), as well as the presence of dislocations acting as effective heterogeneous nucleation sites [14], [15], [55], [88], which have improved the precipitation hardening contribution of the PA+WF material during the artificial aging process.

Also, it can be observed in Figure 4.8 that the peak hardening for both deformed and non-deformed materials is achieved after 1 hour of aging at 177°C. This similarity in peak aging time may be due to the following concurrent phenomena that balance each other's effects:

(i) Increased supersaturation of the matrix leading to the increased driving force for precipitation; this effect is due to the dissolution of some pre-aging GP zones during the warm-forming stage. Indeed dislocations can assist with dissolving more GP zones during the forming procedure [55]. Furthermore, partial, or complete dissolution of precipitates may occur due to shearing by dislocations [15], [20].

(ii) Dislocations are favourable nucleation sites and the precipitates, η' for instance, can nucleate more readily on dislocations, since the free energy change that is required for nucleation is substantially reduced [51].

(iii) The presence of dislocations acting as vacancy sinks [16], [17], may lead to the reduction of vacancy concentration as well as the dissolution of some GPII zones that are mostly considered as vacancy rich clusters [41], [89].

Therefore, there are a number of offsetting factors controlling the rate of precipitation: the precipitation rate increases because of the first two factors, *i.e.* (i) and (ii), while it slows down because of the progressive annihilation of vacancies (iii) that could have assisted the precipitation process.

Additionally, the faster reduction of the peak hardness at longer aging times in the PA+WF material compared to the PA material, can be due to the accelerated precipitate coarsening in presence of dislocations. Similar results are also reported in previous studies [15], [16] in which dislocations are fast diffusion paths leading to accelerated precipitate coarsening via pipe diffusion and solute transportation toward dislocations.

It is worth mentioning that Abolhasani [90] has also investigated the hardness evolution during PBC of the PA-AA7075 material and has found similar trends. However, the alloys used in Abolhasani's work and the current study, are not from the same material batch.

4.2.2. DSC results

To identify the changes induced by dislocations on the precipitation characteristics, DSC tests were performed on the pre-aged (PA) [90] and pre-aged and warm-deformed (PA+WF) samples prior to final aging at 177°C. The resultant DSC traces of the PA and PA+WF materials are represented in Figure 4.9.

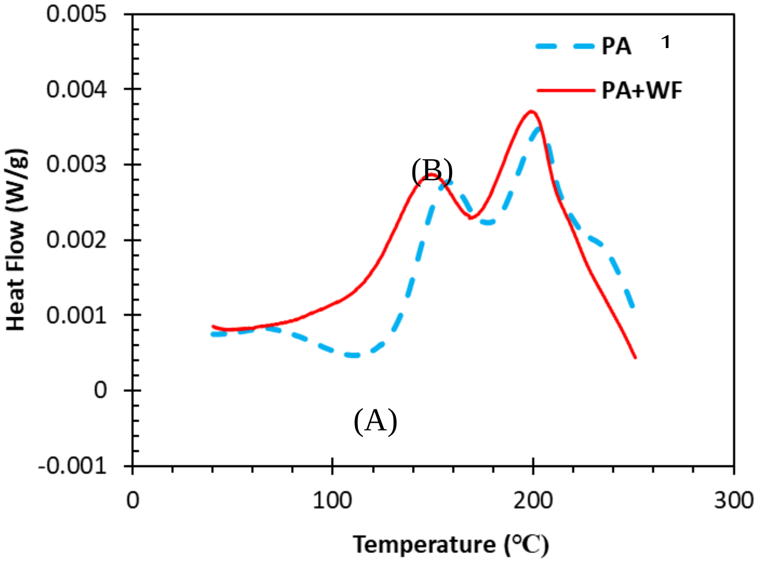

Figure 4.9. The DSC traces of the pre-aged AA7075 before and after warm forming at 150°C.

---

[1] Data provided by Abolhasani [79]

The initial plateau that appears on both DSC traces can be due to the balance between dissolution and precipitation effects cancelling out the resultant endothermic and exothermic peaks, respectively. However, the presence of dislocations induces some differences in the transformation process, as discussed below:

- The endothermic trough (A) on the DSC trace of the PA material (the dotted line) can be attributed to the dissolution of the GP zones that have been formed during the pre-aging stage prior to the DSC run [9], [13]. This endothermic event is not observed on the DSC trace of the PA+WF material (the solid line). This result may suggest two possible reasons: (i) possible dissolution of some pre-aging zones (GP zones) during the warm-forming process and with the assistance of dislocations prior to the DSC run, (ii) the presence of larger precipitates in the matrix that do not dissolve during the DSC run. Indeed, enhanced solute diffusion and precipitate growth due to the short-circuit diffusion along the dislocation core [15], [16], [51] could have caused the precipitates to be larger and more resistant to dissolution during the DSC run.
- The exothermic peak (B) (∼150°C), is more likely related to the formation of η' during the DSC run [8], [16]. This exothermic peak has shifted to a lower temperature in the case of the PA+WF material (the solid line). One may interpret this temperature shift as a result of accelerated formation of η' in presence of dislocations during the DSC run [55]. However, another possible reason for this phenomenon is that the location of peak (B) in the pre-aged material is determined by the overlap of the exothermic and endothermic events, while in the PA+WF material, since the endothermic event is not sufficiently strong to overlap with the exothermic peak, the exothermic peak does not shift to higher temperatures and happens earlier.

4.2.3. IC results

To quantify the effect of deformation on the precipitation kinetics, IC tests were performed at temperatures in the range of (150-177°C) on the as-quenched, pre-aged (PA) and pre-aged + warm-deformed (PA+WF) AA7075 samples (see Table 3.3). Similar to Section 4.1.2.3, the resultant IC test data was analyzed using Esmaeili *et al.*’s approach [71]. The IC traces at the three aging temperatures are shown in Figure 4.10. Each trace is corrected by subtracting the initial 500 seconds from the time axis of the trace, i.e. $t_{final} = t - 500$, as discussed in Section 4.1.2.3.

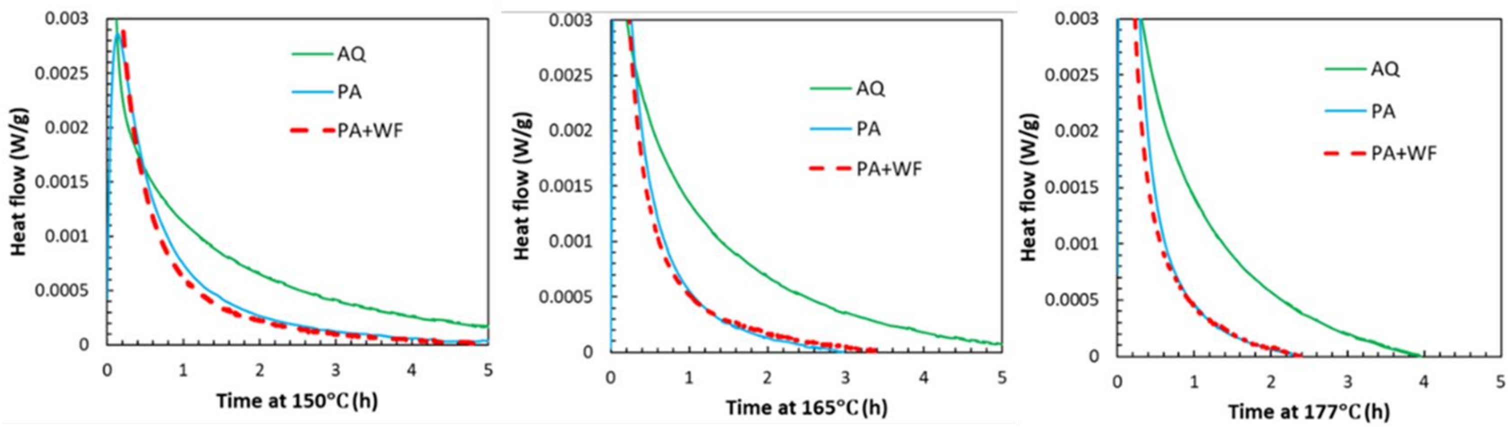

Figure 4.10. The isothermal calorimetry results for artificial aging of As-quenched, PA and PA+ WF AA7075 samples at the temperatures of (a) 150, (b) 165 and (c) 177°C.

The t_f value, *i.e.* time to reach the baseline, is considered the time when the heat flow dropped below $(1.5 - 3.5) \times 10^4$ W/g. The area under each IC trace, which represents the volume fraction of precipitates [71], can be used to compare the extent of precipitation in the deformed and non-deformed AA7075 specimens. Table 4.3 lists the approximate t_f values and the total heat released during the IC tests of PA and PA+WF materials at three aging temperatures. The data in Table 4.3 represent the average values of at least 3 repeats per condition.

Table 4.3. The values of t_f and the total heat released obtained from the IC experiments conducted on PA and PA+WF AA7075 materials.

Temperature (°C)	Pre-aged alloy (PA)		Pre-aged +Warm-formed alloy (PA+WF)	
	t_f(h)	**Total heat (J/g)**	**t_f(h)**	**Total heat (J/g)**
150	6 (±0.3)	8.8 (±0.0)	5.5 (±0.8)	9.3 (±0.7)
165	3 (±0.3)	8.4 (±0.5)	3.4 (±0.6)	9.4 (±0.8)
177	2.4 (±0.2)	9.1 (±0.6)	2.5 (±0.3)	10.4 (±0.2)

As listed in Table 4.3, the t_f values are almost similar for the deformed and non-deformed materials. This observation is consistent with the hardness results in Figure 4.8 which shows a similar time to reach the peak hardness for the final aging at 177°C for the deformed and non-deformed materials. However, the total heat released (the areas) associated with aging of the PA+WF materials, are slightly larger than those for the PA material for all testing temperatures. The slight increase in the total heat released (*i.e.* the volume fraction of precipitates) in the deformed material can be related to the potential errors involved in analysing the IC results [2]. Otherwise, this effect can be due to the presence of dislocations that promotes heterogeneous precipitation. In addition, the possible dissolution of some pre-aging GP zones during the warm-forming process, could have enriched the matrix with the solute atoms and thus enhanced its capacity for precipitation during the IC run, (as was also discussed in section 4.2.1, *i.e.* the hardness results). The latter possibility was also mentioned in section 4.2.2 (the DSC results) as one of the probable reasons for having a smaller area associated with the endothermic event in the DSC trace of the PA+WF material compared to the PA material (see Figure 4.9).

It is worth mentioning that Abolhasani [90] has also performed IC tests on the as-quenched and the pre-aged AA7075 material and found trends similar to the current results. However, the alloys used in Abolhasani's work and the current study, are not from the same material supply batch.

4.3. Summary and concluding remarks

In this chapter, the effects of various aging practices on the precipitation hardening response of the AA7050 have been presented and discussed. Also, the aging behaviour of AA7075 in presence of dislocations induced by the warm-forming process has been analyzed. The acquired knowledge is used to analyse the precipitation kinetics and modeling of yield strength during the various heat treatment and processing. This modeling work is presented in the next chapter.

5. Modeling analysis

Modeling of the precipitation kinetics and hardening of the current alloys is pursued based on the approaches developed by Esmaeili *et al.* [1], [2] and Cheng *et al.* [5]. According to Esmaeili *et al.* [1], [2], the evolution of the relative volume fraction of precipitates (f_r), is predicted and then utilized to model the yield strength of the alloys during various heat treatments. The basic relationships for yield strength modeling for the cases with or with out the dislocation hardening contribution have been described in Section 2.4.

In the current section, the viability of the weak obstacle formulation [1] is expanded by developing a new model which predicts the precipitate radius during aging as a function of the relative volume fraction of precipitates. Also, based on the physical concepts and existing theories regarding the effects of dislocations on the precipitation kinetics, the original kinetic model [2] is expanded to account for the effect of deformation, in the context of warm-forming, on the precipitation kinetics. The results of the precipitation kinetic analysis and the yield strength modeling of each heat treatment and warm-forming procedure are separately presented in the following sections.

5.1. Precipitation kinetics – No deformation

5.1.1. Basic modeling approach

Variations of the relative volume fraction of precipitates (f_r) during artificial aging of the pre-aged alloys are modeled based on Eq. (5.1) [2]:

$$f_r = 1 - (1 - f_r^0)\, exp[-\textstyle\sum_i k_{iv}^n (t_i^n - t_{i-1}^n)] \qquad (5.1)$$

in which, $f_r = \frac{f}{f_{peak}}$ is the relative volume fraction of precipitates at artificial aging time t_i, f_r^0 is the relative volume fraction of precipitates at the start of each artificial aging step (*i*), k_{iv} is the temperature dependent constant value describing the reaction rate and *n* is a time exponent mostly defined as a shape factor. In cases in which the *n* value varies during aging, it should be presented as n_i [2].

The rate constant k_{iv} has an Arrhenius relationship with temperature [1]:

$$k_{iv} = k_{0v} exp\ (\frac{-Q_v}{RT_i}) \qquad (5.2)$$

in which, k_{0v},Q_v, R, and T_i are the frequency factor, apparent activation energy, the universal gas constant (8.314 $\frac{kJ}{mol.K}$), and the process temperature, respectively.

Eq. (5.1), which was originally developed for multi-step and non-isothermal aging processes [2], is considered here as a general relationship that is capable of describing the precipitation kinetics upon direct-aging (where $f_r^0 = 0$) and isothermal conditions, as well.

Direct aging

To model the evolution of the relative volume fraction of precipitates (f_r) during a direct aging process (*i.e.* $f_r^0 = 0$), Eq. (5.1) is reduced to a modified JMAK [61]–[63] equation:

$$f_r = 1 - exp\ (-k_v t)^n \qquad (5.3)$$

For this isothermal process, the relative volume fraction of precipitates (f_r) during direct aging can be experimentally determined using IC data, according to Eq. (5.4) [71]:

$$f_r = \frac{\int_0^t \frac{dQ}{dt} dt}{\int_0^{t_f} \frac{dQ}{dt} dt} \qquad (5.4)$$

Multi-step aging - isothermal condition

To describe the evolution of f_r during isothermal artificial aging of the pre-aged material in the presence of pre-existing precipitates, Eq.(5.1) is expressed as [2]:

$$f_r = 1 - (1 - f_r^0)\ exp(-k_v t)^n \qquad (5.5)$$

The experimental values of the relative volume fraction of precipitates during artificial aging of a pre-aged material are determined through IC and based on the approach introduced in reference [2]. Assuming that the precipitate content of the artificially aged material is solely dependent on the artificial aging temperature (i.e. the metastable phase diagram), the values of f_r can be calculated as [2]:

$$f_r = f_r^0 + \frac{f_{V|AA}}{f_{V|peak}} \qquad (5.6)$$

in which, $f_r = \frac{f_V}{f_{V|peak}}$ and $f_r^0 = \frac{f_{V|PA}}{f_{V|peak}}$. The second term on the right hand side of Eq.(5.6) is determined from the isothermal calorimetry experiments conducted on both pre-aged and as-quenched materials [2]:

$$\frac{f_{v|AA}}{f_{V|peak}} = \frac{\int_0^t \frac{dQ}{dt} dt|_{PA+AA}}{\int_0^{t_f} \frac{dQ}{dt} dt|_{AQ+AA}} \tag{5.7}$$

in which, $\int_0^t \frac{dQ}{dt}\ dt|_{PA+AA}$ is the area under the IC trace up to time t for the pre-aged material and $\int_0^{t_f} \frac{dQ}{dt}\ dt|_{AQ+AA}$ is the area under the IC trace up to the peak aged condition for the as-quenched material. The f_r^0 value can be determined from the two equations of (5.7) and (5.6) for $t = t_f$ and $f_r = 1$ [2]:

$$f_r^0 = \frac{\int_0^{t_f} \frac{dQ}{dt} dt|_{AQ+AA} - \int_0^{t_f} \frac{dQ}{dt} dt|_{PA+AA}}{\int_0^{t_f} \frac{dQ}{dt} dt|_{AQ+AA}} \tag{5.8}$$

5.1.2. Direct aging

To determine the kinetic parameters of Eq. (5.3), *i.e.*, n and k_v, the experimental values of f_r obtained through Eq. (5.4) in the temperature range of 135-190℃ are used and $lnln\left(\frac{1}{1-f_r}\right)\ vs\ lnt$ is plotted. From a linear approximation in the range of 5-95% f_r, n and k_v parameters are obtained for each aging temperature and are listed in Table 5.1.

Table 5.1. Experimental values determined for *n* and k_v parameters for direct aging of AA7050.

Temperature (℃)	**n**	k_v **(**s^{-1}**)**
135	0.73	0.00031
150	0.80	0.00041
165	0.80	0.00080
177	0.80	0.00130
190	0.80	0.00140

It can be inferred from the above table that the n value for the direct aging of AA7050 has an average value of $n \approx 0.8$. Using the values of k_v reported in Table 5.1, the Arrhenius relationship of k_v with respect to the aging temperature (Eq. (5.2)) is plotted in Figure 5.1. The resultant kinetic parameters obtained for the direct aging of AA7050 are listed in Table 5.2. It should be noted that the activation energy obtained from this analysis is an apparent value, as explained in prior works by Berkenpas [91] and Esmaeili *et al.* [1].

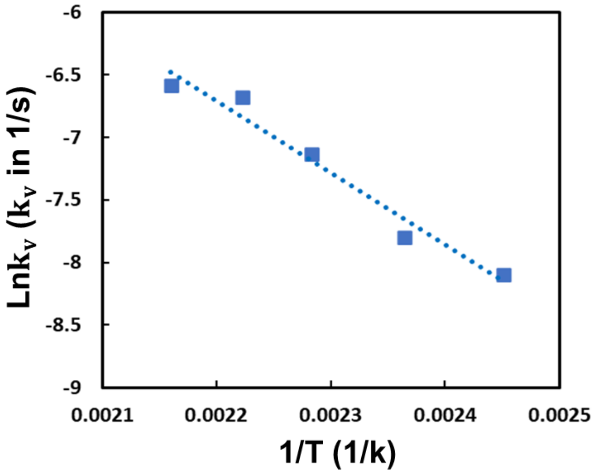

Figure 5.1. Arrhenius plot for the direct-aging of AA7050.

Table 5.2. The kinetic parameters determined for direct aging of AA7050.

Parameter	**Value**
n	0.8
Q_v (kJ/mol)	48
k_{0v} (s^{-1})	3.6×10^2

Having obtained the kinetic parameters, the evolution of f_r obtained through Eq. (5.3), along with the experimental values of f_r obtained from the IC tests, *i.e*. Eq. (5.4), are compared in Figure 5.2. It is apparent that there is a reasonable agreement between the experimental results and the model (Eq. (5.3)), which provides the input data required for the yield strength model.

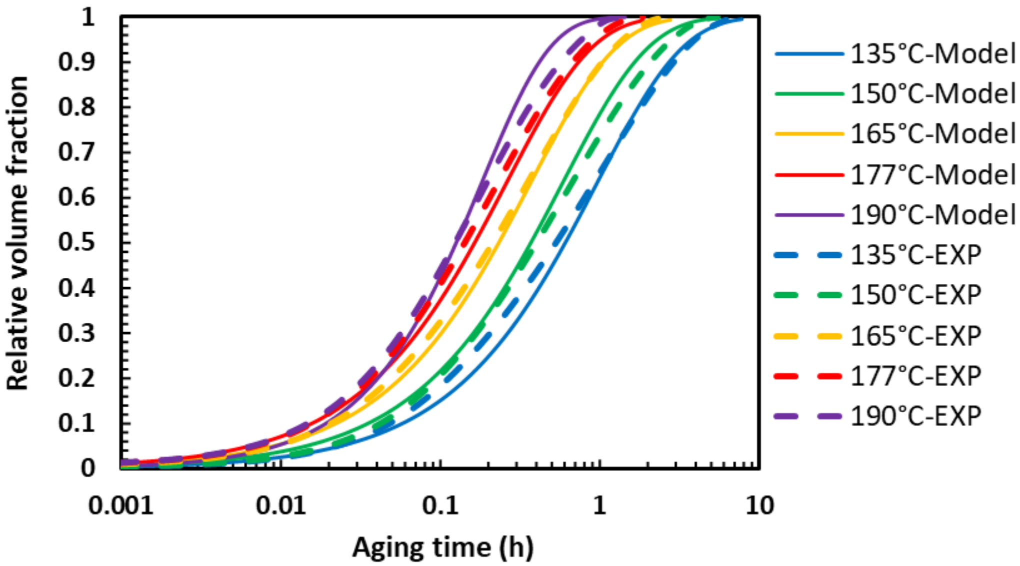

Figure 5.2. Comparison of the f_r values obtained through the kinetic model with the values acquired from the calorimetry results for direct artificial aging of AA7050.

The apparent activation energy of the current direct-aging process, *i.e.* 48 kJ/mol, has a relatively lower value in comparison to the values reported for 7000- and 6000-series aluminum alloys [1], [39], [89]. This result suggests that the formation of vacancy rich clusters after a fast quench, promotes and facilitates GP zone formation, more specifically GP II zones, during direct-aging which leads to a low activation energy value. This view is also supported by Ferragut *et al.* [89] who claimed that upon applying a rapid quench, the starting time of precipitation is predominantly related to the amount of solute-vacancy pairs. In the current case, the apparent activation energy value (48 kJ/mol) is similar to the value obtained through atomistic simulations for the migration energy of Mg into the nearest neighbour vacancy in Al–Mg alloys (*i.e.* 0.51 eV ≅ 49 kJ/mol) [92], [93]. These arguments suggest that the direct-aging process is accelerated by solute diffusion assisted by the presence of excess vacancies paired with solute atoms within the matrix.

So far in this section, the kinetics of direct-aging have been analyzed through existing theories and modeling approaches. However, the next section serves to provide additional insight into precipitation kinetics associated with direct aging: for this purpose, a calculated TTT diagram from the literature [45] is used to consider the sequential nature of the precipitation process.

Analysis of the TTT diagram

The kinetics of transformation is dictated by the net temperature-dependent phenomena of (a) atomic mobility (growth) and (b) driving force for nucleation [91]. It is generally assumed that at high temperatures the overall transformation kinetics are dominated by the growth component (the driving force for nucleation is reduced at relatively high aging temperatures) [53]. In contrast, the rate of solute diffusion is low at lower temperatures, and therefore precipitation kinetics may be controlled by a faster nucleation process due to a higher driving force for the process.

The TTT diagram reported by Chinella and Guo [45] for AA7075 was shown in Figure 2.7, Section 2.3.1. It is assumed that this TTT diagram can provide appropriate description for the precipitation process in AA7050 as well. It is also assumed that precipitates are transiting continuously during direct aging from GP zones to η' precipitates. The current aging temperatures (except for 135°C) correspond to the upper part of the GP zones formation C-curve (See Figure 2.7). Considering these understandings, to further elaborate the dominant mechanism during the direct aging process, the following analysis is provided:

According to the TTT diagram (Figure 2.7), one can hypothesize that each direct-aging process can be divided into two continuous stages of GP zones and η' formations:

(i) 1st stage of aging starts from t = 0 to t = $t_{\eta'}$: GP zones are the only precipitates present in the matrix during early stages of aging up to the specific time ($t_{\eta'}$) at each aging temperature. $t_{\eta'}$ is the time when the η' precipitates start to nucleate within the matrix or on the existing GP zones. The formation of GP zones may extend beyond the first stage and be completed at the end of aging time t_f. Due to the dominance of homogenous nucleation of GP zones in the first stage of aging, it can be postulated that nucleation of new nuclei is the controlling mechanism in the first stage of aging.

(ii) 2nd stage of aging starts from t = $t_{\eta'}$ to t = t_f: η' precipitation starts in presence of the existing GP zones. A considerable number of studies have highlighted the heterogeneous nature of η' nucleation. It is believed that η' precipitates either nucleate on the existing GP zones, or form by the growth of GP zones in one preferred direction (elongated phases) or even result from an in situ transformation of GP zones [33], [39], [50]. Hence, it can be suggested that the second stage of aging is controlled by both nucleation and growth components.

According to the TTT diagram (Figure 2.7), the $t_{\eta'}$ values, *i.e.* the η' starting times, have a decreasing trend with respect to temperature for temperatures below the knee of the η' curve (*i.e.* 300℃). In other words, as the aging temperature increases, η' nucleates faster. Table 5.3 provides the $t_{\eta'}$ values corresponding to each aging temperature.

Table 5.3. η'starting times ($t_{\eta'}$) at each aging temperature.

Temperature (℃)	135	150	165	177	190
$\boldsymbol{t_{\eta'}}$**(s)**	6000	2900	1700	900	550

For the current AA7050 alloy, the relative volume fraction of precipitates during the first stage of aging for each aging temperature, designated as f_r^1, can be determined using the IC test results as:

$$f_r^1 = \frac{f_{v(t=0\,:t=t_{\eta'})}}{f_{v(peak)}} = \frac{\int_0^{t_{\eta'}} \frac{dQ}{dt} dt}{\int_0^{t_f} \frac{dQ}{dt} dt} \qquad (5.9)$$

Where $f_{v(0:\,t_{\eta'})}$ is the volume fraction of GP zones at $t_{\eta'}$ and $f_{v(peak)}$ is the volume fraction of precipitates at the peak aged condition which can be a mixture of GP zones and η'. The values of f_r^1 corresponding to each aging temperature are listed in Table 5.4.

Table 5.4. the values of relative volume fraction of precipitates up to $t_{\eta'}$.

Temperature (℃)	135	150	165	177	190
$\boldsymbol{f_r^1}$	0.8	0.7	0.7	0.7	0.6

It can be inferred from f_r^1 values in the above table that a high portion of the precipitation process (more than 50%), specifically for the lower aging temperatures, consists of GP zone formation. Additionally, as the aging temperature increases, the duration of the first stage of aging becomes shorter and therefore the GP zone formation loses its dominancy. So, it is postulated that a higher volume fraction of η' precipitates is formed during aging at higher temperatures. The decreasing trend of f_r^1 with respect to the aging temperature also supports this idea.

The above mechanisms that is the dominancy of GP zone formation during the direct aging process, is reflected in the changes of the n value with temperature (Table 5.1): It has been suggested that the kinetic parameter n is a shape dependent factor [60]. Accordingly, the time exponent $n \approx 0.5$ corresponds to the spherical growth in the absence of impingement [60], [94], and $n \approx 1$ is for needle or plate shaped precipitates [60]. It is generally assumed that GP zones have a spherical morphology [39], [83] while η' precipitates are plate shaped [15], [35], [43], [75] or needle shaped structures [44]. Therefore, it is expected that the n value increases with temperature, *i.e.* starting from 0.5 for natural aging [94] and approaching unity for higher aging temperatures.

5.1.3. Multi-step aging

To apply the kinetic model (Eq. (5.5)) and find the kinetic parameters for the multi-step aging process under the isothermal condition, Eq. (5.5) is fitted to the experimental values of f_r using the IC data (obtained through Eq. (5.6)) and is written in the following form:

$$lnln\frac{(1-f_r^0)}{1-f_r} = nlnt + nlnk_v \tag{5.10}$$

By plotting Eq. (5.10) in the range of f_r^0 and 95%, a straight line can be fit to the resulting data points to determine the values of *n* and k_v (Table 5.5). It is worth mentioning that f_r^0 is found by obtaining the average of the values determined experimentally through Eq. (5.8) for each aging temperature (seeTable 5.6).

Table 5.5. Kinetic parameters *n* and k_v obtained for artificial aging of the pre-aged AA7050 alloy.

Temperature (℃)	**n**	$\boldsymbol{k_v\ (s^{-1})}$
135	0.9	0.00018
150	0.81	0.00031
165	1.1	0.00045
177	1.2	0.0008

As is presented in the above table, the time exponent *n* has a value in between 0.8-1.2 ($n_{average} \approx 1$) suggesting the dominancy of η' precipitates for the final artificial aging stage of AA7050 alloy. The resultant values of k_v are used to obtain the kinetic parameters k_{0v} and Q_v through Eq. (5.2). Figure 5.3 shows the Arrhenius plot from which the kinetic parameters are obtained (Table 5.6).

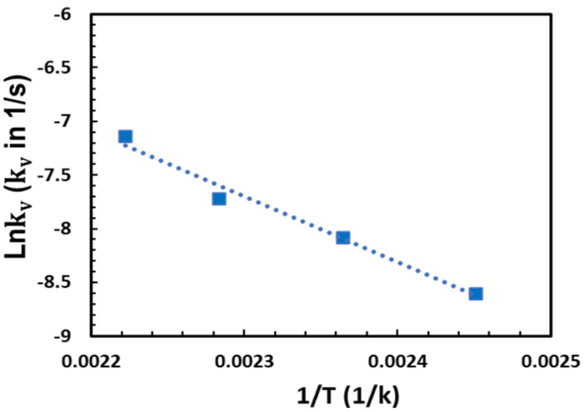

Figure 5.3. The Arrhenius plot for the final artificial aging of the pre-aged AA7050 alloy.

Table 5.6. Kinetic parameters obtained for the final artificial aging stage of the pre-aged AA7050 alloy.

Parameter	**Value**
n	1
f_r^0	0.52
Q_v (kJ/mol)	51
k_{0v} (s^{-1})	6×10^2

Having obtained the kinetic parameters, the model predictions for f_r (Eq. (5.5)) are compared with their respective experimental results (Eq. (5.6)) in Figure 5.4. The maximum difference between the experiment and the model is ~ 12% which is observed for the case of aging at 135℃ (the blue curve).

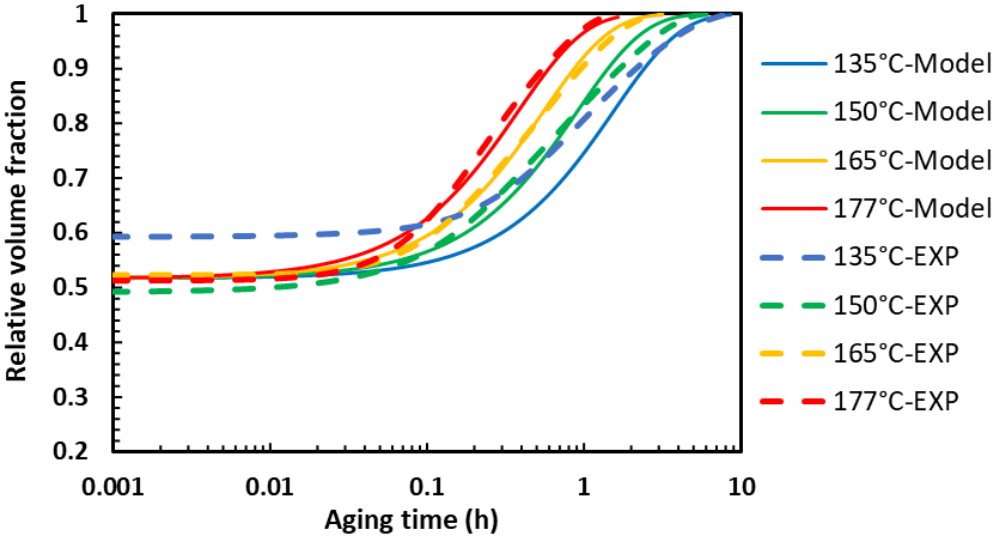

Figure 5.4. Comparison of the modeling and experimental results of relative volume fraction of precipitates for pre-aged AA7050 alloy.

As in the case of pre-aged 6000-series aluminum alloy [2], and considering the f_r^0 and *n* values (Table 5.6), it is proposed that the growth of the precipitates that form during the pre-aging stage, and not the formation of new nuclei, is more likely the dominant mechanism of precipitation during the final artificial aging step.

5.2. Yield strength – No deformation

5.2.1. Basic modeling approach

To model the evolution of yield strength during artificial aging process (up to the peak aged condition), the basic yield strength model [1] is applied:

$$\sigma_y = \sigma_i + \sigma_{ss} + \sigma_{ppt} \qquad (5.11)$$

where $\sigma_i = 10$ MPa [1], is the intrinsic strength of the pure aluminum matrix. The individual contributions of solid solution strengthening and precipitation hardening to the yield strength, *i.e.* σ_{ss} and σ_{ppt} (weak or strong obstacles) respectively, are defined as [1], [2]:

$$\sigma_{ss} = \sigma_{0ss}(1 - \alpha f_r)^{2/3} \qquad (5.12)$$

$$\sigma_{ppt|Strong} = C_1(f_r)^{1/2} \qquad (5.13)$$

$$\sigma_{ppt|Weak} = C_2(r f_r)^{1/2} \qquad (5.14)$$

where α is the fraction of initial solute concentration depleted from the matrix when f_r approaches unity and is assumed to be unity [1], σ_{0ss} is the contribution from the solid solution to the yield strength when the material is in the as-quenched state ($f_r = 0$), C_1 and C_2 are the constant parameters associated with the microstructural characteristics of the alloy in the peak-aged condition [1]. These parameters can be determined using the experimental values of the yield strength (and the precipitate radius at the peak aged condition for the weak obstacle case).

According to Eq. (5.13), the strong obstacle model is dependent only on the relative volume fraction of precipitates, while to apply the weak obstacle model, *i.e.* Eq. (5.14), knowledge of the precipitate radius is required. In addition, the weak obstacle model better suits the earlier stages of aging [1], and therefore may better define nucleation dominated aging processes. For the significance of the precipitate radius, *r*, in the implementation of the weak obstacle model, Eq. (5.14), a new equation is developed in the following section so that "*r*" can be easily predicted using the modeled f_r values. Accordingly, the developed model is described as the "nucleation-affected growth" model.

5.2.2. Modifications to extend the applicability of the basic model

5.2.2.1. Microstructural evolution

Nucleation- affected growth model

The focus of this section is to model the evolution of precipitate size during aging processes in which the nucleation phenomenon plays an important role in the artificial aging. The modeling approach is built based on the assumption of concurrent nucleation and growth of precipitates during the aging process. In other words, it is assumed that the precipitate number density (N) changes with respect to the aging time.

Starting with the well-known concept of the relative volume fraction of precipitates, f_r is given by [2]:

$$f_r = \frac{V_{ppt}}{V_{total}} = \frac{N\bar{V}}{V_{total}} \qquad (5.15)$$

in which, N and $\bar{V}$ are the number density and the average precipitate volume, respectively, at artificial aging time *t*.

Assuming a spherical morphology for precipitates, the average precipitate volume during aging is related to the average precipitate radius, r:

$$\bar{V} = \frac{4}{3}\pi r^3 \qquad (5.16)$$

Substituting the average volume per precipitate $(\bar{V})$ from Eq. (5.16), in Eq. (5.15) and rearranging, results in a proportionality between f_r and Nr^3 (*i.e.* $f_r \propto Nr^3$), which can be expressed in terms of precipitate radius and number density at time t_1 (r_1 and N_1) and at time t_2 (r_2 and N_2):

$$\frac{f_{r2}}{f_{r1}} = \frac{N_2 r_2^3}{N_1 r_1^3} \qquad (5.17)$$

Assuming that after a very short aging time, dt, the changes in relative volume fraction, number density and size of the precipitates are: df_r, dN and dr, respectively, Eq. (5.17) can be re-written as:

$$\frac{df_r+f_r}{f_r} = (\frac{dN+N}{N})(\frac{dr+r}{r})^3 \qquad (5.18)$$

or

$$1+\frac{df_r}{f_r} = (1+\frac{dN}{N})(1+\frac{dr}{r})^3 \qquad (5.19)$$

Expanding Eq. (5.19) gives:

$$1+\frac{df_r}{f_r} = (1+\frac{dN}{N})(1+(\frac{dr}{dt})^3+3\frac{dr}{dt}+3(\frac{dr}{dt})^2) \qquad (5.20)$$

Eq. (5.20) is mathematically simplified by neglecting the smallest multiplication products of $(\frac{dr}{dt})^3, (\frac{dr}{dt})^2, \frac{dN}{N}\times(\frac{dr}{dt})^3, \frac{dN}{N}\times\frac{dr}{dt}, \frac{dN}{N}\times(\frac{dr}{dt})^2$:

$$\frac{df_r}{f_r} = \frac{dN}{N}+3\frac{dr}{r} \qquad (5.21)$$

It is assumed that $\frac{dN}{N}$ relates to the radius of the critical size nucleus, r^*, according to the following equation [56]:

$$\frac{dN}{N} = \frac{dr}{r*-r} \qquad (5.22)$$

It is well known that $r^*$is inversely proportional to the driving force for nucleation ($r^* \propto \frac{1}{\Delta G_v}$) [53] . So, in cases in which supersaturation of the matrix is very high, the large driving force for nucleation results in an extremely small r^*. Hence, by substituting Eq. (5.22) in Eq. (5.21) and assuming $r^* \approx 0$, Eq. (5.21) is integrated as follows:

$$\int_{f_{r1}}^{f_{r2}} \frac{df_r}{f_r} = \int_{r_1}^{r_2} 2\frac{dr}{r} \qquad (5.23)$$

where $\qquad f_r(t) \le f_r \le 1$ and $r_t \le r \le r_{peak}$

Eq. (5.23) is then solved in the defined boundary conditions as:

$$ln(1) - lnf_r(t) = ln(r_{peak})^2 - ln\ (r_t)^2 \qquad (5.24)$$

Therefore:

$$ln\ (r_t)^2 = ln\ (r_{peak}^2 \times f_r(t)) \qquad (5.25)$$

Eq. (5.25) can be also expressed in a simplified form as:

$$r_t = \sqrt{f_r(t)} \times r_{peak} \qquad (5.26)$$

Eq. (5.26) is expressed, hereafter, as the "nucleation-affected growth model".

Nucleation-affected growth model validation

In this section, the validity of the nucleation-affected growth model is examined by applying it to two different 7000-series aluminum alloys with various aging histories: (a) AA7010, using published data in reference [95], and (b) AA7030, using the results of small angle x-ray scattering (SAXS) analysis conducted by Deschamps as part of a previous collaborative study [96]. The chemical compositions of the two alloys as well as the chemical composition of the current AA7050 are given in Table 5.7. It is worth mentioning that SAXS has been reported as a reliable method for quantifying microstructural evolution, *e.g*, precipitate size (which is usually given in terms of the Guinier radius) and integrated intensity, Q_i, during aging in 7000-series aluminum alloys [97].

Table 5.7. Chemical compositions of AA7050, AA7010 and AA7030 (wt%) [95], [96].

	Mn	Si	Cr	Mg	Ti	Cu	Zn	Fe	Zr
AA7050	0.01	0.03	0.01	2.04	0.02	2.15	6.44	0.04	0.11
AA7010 [95]	NG	0.1	NG	2.3	NG	1.5	6.5	0.1	0.1
AA7030 [96]	NG	NG	NG	1.22	NG	0.3	5.45	NG	NG

NG: the amount of is not given.

AA7010 alloy

SAXS measurement data for AA7010 during aging at 160°C [95] is used here. The chemical composition of the alloy is given in Table 5.7. The heat treatment process, as reported in the reference, consists of:

solutionizing at 475℃ → water quenching → 3days natural aging→ aging at 160℃.

The evolution of the Guinier radius and integrated intensity, Q_i, of the naturally-aged material during aging at 160°C are shown in Figure 5.5 [95]. Using the hardness data presented in reference [95], it is assumed that the peak aged condition is achieved after 3 hours of aging at 160°C.

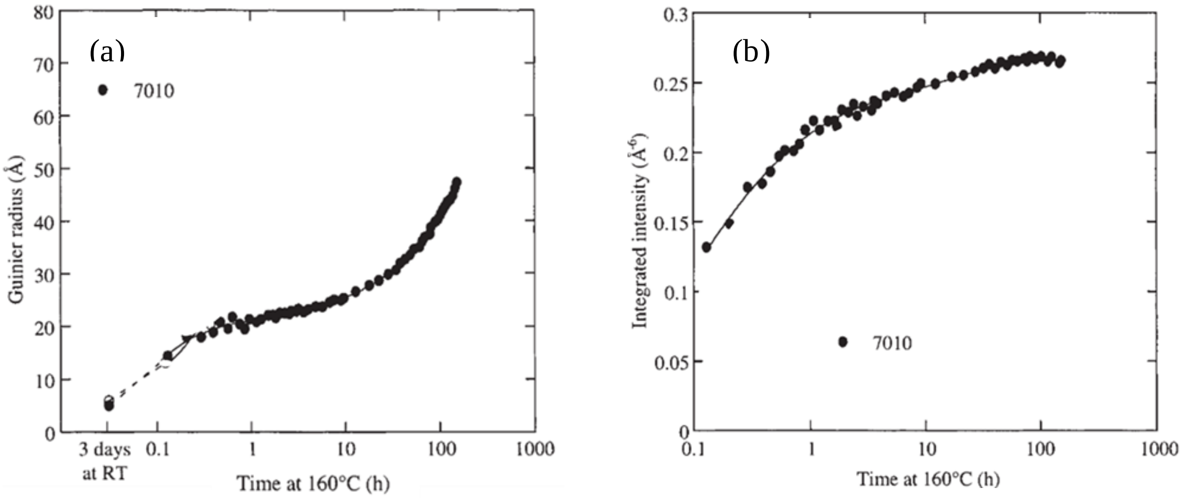

Figure 5.5. The results of SAXS experiments during aging at 160°C carried out after 3 days of natural aging on AA7010 alloy, (a) Guinier radius, (b) Integrated intensity [95].

Assuming the measured integrated intensity is proportional to the volume fraction of precipitates [95], the relative volume fraction, f_r, can be estimated as follows:

$$f_r = \frac{f_v}{f_{v\,peak}} \approx \frac{Q_i}{Q_{max}} \qquad (5.27)$$

in which, $Q_{max} = Q_{3h@160°C} \cdot f_r$, therefore, can be obtained using the data presented in Figure 5.5 (b).

It is also assumed that the Guinier radius, is a representation of the average precipitate size. Assuming that nucleation and growth of precipitates happen concurrently during aging at 160°C, the boundary conditions are defined as:

$$f^{o}_{r(3days\,NA)} < f_r \leq 1 \quad \text{and} \quad r_{(3days\,NA)} < r \leq r_{peak}.$$

Using Figure 5.5 (a), r_{peak} is approximated as the Guinier radius for the sample aged for 3 hours at 160 ℃, *i.e.* $r_{peak} = 21.5$ A°.

Using the above experimental values, Eq. (5.26) is implemented.

Figure 5.6 shows the comparison between the measured values of precipitate radius (*i.e.* Guinier radius) and the precipitate radius predicted by the nucleation-affected growth model (which includes f_r obtained through Eq. (5.27)). The reasonable agreement between the modeling and experimental results confirms the validity of Eq. (5.26) to estimate the precipitate size evolution during aging from the evolution of the relative volume fraction of precipitates during the final stage of a multi-step aging process in AA7010.

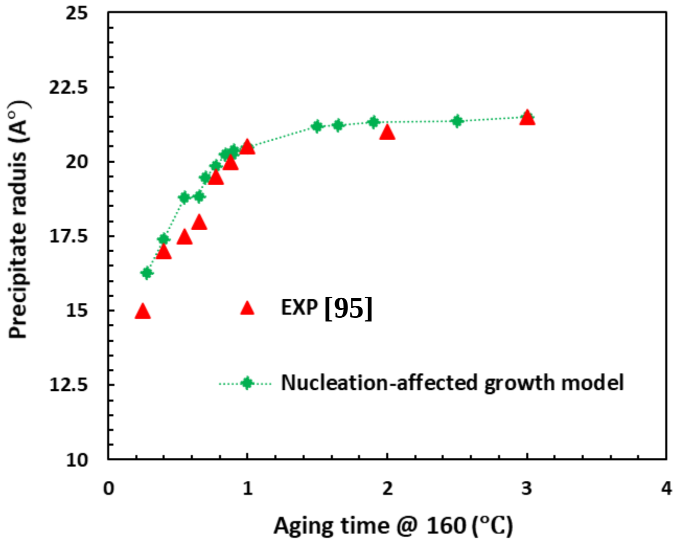

Figure 5.6. Comparison of the measured and predicted values of precipitate radius during aging of AA7010 at 160°C.

AA7030 Alloy

In a previous experimental study by Deschamps [96], a series of SAXS measurement were performed on AA7030 following two different multi-step aging routes, as shown in Table 5.8.

Table 5.8. Summary of the aging processes performed on AA7030.

Aging designation	**Aging route**
A	SHT & Water quenching + 24h NA+ 5h@100°C+ Aging @150°C
B	SHT & Water quenching + 1h NA+ 5h@100°C+15min@130°C+2h@177°C

The “nucleation-affected growth” model (Eq. (5.26)) is applied to each aging route and the results are presented separately in the following.

i. Aging route (A)

The evolution of the Guinier radius r and the integrated intensity Q_i were obtained through continuous SAXS measurement during pre-aging at 100°C followed by aging at 150°C. The results are shown in Figure 5.7 (a) and (b).

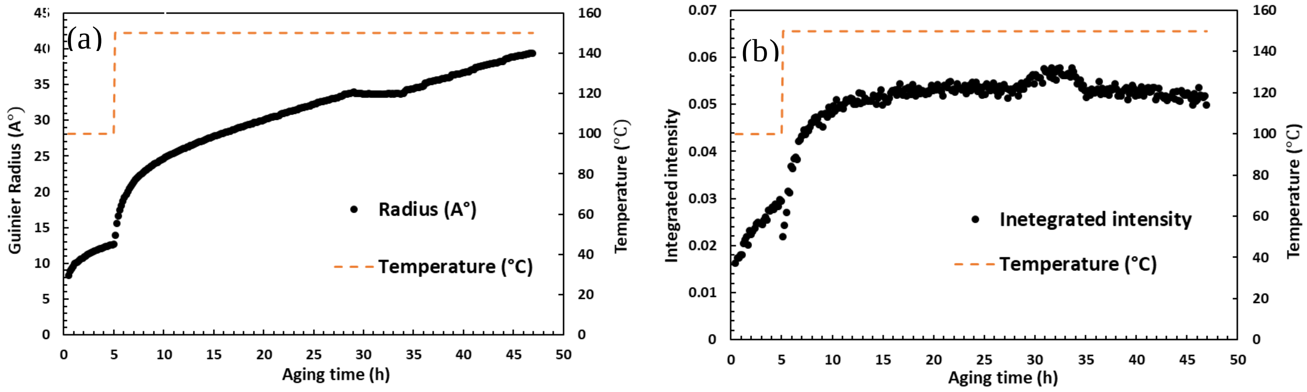

Figure 5.7. The results of the SAXS experiments conducted on AA7030 during pre-aging at 100°C followed by aging at 150°C. (a) Guinier radius, (b) Integrated intensity [96].

(1) Intermediate aging step at 100°C: the nucleation affected growth model (*i.e.* Eq. (5.26)) is applied to the intermediate aging stage, *i.e.* 5 hours at 100°C. At the start of aging at 100°C, the sample is in the naturally-aged state, therefore, the boundary conditions for this stage are defined as:

$f_{r(24h\,NA)} < f_r \le f_r(5h@100°C)$ and $r_{(24h\,NA)} < r \le r_{(5h@100°C)}$.

Solving Eq. (5.23) in the f_r and r ranges leads to:

$$r = r_{(5h@100°C)} \times \sqrt{\frac{f_r}{f_{r(5h@100°C)}}} \qquad (5.28)$$

in which, $r_{(5h@100°C)}$ =12.6 A° and $\frac{f_r}{f_r(5h@100°C)} \approx \frac{Qi}{Q(5h@100°C)}$ are obtained from the SAXS experiments presented in Figure 5.7 (a) and (b), respectively.

(2) Final artificial aging step at 150°C: the nucleation affected growth model (*i.e.* Eq. (5.26)) is applied to the final stage of aging. According to Figure 5.7 (b), the integrated intensity Q_i increases up to about 8 hours of aging at 150 °C and then becomes constant. Therefore, the peak aging time is estimated to be 8 hours, *i.e.* t_{peak}@ 150°C = 8 hours. Using Figure 5.7 (a), r_{peak} is approximated as the Guinier radius for the pre-aged sample aged for 8 hours at 150 °C, *i.e.* $r_{peak} = 26.7\text{A}°$.

The experimental values of f_r during aging at 150 °C are calculated through Eq. (5.27) using the data presented in Figure 5.7 (b). Additionally, the evolution of f_r during the final stage of aging (at 150°C) is modeled through Eq. (5.5). The constant parameters of the model are obtained from the IC analysis of the pre-aged materials at temperatures of 130, 150 and 177°C (see Table 5.9) [98]. The modeling and the experimental values of f_r are shown in Figure 5.8. The maximum error is calculated to be ~ 18%.

Table 5.9. The constant parameters reported for multi-step aging of AA7030 [98].

Parameter	**Value**
n	1.1
f_r^0	0.4
Q_v (kJ/mol)	59
k_{0v} (s^{-1})	2.3×10^3

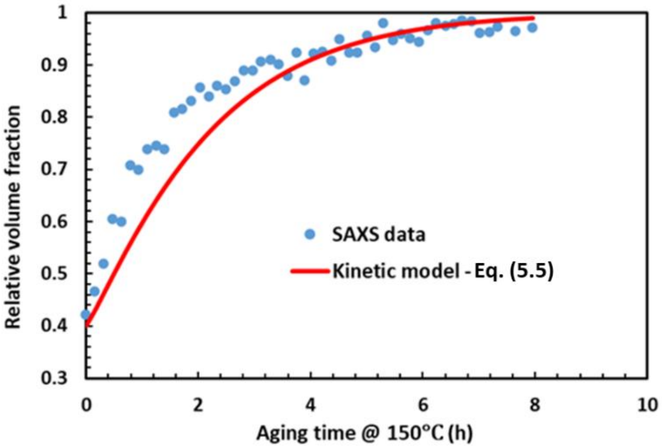

Figure 5.8. Comparison of the f_r values for AA7030 determined through experiments (SAXS), *i.e.* Eq. (5.27), and the kinetic model, *i.e.* Eq. (5.5).

Having obtained the predicted values of f_r during aging at 150°C (shown in Figure 5.8) and the r_{peak} value from Figure 5.7 (a), Eq. (5.26) is implemented using the following boundary conditions:

$f^o_{r(5h@100°C)} < f_r \leq 1$ and $r_{(5h@100°C)} < r \leq r_{peak}$

Finally, the measured values of precipitate radius (obtained from SAXS) along with the values predicted by the model (Eq. (5.26)) are plotted for both the pre-aging and final stage of aging in Figure 5.9.

The good agreement between the predicted and measured results suggests the validity of the nucleation-affected growth model (Eq. (5.26)) to estimate the precipitate size evolution during the intermediate and final aging stages of a multi-step aging process for AA7030.

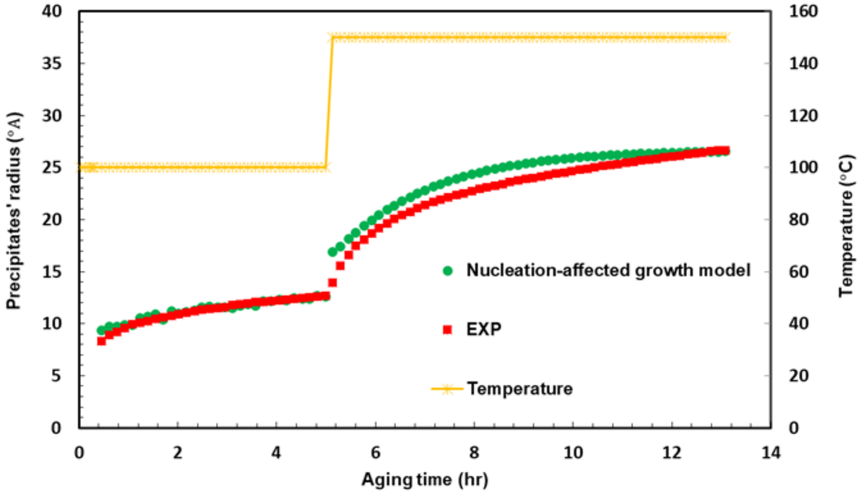

Figure 5.9. Comparison of the predicted and measured values of precipitate radius for AA7030 during pre-aging at 100°C followed by final aging at 150°C.

The maximum discrepancy between the predicted and measured values of precipitate radius is observed in the early stages of aging at 150°C. The possible explanation for such behaviour can be the initial dissolution of some pre-aging precipitates at the start of the final artificial aging step that is not considered in the nucleation-affected growth model.

ii. Aging route (B)

Aging route (B) consists of an additional intermediate aging step at 130°C after the pre-aging step and prior to the final aging at 170°C (see Table 5.8). The evolution of the Guinier radius r and the integrated intensity Q_i were recorded continuously through SAXS measurement from the start of pre-aging at 100°C, and up to two hours of aging at 170°C. The results are demonstrated in Figure 5.10 (a) and (b).

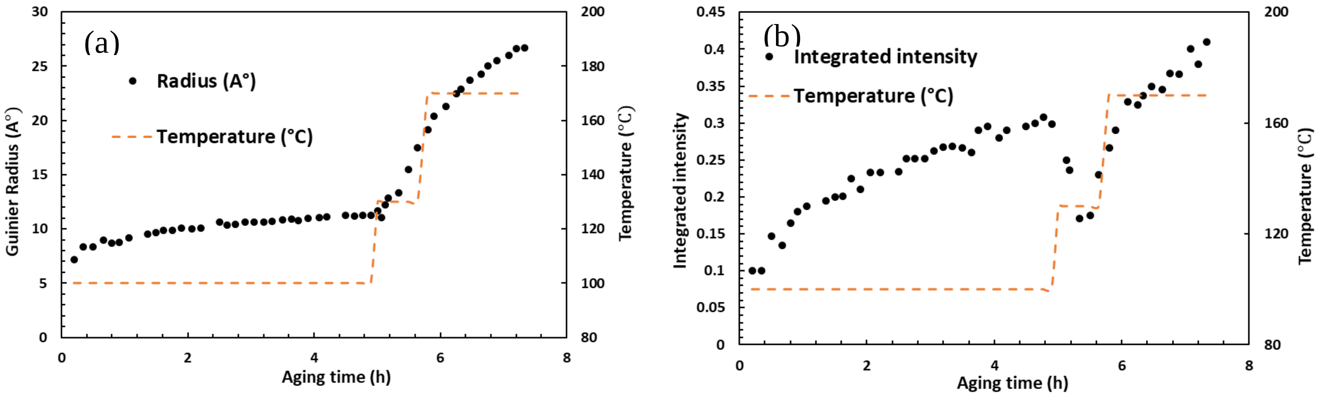

Figure 5.10. The results of the SAXS experiments conducted on AA7030 during pre-aging at 100°C followed by aging at 130°C and 170°C: (a) Guinier radius, (b) Integrated intensity [96].

The non-isothermal kinetic model, *i.e.* Eq. (5.1), is applied to model the evolution of f_r in the process of intermediate aging at 130°C, ramp heating to 170°C, and 2 hours of aging at the final aging temperature. The isothermal kinetic parameters shown in Table 5.9 are implemented in the kinetic model. Also, the experimental values of f_r during the sequential aging at 130 and 170°C are calculated through Eq. (5.27) using the data presented in Figure 5.10 (b).

The modeling and the experimental values of f_r during the non-isothermal aging process are shown in Figure 5.11. The drop in the integrated intensity curve at the start of aging at 170°C (see Figure 5.10 (b)) is considered to be due to the dissolution of some precipitates that are smaller than the critical size for precipitate stability. This effect is not currently considered in the non-isothermal kinetic model.

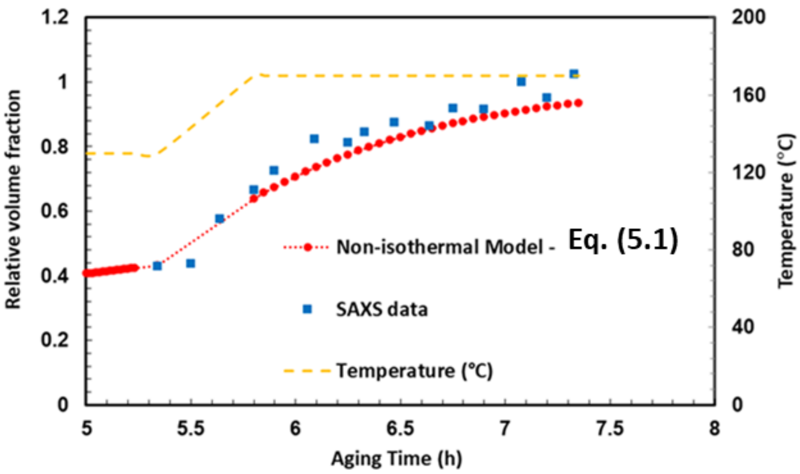

Figure 5.11. Comparison of experimental (SAXS) and modeling values of f_r during non-isothermal aging.

Having the predicted values of f_r, the evolution of precipitate radius can be modeled through Eq. (5.26) during the non-isothermal aging process:

(1) Intermediate aging step at 130°C: at the start of aging at 130°C, the material is naturally aged and pre-aged at 100°C. For this stage, the boundary conditions are defined as:

$f^{o}_{r(5h@100°\mathrm{C})} < f_r \leq f_r(15min@130°C)$ and $r_{(5h@100°\mathrm{C})} < r \leq r_{(15min@130°C)}$.

Solving Eq. (5.23) for the intermediate aging step in the defined boundary conditions leads to:

$$r = r_{(15min@130°C)} \times \sqrt{\frac{f_r}{f_r(15min@130°C)}} \qquad (5.29)$$

in which, $r_{(15h@130°C)}$ =13.3 A° is obtained according to the SAXS data presented in Figure 5.10 (a), and $\frac{f_r}{f_r(15min@130°C)}$ is determined using the modeling results presented in Figure 5.11.

(2) Final artificial aging step at 170°C: the nucleation affected growth model, *i.e.* Eq. (5.26), is applied in the defined boundary conditions:

$f^{o}_{r(15min@130°C)} < f_r \leq 1$ and $r_{(15min@130°C)} < r \leq r_{peak}$.

Using Figure 5.10 (a), r_{peak} is approximated as the Guinier radius for the sample aged for 2 hours at 170 °C, *i.e.* $r_{peak} = 26.7\text{A}°$. f_r values are also substituted from the modeling results presented in Figure 5.11.

Finally, the modeling results (obtained from the nucleation-affected growth model) along with the experimental values of precipitate radius (obtained from SAXS) during aging at 130 and 170 °C are compared in Figure 5.12.

The reasonable agreement between the modeling and the experimental results confirms the validity of the nucleation affected growth model (Eq. (5.26)) to predict the precipitate size evolution during the multi-step and non-isothermal aging process in AA7030 alloy.

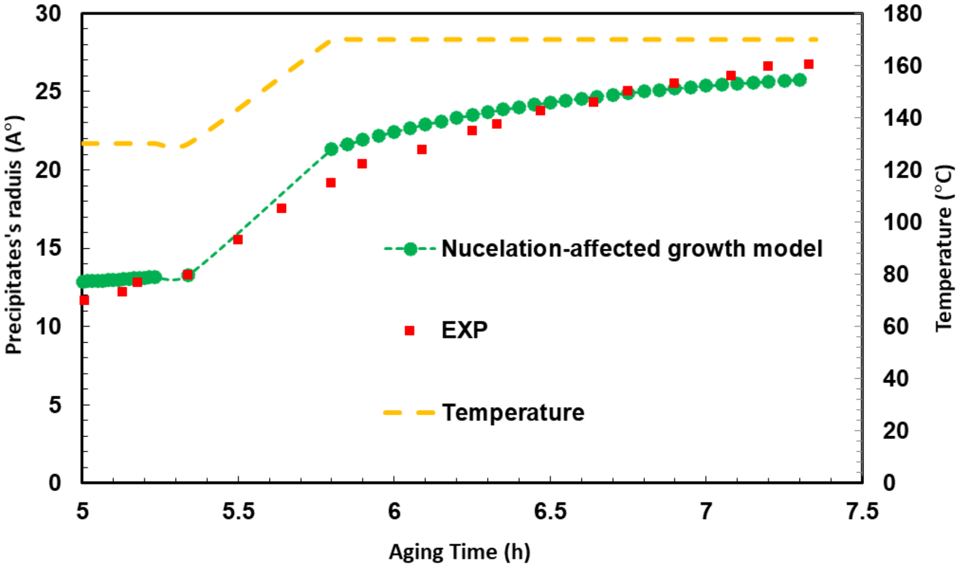

Figure 5.12. Comparison of the measured and predicted values of precipitate radius of AA7030 during aging at 130 and 170°C.

5.2.2.2. Weak obstacle strengthening equation

Having obtained the evolution of precipitate radius through Eq. (5.26), the weak obstacle model, *i.e.* Eq. (5.14), is modified as:

$$\sigma_{ppt|Weak} = C_2(r_{peak}\sqrt{f_r}f_r)^{1/2} \qquad (5.30)$$

To find C_2, it is assumed that at the peak aged condition $f_r = 1$ and $\boldsymbol{\sigma}_{ss} = 0$. So, the basic yield strength equation, Eq. (5.11) is given by:

$$\sigma_y^{peak} = \sigma_i + \sigma_{ppt}^{weak} = \sigma_i + \sigma_{ppt}^{strong} \tag{5.31}$$

where $\sigma_{ppt}^{weak} = C_2(r_{peak})^{1/2}$ and $\sigma_{ppt}^{strong} = C_1$ which leads to the following relationship between the constant parameters C_1 and C_2:

$$C_2 = \frac{C_1}{(r_{peak})^{1/2}} \tag{5.32}$$

By substituting C_2 from Eq. (5.32) into Eq. (5.30) the contribution of weak obstacles to the yield strength is expressed as:

$$\sigma_{ppt|Weak} = C_1(f_r)^{3/4} \tag{5.33}$$

The above modified weak obstacle model eliminates the need to have the precipitate radius r as a function of aging time. The validity of the modified weak obstacle model is examined in the next section.

Modified weak obstacle model validation

Earlier in this report, the precipitate size data obtained for an AA7010 alloy during aging at 160°C was used to validate the nucleation affected growth model (see section 5.2.2.1). In this section, the yield strength data reported for the same alloy and with the same heat treatment history (*i.e.*, solution heat treatment, 3 days natural aging and artificial aging at 160°C) [95] is utilized to validate the modified weak obstacle model, Eq. (5.33). The constant parameter C_1 (in Eq. (5.33)) is determined using the peak-hardness value that is reported by Deschamps *et al.* [95], for 3 hours of aging at 160°C and equals to 192HV (~576MPa). Also, since the as-quenched material yield strength was not reported in reference [95], the corresponding value for AA7050 in this current study (~ 135 MPa), is used in the solid solution strengthening equation (Eq. (5.12)). The calibration parameters for AA7010 for direct aging at 160°C are summarized in Table 5.10.

Table 5.10. Calibration parameters used for direct aging of AA7010 alloy at 160°C.

Parameter	**Value**
σ_{0ss} (MPa)	125
C_1(MPa)	526

Having the calibration parameters, the basic yield strength model, $i.e$. Eq. (5.11), is implemented and the contributions from solid solution strengthening and precipitation hardening (weak obstacles), are substituted from Eqs. (6.12) and (6.33), respectively. The f_r values that are implemented in the modeling equations are obtained through the SAXS experiments shown in Figure 5.5 (b) and through Eq. (5.27).

Figure 5.13 shows the results of the above modeling predictions in comparison with the experimental yield strength data reported in reference [95] ($i.e$. hardness data from reference [95] × 3). It is apparent that the evolution of yield strength during aging at 160 ℃ is well predicted by the modified weak obstacle model over the entire aging period.

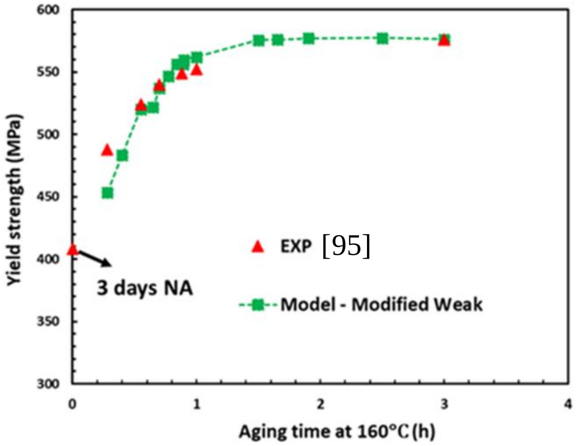

Figure 5.13. Comparison of modeling and experimental yield strength results of AA7010 alloy for artificial aging at 160°C after 3 days of natural aging.

5.2.3. Implementation of the yield strength model

5.2.3.1. Direct- natural aging

Natural aging kinetic parameters are not obtained through IC tests at room temperature due to the long duration of the process and the low heat evolved beyond the very early stages of natural aging ($i.e$. see Figure 3 in reference [58]). It is of interest to examine whether the kinetic parameters obtained for high temperature IC tests are useful in obtaining a good estimation of f_r evolution with natural aging time at room temperature. The approach in this section is to consider natural aging as a direct aging process at room temperature. Accordingly, the evolution of f_r during natural aging is determined through Eq. (5.3). The kinetic parameters (k_{0v} and Q_v) obtained from the high temperature IC experiments on the as-quenched material (see Table 5.2), are substituted in the Arrhenius relationship, Eq. (5.2), to obtain the value of k_v for natural aging. Considering the dominance of GP zone formation during natural aging, it is reasonable to assume that $n \neq 1$. Indeed, the time exponent n in Eq. (5.3) is assumed to be ~ 0.3 as reported by Abolhasani [84], who has reverse calculated the kinetic parameters of natural aging for AA7075.

The predicted values of f_r are used to predict the yield strength according to the following assumptions: (a) precipitate size r is constant, *i.e.* Eq. (6.13), and (b) r increases with time, *i.e.* Eq. (5.33).

The calibration parameter C_1 is found by using the σ_y value obtained experimentally for the one-year natural aging:

$\sigma_y\,(peak) = 480$ MPa, therefore: $\sigma_{ppt}^{NA} = 480 - \sigma_i = 470$ MPa and $C_1 = 470$ MPa.

σ_{0ss} is related to the yield strength of the as-quenched material:

$\sigma_y(as - quenched) = 135$ MPa, therefore: $\sigma_{ss} = 135 - \sigma_i = 125$ MPa and $\sigma_{0ss} = 125$ MPa.

These parameters, as well as the kinetic parameter k_v obtained from the IC tests at temperatures in the range of 135-190°C, are reported in Table 5.11.

Table 5.11. The calibration parameters of AA7050 alloy obtained up to one-year natural aging.

Calibration Parameter	**Value**
σ_{0ss}	125 MPa
C_1	470 MPa
n	0.3 [84]
k_v (Arrhenius relationship Eq. (5.2))	$1.6 \times 10^6\ s^{-1}$ (k_{0v} and Q_v from Table 5.2)

The predicted values of yield strength, along with the experimental data, are plotted in Figure 5.14. As expected, this method gives a rough estimation of the yield strength values because of the use of high temperature IC results. The observations indicate that the differences between the measured values of yield strength and the predictions are very similar for both cases of constant precipitate radius and growing precipitate radius (average difference in both cases is ~ 6%).

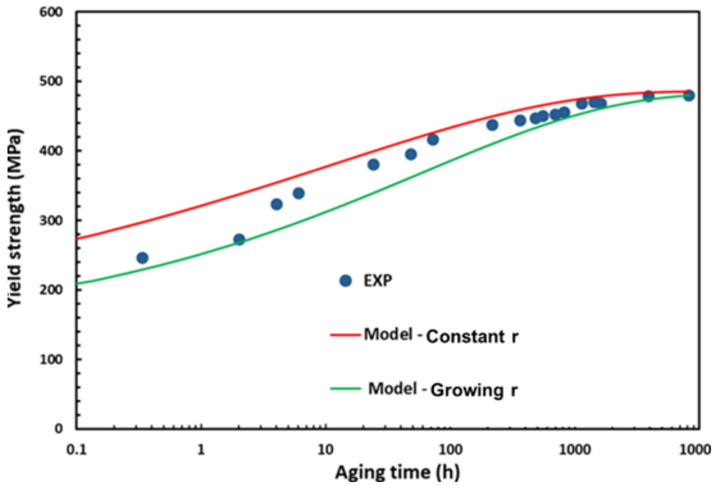

Figure 5.14. Comparison of the experimental data and modeling results for the yield strength of AA7050 up to one year of natural aging using the k_{0v} and Q_v values from the high temperature IC analysis.

5.2.3.2. Direct- artificial aging

To model the evolution of yield strength during direct-aging of the current AA7050 alloy, the basic yield strength model, *i.e.* Eq. (5.11), is implemented. The contributions from solid solution strengthening and precipitation hardening, through strong and weak obstacles, are substituted from Eqs. (5.12), (5.13) and (5.33), respectively. As was shown in Section 5.1.2, the values of f_r were predicted using the determined kinetic parameters for direct aging (see Figure 5.2 and Table 5.2). By using the hardness values of the as-quenched and the peak-aged samples after direct aging at two different temperatures of 150 and 177 °C, the calibration parameters (σ_{0ss} and C_1) are determined for each aging temperature and are listed in Table 5.12.

Table 5.12. The calibration parameters for direct aging of AA7050.

Parameter	**Value for each aging Temperature**	
	150 °C	**177 °C**
σ_{0ss}(MPa)	125	125
C_1(MPa)	533	500

The modeling results together with the measured values of yield strength ($\sim H_v \times 3$) for direct-aging at two temperatures of 150 and 177°C are demonstrated in Figure 5.15 (a) and (b), respectively. It can be observed that for the case of aging at 150 °C, the modified weak obstacle equation (Eq. (5.33)) has a better agreement with the experimental results compared to the strong obstacle equation. While for the case of aging at higher temperature of 177°C, the material strength is better approximated by the strong obstacle model. This result suggests that for the case of aging at higher temperature of 177°C, since precipitates are larger, the strong obstacle model works better.

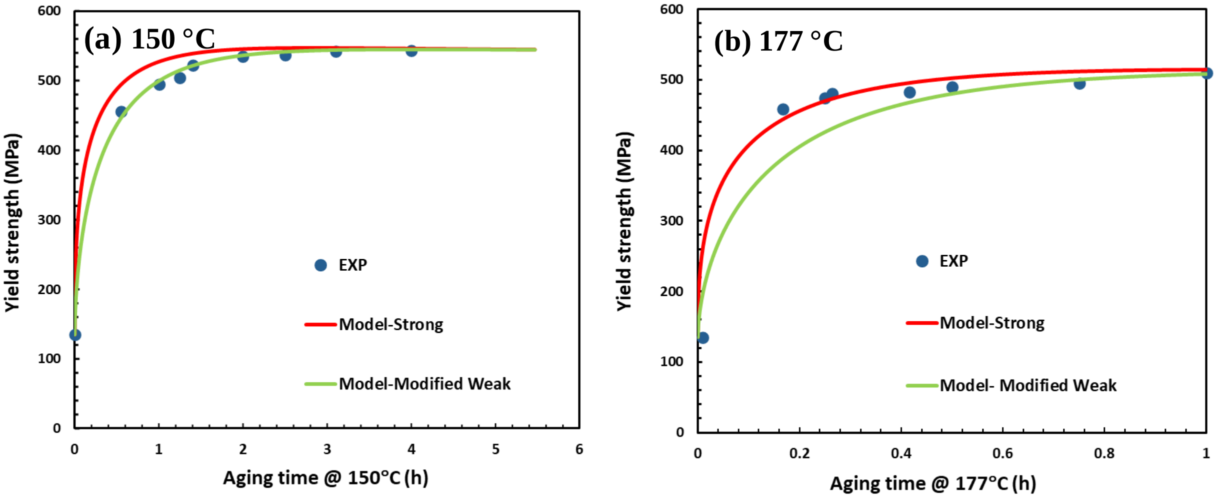

Figure 5.15. Comparison of the measured and predicted values of the yield strength of AA7050 alloy during aging at (a) 150 and (b) 177°C.

5.2.3.3. Multi-step aging

In this section, the evolution of yield strength during the final step of a multi-step aging process is modeled through Eq. (5.11). As was shown in Section 5.1.3, the f_r values were determined through Eq. (5.5) using the calculated kinetic parameters for multi-step aging (see Figure 5.4 and Table 5.5). The predicted values of f_r are now substituted in Eqs. (5.12), (5.13) and (5.33). The calibration parameter C_1 is calculated by using the peak hardness value obtained from the final aging step of the multi-step heat treatment. The value of σ_{0ss} remains the same as in the direct aging process.

Table 5.13 summarizes the calibration parameters determined for the pre-aged AA7050 alloy for final step of aging at the two temperatures of 150 and 177°C.

Table 5.13. The calibration parameters for final stage of aging of the pre-aged AA7050 alloy.

Parameter	**Value for each aging Temperature**	
	150℃	**177 ℃**
$\sigma_{0ss}(MPa)$	*125*	*125*
$C_1(MPa)$	*554*	*551*

The results of the yield strength model prediction for the final step of aging at 150 and 177°C, implementing both strong (Eq. (5.13)) and modified weak obstacle (5.33) models, are shown in Figure 5.16 (a) and (b), respectively. It can be observed that for the case of aging at 150 ℃, the average error is very similar for both cases of strong and weak obstacle models (~ 4.5%). This observation can be due to the reason that at the start of final artificial aging step, f_r^0 value is already high (~0.52) and the variation in f_r would be limited. Since the basis of the difference between the strong and weak obstacle models are the values of ${f_r}^{1/2}$ and ${f_r}^{3/4}$, respectively, a large difference between the two models is not expected. On the other hand, for the case of aging at 177°C, the experimental values of yield strength are better approximated by the strong model. This result can be due to the reason that during aging at higher temperature of 177℃, since the precipitates are larger, the strong obstacle model works better.

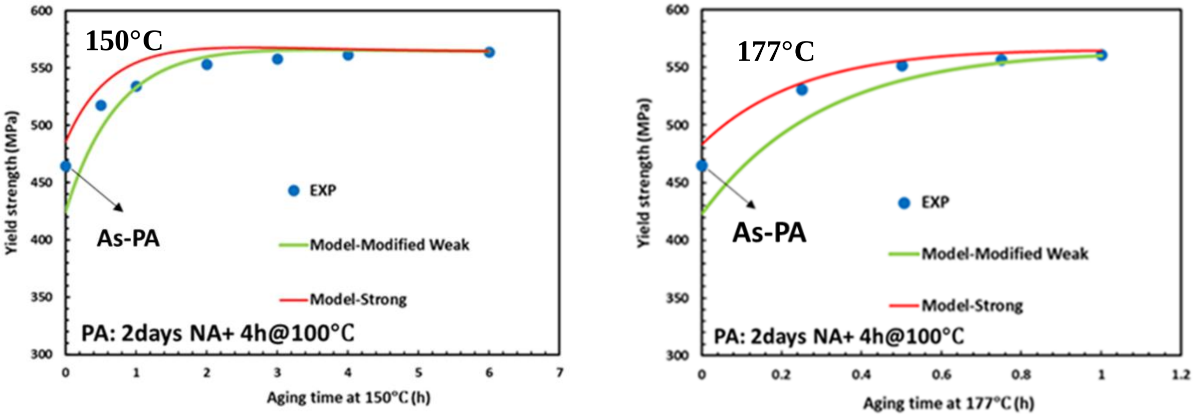

Figure 5.16. Comparison of the measured and predicted values of the yield strength of the pre-aged (pre-aging process: 2 day natural aging+ 4 hours of aging at 100°C) AA7050 during final artificial aging at (a) 150 and (b) 177℃.

5.3. Deformation-affected precipitation kinetics

The focus of this section is to present the results of the investigation on the effects of deformation, through warm-forming (WF), on the precipitation kinetics of AA7075 during multi-step aging. The heating profile of the warm forming process was presented in Chapter 3, Figure 3.2. Similar to the analysis for the non-deformed AA7050 material (Section 5.1), the precipitation kinetics of the PA+WF AA7075 during final stage of artificial aging is first examined through IC analysis. Then, a theoretical kinetic model is introduced which takes in to account the presence of dislocations during aging. The theoretical model eliminates the necessity of performing IC tests on the PA+WF materials.

5.3.1. Kinetics of precipitation through IC analysis

To analyze the precipitation kinetics of the PA+WF AA7075 material (during the final artificial aging step) through the IC tests, it is assumed that the precipitate content of the artificially aged material is solely dependent on the artificial aging temperature (*i.e.* the metastable phase diagram) [2]. Hence, the relative volume fraction of precipitates during aging, f_r, is expressed using the original IC analysis [2] and is similar to the analysis presented in Section 5.1.3:

$$f_r = f^0_{r(PA+WF)} + \frac{f_{V|AA}}{f_{V|peak}} \tag{5.34}$$

in which, $f_r = \frac{f_V}{f_{V|peak}}$ and $f^0_{r(PA+WF)}$, which is the relative volume fraction of precipitates at the start of the final artificial aging process, is defined as: $f^0_r = \frac{f_{V|PA+WF}}{f_{V|peak}}$.

The value of $\frac{f_{V|AA}}{f_{V|peak}}$ is calculated through the IC data of both the PA+WF and as-quenched AA7075 material conditions [2]:

$$\frac{f_{v|AA}}{f_{V|peak}} = \frac{\int_0^t \frac{dQ}{dt} dt|_{(PA+WF)+AA}}{\int_0^{t_f} \frac{dQ}{dt} dt|_{AQ+AA}} \tag{5.35}$$

in which, $\int_0^t \frac{dQ}{dt}\, dt|_{(PA+WF)+AA}$ is the area under the IC trace up to time t for the PA+WF material and $\int_0^{t_f} \frac{dQ}{dt}\, dt|_{AQ+AA}$ is the area under the IC trace up to the peak aged condition, *i.e.* t_f, for the as-quenched material.

The value of $f^0_{r(PA+WF)}$ for each testing temperature is determined from Eqs. (5.34) and (5.35) for $t = t_f$ and $f_r = 1$[2]:

$$f^0_{r(PA+WF)} = \frac{\int_0^{t_f} \frac{dQ}{dt} dt|_{AQ+AA} - \int_0^{t_f} \frac{dQ}{dt} dt|_{(PA+\mathrm{WF})+AA}}{\int_0^{t_f} \frac{dQ}{dt} dt|_{AQ+AA}} \tag{5.36}$$

Table 5.14 represents the calculated values of $f^0_{r(PA)}$ and $f^0_{r(PA+WF)}$ for the PA and PA+WF AA7075 material through Eqs. (5.8) and (5.36), respectively.

Table 5.14. The f^0_r values calculated for final stage of aging of the PA and PA+WF AA7075 material.

Temperature(°C)	$f^0_{r(PA)}$	$f^0_{r(PA+WF)}$
150	0.44	0.4
165	0.47	0.41
177	0.44	0.36
Average	**0.45**	**0.4**

Using the data presented in Table 5.14, the experimental values of f_r for artificial aging of the PA and PA+WF AA7075 samples are determined through Eqs. (5.6) and (5.34), respectively. The results for the case of aging at 177°C are plotted in Figure 5.17. It can be understood from the figure as well as the data presented in Table 5.14, that the volume fraction of precipitates at the initial stages of aging for the PA+WF condition is less than that for the PA material (the difference is ~ 20%). As was discussed in Section 4.2.1 (the hardness comparison), this initial lower volume fraction of precipitates for the PA+WF material compared to the PA material, confirms the potential dissolution of some pre-aging GP zones during the warm forming procedure [55], [15], [20]. As a result of this dissolution effect, the initial volume fraction of GP zones that could have assisted the formation of η' during aging at 177°C, is reduced for the PA+WF material. Also, some of the solutes go back into solution. However, as shown in Figure 5.17, the volume fraction of precipitates in the PA+WF material reaches similar values to that of the PA material within a very short time, *i.e.* ~ 2 minutes. Indeed, the increased driving force for precipitation (due to the solute enrichment of the matrix after GP zones dissolution), as well as the presence of dislocations as heterogeneous nucleation sites [14], [15], [55], [88], may have assisted the PA+WF material achieve similar volume fraction of precipitates/precipitation rate as the PA material (within ~2 minutes) during aging at 177°C. As was mentioned in Section 4.2.1 (the hardness comparison), the comparison of the f_r values (Figure 5.17), shows the improvement of the precipitation hardening contribution in the PA+WF material due to the presence of dislocations.

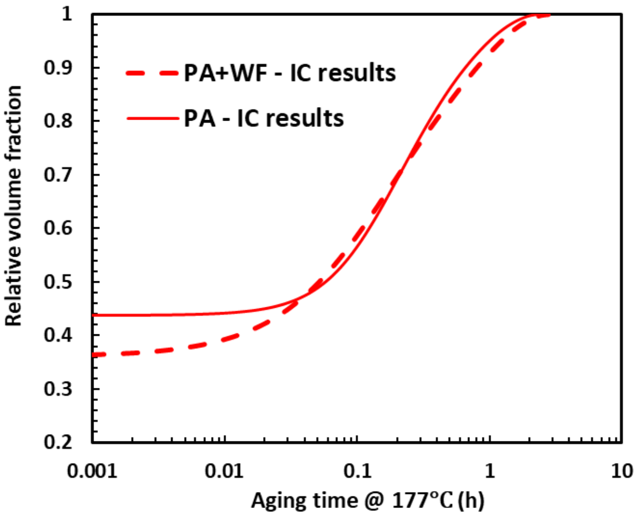

Figure 5.17. Comparison of the experimental values of the relative volume fraction of precipitates for the PA and PA+WF material during aging at 177°C.

The evolution of f_r as a function of time at the final artificial aging temperature for the PA+WF material, is modeled using the adjusted form of Eq. (5.5) as follows:

$$f_r = 1 - (1 - f^0_{r(PA+WF)}) exp\,(-k_{eff} t)^n \qquad (5.37)$$

in which, k_{eff} is the precipitate rate constant in the presence of dislocations.

In the current condition for which the pre-aged material is warm-formed prior to the final artificial aging step, it is assumed that the dominant effect of the deformation on the precipitation kinetics, *i.e.* k_v, is the enhancement in solute diffusivity through the effect of dislocation core diffusion [99]. Thereby, the contribution of pipe diffusion (dislocation core) to the precipitation kinetics should be considered along with the bulk (volume) diffusion. Accordingly, the temperature-dependent precipitation rate parameter, k_v, is defined as an effective rate as follows:

$$k_{eff} = k_{0eff} \times \exp(-Q_{eff}/RT) \qquad (5.38)$$

in which, k_{0eff} and Q_{eff} are the pre-exponential factor and the apparent activation energy values, respectively, that encompass both bulk diffusion and dislocation core diffusion effects.

To find the values for n and k_{eff}, Eq. (5.37) is fitted to the experimental values of f_r (obtained through Eq. (5.34)) and is transformed to the following form:

$$lnln\frac{\left(1-f^0_{r(PA+WF)}\right)}{1-f_r} = nlnt + nlnk_{eff} \qquad (5.39)$$

By plotting the data from implementing Eq. (5.39) in the range of $f^0_{r(PA+WF)}$ and 95% and fitting a straight line to the resulting curve, the values of n and k_{eff} are determined (Table 5.15).

Table 5.15. Kinetic parameters n and k_{eff} obtained for artificial aging of the PA+WF alloy.

Temperature (℃)	n	k_{eff} (s^{-1})
150	1	0.0004
165	0.9	0.0007
177	0.8	0.0010

It is worth noting that in both cases of PA and PA+WF materials, the n value is found to be close to unity. This result suggests that η' precipitates are the dominant precipitates in the matrix during the final stage of aging.

The determined values of k_{eff} are then used to obtain the effective kinetic parameters, k_{0eff} and Q_{eff}, for the final aging of the PA+WF material through the Arrhenius relationship in Eq. (5.38). For the purpose of comparison, the kinetic parameters of the PA-AA7075 material (k_{0v} and Q_v) are also found through the analysis of Section 5.1.3. Figure 5.18 shows the Arrhenius plots for the PA and PA+WF materials, and the obtained kinetic parameters are summarized in Table 5.16.

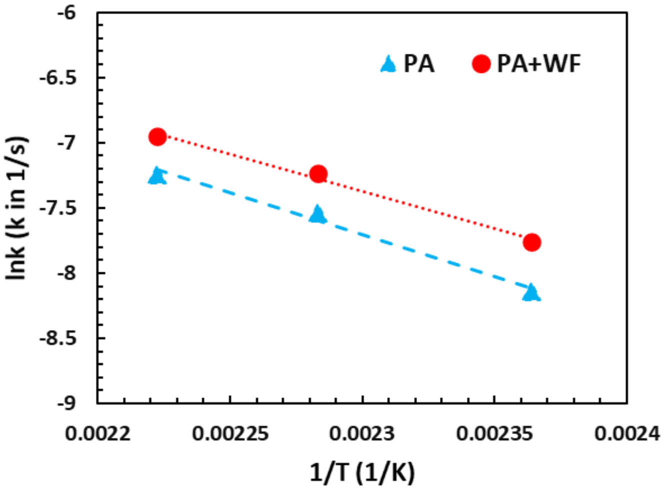

Figure 5.18. The Arrhenius plot to determine the kinetic parameters for the PA and PA+WF AA7075 for final artificial aging at 177°C.

Table 5.16. Kinetic parameters determined from IC tests for final aging stage of the PA and PA+WF AA7075 alloys.

PA		**PA+WF**	
k_{0v} (1/s)	$Q_v\ (\frac{kJ}{mol})$	k_{0eff}(1/s)	$Q_{eff}\ (\frac{kJ}{mol})$
1.1×10^3	53	3.4×10^2	48

Comparison of the kinetic parameters of PA and PA+WF materials suggests that the presence of dislocations does not significantly alter the precipitation kinetics in the current condition. Since the values of activation energy, Q_{eff}, and the pre-exponential factor, k_{0eff}, in the PA+WF material conditions are both lower than the respective values in the PA (non-deformed) material (Q_v and k_v), they balance each other's effect and the kinetics remain unchanged. The similar precipitation kinetics is specifically observed for the current heat treatment and processing condition of the selected material. However, the effect of dislocation core diffusion on the precipitation kinetics is an important factor that should be considered in general experimental and modeling analysis.

Finally, the kinetic parameters obtained for the PA+WF material (see Table 5.16) are used to model the evolution of f_r through Eq. (5.37). The modeling results for final artificial aging at three temperatures of 150, 165 and 177°C are compared with their respective experimental IC data in Figure 5.19. It is evident that the results from the model and the experimental analysis agree well.

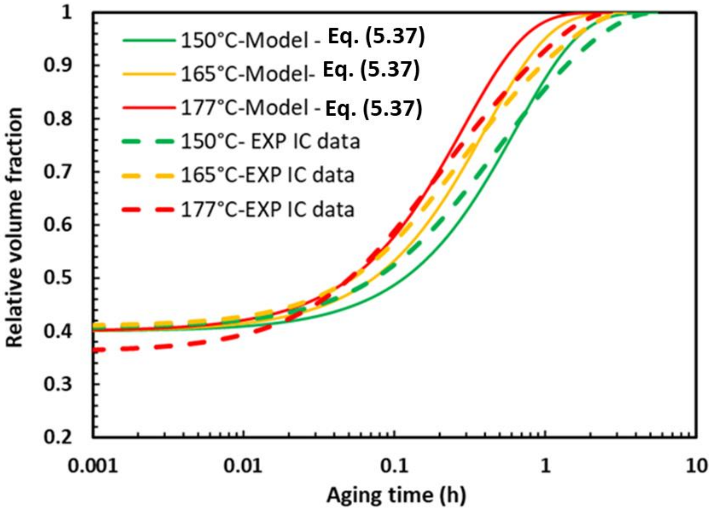

Figure 5.19. Comparison of modeling and experimental results of the relative volume fraction of precipitates for final artificial aging of the PA+WF-AA7075.

5.3.2. Development of the kinetic model – theoretical

In the previous section, the kinetics of precipitation for the final artificial aging stage of the PA+WF material was investigated by performing IC tests and the kinetic parameters k_{0eff} and Q_{eff} were determined through the experimental analysis. However, this approach is limited to the cases in which, the time and equipment for the experimental analysis are available. In this section, kinetic model formulations are developed through the theoretical descriptions of the effect of dislocation core diffusion on the precipitation kinetics.

To model the evolution of f_r for the multi-step and non-isothermal heat treatment processes consisting of an intermediate warm-forming stage, *e.g.* the current sequential warm-forming and artificial aging processes, first the following assumptions are made:

(A) Since the temperatures of the warm-forming and the subsequent artificial aging are very close (in the range of 150-177°C), it is assumed that the dislocation density remains unchanged, *i.e.* dislocation recovery is ignored:

ρ (during warm forming) = ρ (during subsequent artificial aging).

(B) The time exponent (n) in the f_r equation is considered equal to unity (n = 1) which is of characteristics of η' precipitates [60].

(C) Possible dissolution of pre-aging precipitates during the warm forming stage is not considered in the model.

Then, the heat treatment and forming process that are applied to the PA material are divided into two non-isothermal heat treatment steps (see Figure 3.2):

(i) Before the deformation: ramp heating of the PA material from RT to the warm-forming temperature, *i.e.* 150℃ (17 K/s).

(ii) Deformation and post-deformation treatment: warm-forming at 150°C + air cooling + final aging at 177°C.

Next step is to write the general kinetic model, *i.e.* the non isothermal f_r model (Eq. (5.1), for each of the above mentioned heat-treatment steps:

- Variations of f_r during the ramp heating, step (i), is given as:

$$f_r(i) = 1 - \left(1 - f^0_{r(PA)}\right) exp[-\textstyle\sum_i (k_{iv})^n \, (t_i^n - t_{i-1}^n)] \qquad (5.40)$$

in which, $f^0_{r(PA)}$ is the relative volume fraction of precipitates at the start of ramp heating or at the end of the pre-aging stage. The values of $f^0_{r(PA)}$ were determined through Eq. (5.8) and were presented in Table 5.14. k_{iv} is the temperature dependent constant describing the reaction rate in the absence of dislocations (related to bulk diffusion) and the time exponent n is considered equal to unity.

- Once the deformation is started at the warm-forming stage, the variations of f_r for the warm-forming process and the post-deformation treatment (warm-forming + air cooling + aging at 177°C), step (ii), is written as:

$$f_r(ii) = 1 - \left(1 - f^0_{r(PA+Ramp)}\right) exp\left[-\textstyle\sum_i (k_{ieff})^n \, (t_i^n - t_{i-1}^n)\right] \qquad (5.41)$$

in which, $f^0_{r(PA+Ramp)}$ is the relative volume fraction of precipitates at the start of warm-forming. k_{ieff} is the temperature dependent constant describing the reaction rate in the presence of dislocations and the time exponent n is considered equal to unity.

It is worth noting that the value of $f^{0}_{r(PA+Ramp)}$ in Eq. (5.41) is indeed equal to the relative volume fraction of precipitates at the end of the ramp heating from RT to the WF temperature, *i.e.* $f_r(i) = f^{0}_{r(PA+Ramp)}$. Therefore, by substituting Eq. (5.40) into Eq. (5.41), the variations of f_r over the entire heat treatment (starting from the PA condition), is described as:

$$f_r(tot) = 1 - \left(1 - f^{0}_{r(PA)}\right) exp\left[-\sum_i (t_i^n - t_{i-1}^n)((k_{iv})^n + (k_{ieff})^n)\right] \qquad (5.42)$$

As can be seen in the above equation, the summation section has two components, k_{iv} and k_{ieff}. k_{iv} denotes the rate constant of the reaction prior to the warm forming stage and corresponds to the non-deformed condition. Once the deformation is started, the rate constant should change to the effective value (k_{eff}) to account for the effect of dislocation core diffusion on the precipitation kinetics. Eq. (5.42) is a general model that can be implemented for the multi-step heat treatments, either with or with out the deformation stage. As in the cases without a deformation stage, the value of k_{eff} is dismissed and the equation will be reduced to the Esmaeili and Lloyd's model, *i.e.* Eq. (5.1).

5.3.3. Implementation of the kinetic model

To be able to implement the non-isothermal f_r model, Eq. (5.42), to the sequential warm-forming and aging processes, *e.g.* the current heat treatment process (Figure 3.2), the value of k_{eff} is required. A modeling equation is introduced in the next section which predicts k_{eff} values for each aging temperature. Consequently, the kinetic parameters of k_{0eff} and Q_{eff} are determined through Eq. (5.38) and the necessity of performing the calorimetry tests on the PA+WF materials is eliminated.

In addition, the value of dislocation density generated during the warm-forming process is obtained (through two approaches). This value will then be implemented in the k_{eff} model.

5.3.3.1. Modeling of k_{eff}

The focus of this section is on the effect of deformation on enhancing the diffusional mechanisms upon aging, and its effect on the precipitate nucleation which is not considered in the current modeling equations. To this end, the resultant effective diffusion coefficient that captures the combined effects of bulk (lattice) and dislocation core diffusions on the precipitation kinetics is defined as:

$$D_{eff} = f_v D_v + f_c D_c \qquad (5.43)$$

Eq. (5.43) was originally proposed by Hart [100], in which D_{eff} is the effective diffusion coefficient in presence of dislocations, D_v is the diffusion coefficient of the lattice (volume), D_c is the diffusion coefficient of the dislocation core, and f_v and f_c are the contributions from the lattice and the core, respectively. Eq. (5.43) was later modified by Frost and Ashby [101]:

$$D_{eff} = D_v\left(1 + \frac{\rho a_c D_c}{D_v}\right) \qquad (5.44)$$

in which, ρ is the dislocation density and a_c is the cross-sectional area of the dislocation core. The diffusion coefficients of the lattice and core are given as:

$$D_v = D_{0v}\, exp\left(\frac{-Q_v^{diff}}{RT}\right) \qquad (5.45)$$

$$D_c = D_{0c}\, exp\,(\frac{-Q_c^{diff}}{RT}) \qquad (5.46)$$

in which, D_{0v}, Q_v^{diff}, D_{0c}, and Q_c^{diff} are the pre-exponential factors and the activation energies for lattice and core diffusion, respectively. Since both the diffusivity, *D*, and the rate constant, *k*, have an Arrhenius relationship with respect to the temperature, it is reasonable to assume that:

$$\frac{D_{eff}}{D_v} \approx \frac{k_{eff}}{k_v} \qquad (5.47)$$

Equating Eqs. (5.44) and (5.47) leads to:

$$k_{eff} = k_v\left(1 + \frac{\rho a_c D_c}{D_v}\right) \qquad (5.48)$$

The diffusion coefficients of the lattice and core, D_v and D_c are substituted from Eqs. (5.45) and (5.46), respectively, and Eq. (5.48) is expanded to the following form:

$$k_{eff} = k_v\left(1 + \rho a_c \frac{D_{0c}}{D_{0v}} exp\,(\frac{Q_v^{diff} - Q_c^{diff}}{RT})\right) \qquad (5.49)$$

There is a considerable amount of literature reporting the values of D_{0c}, D_{0v}, Q_c and Q_v for aluminum alloys [24], [51], [93], [99], [102]–[105]. However, these values are dependent on the composition and structure of the material. Due to the similarities between the chemical composition of the current AA7075 and AA7475 taken from the literature [106](see Table 5.17), the above parameters are assumed to be very close to the reported values for the AA7475 alloy [106]. These values are listed in Table 5.18.

Table 5.17. The chemical composition of the current AA7075 and AA7475 reported in [106](wt%).

	Mn	Si	Cr	Mg	Ti	Cu	Zn	Fe	Zr
AA7475 [106]	< 0.08	0.2-0.3	0	2-2.5	0	1.5-2.5	5.5-6.5	< 0.2	0.2-0.3
AA7075	0.04	0.08	0.19	2.27	0.03	1.38	5.63	0.15	0.01

Table 5.18. Constant parameters of the k_{eff} model (Eq. (5.49)) taken from reference [106].

Variable	**Value in the model**
$a_c \frac{D_{0c}}{D_{0v}}$	4.7×10^{-19}
Q_v^{diff}	$120 \frac{kJ}{mol}$
Q_c^{diff}	$80 \frac{kJ}{mol}$

The final modeling equation describing the k_{eff} value for the deformed AA7075 as a function of dislocation density and the k_v value (which is associated with the non-deformed condition) is written as:

$$k_{eff}(Model) = k_v(1+\rho \times 4.7 \times 10^{-19} \times exp(\frac{40}{RT})) \qquad (5.50)$$

For the current work, the k_v parameter in the above equation is determined by performing IC tests on the PA materials (the results were shown in Table 5.16).

To be able to predict the k_{eff} value using equation (Eq. (5.50)), knowledge of the dislocation density, ρ, is required. To determine the dislocation density, two approaches are pursued:

(i) Utilizing the modeling approaches to find a simple equation that predicts the dislocation density as a function of applied plastic strain. This method has a general function and broadly applicable (including the current work).

(ii) Experimental determination of dislocation density through performing IC tests on the PA+WF materials (exclusively for the current work).

Each approach is explained separately in the following sections after which, the results will be compared to each other.

5.3.3.2. Dislocation density ($\boldsymbol{\rho}$) calculation

<u>First approach: Modeling methods</u>

Following Ashby [107], it is assumed that the total dislocation density in a deformed material is equal to the sum of statically stored and geometrically necessary dislocations. In the process of deforming a two-phase (or more) alloy system, one component may deform plastically more than the other, leading to a gradient of deformation in the material. The gradient of deformation requires some dislocations to be stored to acquire compatible deformation of various parts of the specimen (to maintain material's integrity). These dislocations are conveniently called "geometrically necessary" dislocations. Also, some dislocations may accumulate by trapping each other in a random way that are called "statically stored" dislocations [107]. Reportedly, the statically stored dislocation density, is a characteristic of the material (*i.e.* crystal structure, shear modulus, stacking-fault energy, *etc*), and the geometrically necessary dislocation density, is a characteristic of the microstructure (*i.e.* the geometric arrangements, size of grains and phases and independent of the material) [107].

Following Ashby's theory regarding the two types of dislocations, a model describing the evolution of total dislocation density ρ with plastic strain is given as a generalization of Kocks/Mecking [5], [27] approach:

$$\frac{\partial \rho}{\partial \epsilon} = (k_1 \rho^{1/2} - f k_2 \rho^{1/2} + k_D) \qquad (5.51)$$

in which, ϵ is the applied plastic strain, k_1, k_2, f, and k_D are constants. The term $k_1 \rho^{1/2}$is related to the dislocation storage rate due to trapping of dislocations by one another (*i.e.* related to the statically stored dislocation density), the term $f k_2 \rho^{1/2}$ is related to the dynamic recovery, which is dependent on temperature, strain rate, and solute concentration. The last parameter, k_D is related to the storage of geometrically necessary dislocations due to the non-shearable precipitates [5].

There is general agreement that the deformation behaviour of the precipitate-containing alloys can be significantly affected by the nature of the dominant precipitates, whether they are shearable or non-shearable [5]. According to the studies conducted by Cheng *et al.* [5] and Myhr *et al.* [108], when the particles are shearable, the storage of geometry necessary dislocations can be ignored and the term k_D in Eq. (5.51) is equal to zero ($k_D \approx 0$). Therefore, assuming that the majority of precipitates are shearable in the under aged regime, Eq. (5.51) is re-written as:

$$\frac{\partial \rho}{\partial \epsilon} = (k_1 \rho^{1/2} - f k_2 \rho^{1/2}) \qquad (5.52)$$

To further simplify the above equation, it can be assumed that the dynamic recovery during the current warm-forming condition (*i.e.* fast forming at 150℃) and the subsequent artificial aging (at 177 ℃) is not very different from that at RT. Hence, the value of $f k_2$ is considered to be constant and equal to the value reported by Cheng *et al.* [5] for AA6111 alloy for the room temperature recovery, *i.e.* $f k_2 \approx 27$. The simplified version of Eq. (5.52) is written as:

$$\frac{\partial \rho}{\partial \epsilon} = (k_1 \rho^{1/2} - 27 \rho^{1/2}) \qquad (5.53)$$

Integrating Eq. (5.53) gives:

$$\int_{\rho_0}^{\rho} d\rho \, \frac{\rho^{-1/2}}{(k_1 - 27)} = \int_{\epsilon_0}^{\epsilon} d\epsilon \qquad (5.54)$$

Then, solving Eq. (5.54) results in the evolution of dislocation density ρ as a function of plastic strain ϵ:

$$\frac{2}{(k_1 - 27)} \times (\sqrt{\rho} - \sqrt{\rho_0}) = \epsilon - \epsilon_0 \qquad (5.55)$$

Eq. (5.55) should be calibrated by finding the constant value of k_1, which is reported to be a characteristic of the material under the investigation [5], [108]. It is reported by Robson [99] that the dislocation density in the undeformed aluminum ($\epsilon_0 = 0$) is approximately $1 \times 10^{11} m^{-2}$. In another investigation conducted by Deschamps *et al.* [15] on an AA7449 alloy (which is similar to AA7075), it was assumed that 6% deformation at a temperature in the range of 120-160℃ results in a dislocation density equal to $2 \times 10^{12} m^{-2}$. Table 5.19 summarizes the above-mentioned parameters and values that are used to calibrate Eq. (5.55).

Table 5.19. The calibration parameters used in Eq. (5.53).

Parameter	ϵ_0	$\rho_0\ (m^{-2})$
Value	0	1×10^{11} [99]
Parameter	ϵ	$\rho\ (m^{-2})$
Value	0.06	2×10^{12} [15]

By substituting the parameters presented in Table 5.19 in Eq. (5.55), the constant value of k_1 for the warm deformation of 7000-series aluminum alloys is estimated as: $k_1 = 3.7 \times 10^7 m^{-1}$. Hence, the final model describing the dislocation density as a function of strain level is found as:

$$\rho_{model} = (3.16 \times 10^5 + 1.8 \times 10^7 \boldsymbol{\epsilon})^2 \qquad (5.56)$$

Based on Eq. (5.56), the evolution of the dislocation density with respect to the plastic strain for the strain levels in the range of 0-100% is plotted in Figure 5.20.

Second approach: Experimental methods

In this section, the dislocation density that is produced during the current warm-forming experiment (*i.e.* 10% tensile deformation at 150°C) is determined by calibrating the k_{eff} model, Eq. (5.50), using the IC test results. Consequently, the values of k_{eff} and k_v obtained from the experimental analysis of the IC test results of the PA and PA+WF material (see

Table 5.16), were substituted in Eq. (5.50). It is assumed that the dislocation density during warm-forming and the subsequent artificial aging has a relatively constant value. Therefore, the value of dislocation density is calculated as:

$$\boldsymbol{\rho_{exp}} = \left[\left(\frac{k_{eff}}{k_v}\right) - 1\right] / \left[\, 4.7 \times 10^{-19} \times exp\left(\frac{40}{RT}\right)\right] \qquad (5.57)$$

The resultant dislocation density is designated as $\boldsymbol{\rho_{exp}}$, since it is calculated using the k_{eff} value determined experimentally from the IC test analysis (Table 5.16).

Solving Eq. (5.57) at the current warm-forming temperature (*i.e.* 150°C) results in:

$$\rho_{exp}\ (150°\text{C}) = 6.8 \times 10^{12}\ m^{-2}$$

For the purpose of comparison, the above dislocation density, $\rho_{exp}\ (150°\text{C})$, is also shown in Figure 5.20. It is observed that there is a reasonable agreement between the value of dislocation density obtained from the model (Eq. (5.56)) and the value determined from the IC test analysis for $\epsilon = 10\%$. *i.e*: $\rho_{model} = 4.6 \times 10^{12}\ m^{-2}$ and $\rho_{exp} = 6.8 \times 10^{12}\ m^{-2}$.

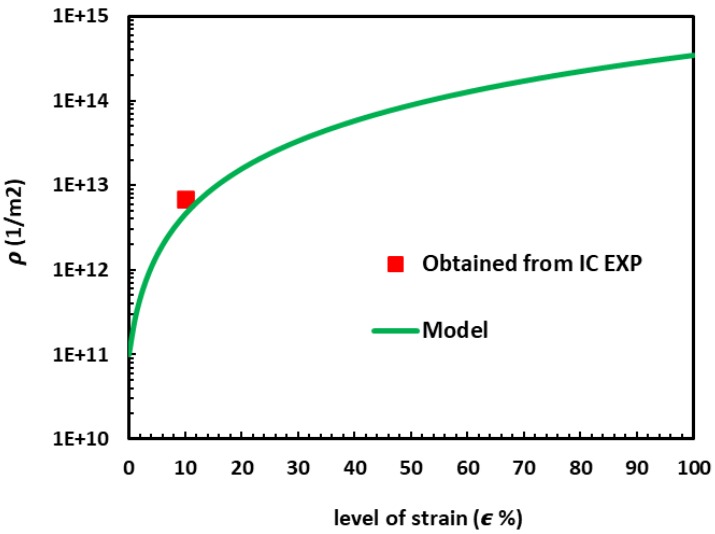

Figure 5.20. The evolution of dislocation density ρ with respect to the strain level according to model (Eq. (5.54)) and the experimental IC analysis.

5.3.3.3. Use of the modeled value of the dislocation density to calculate k_{eff}

In this section, the dislocation density ρ in the k_{eff} model, Eq. (5.50), is replaced by the value predicted through the model, Eq. (5.56), for the current warm-forming process (ϵ = 10%). Consequently, the values of k_{eff} obtained through the modeling equation (Eq. (5.50)) for various temperatures are implemented in the Arrhenius relationship (Eq. (5.38)) and the constant values of k_{0eff} and Q_{eff} are predicted. The modeling results of the parameters k_{eff}, Q_{eff} and k_{0eff} along with their respective values obtained through the IC tests (see

Table 5.16) are summarized in Table 5.20. The excellent agreement between the results suggests that the k_{eff} model, Eq. (5.50), with substitution of the dislocation density from the model, Eq. (5.56), can well predict the precipitation kinetics during such multi-step aging processes. Accordingly, it can be concluded that if the kinetic parameters of the PA and non-deformed material are available ($i.e.$ Q_v and k_{0v}), the kinetic parameters of Q_{eff} and k_{0eff} can be predicted for the deformed material without performing extra experimental tests on the PA+WF samples.

Table 5.20. The modeling and experimental values obtained for the k_{eff}, Q_{eff} and k_{0eff} for the current warm forming condition ($\epsilon = 10\%$) of AA7075.

	k_{eff} – IC experiment	**k_{eff} – Model Eq. (5.48)**
T = 150 °C	0.00043	0.00036
T = 165 °C	0.00069	0.00057
T = 177 °C	0.00098	0.00081
Note: $k_{eff} = k_{0eff} \times \exp(-Q_{eff}/RT)$		
Q_{eff} (kJ/mol)	48	48.3
k_{0eff} (1/s)	3.4×10^2	3.3×10^2

5.3.3.4. Use of the modeled value of k_{eff} to implement the kinetic model

Having the predicted values of k_{eff} (through Eq. (5.50)), Eq. (5.42) can be applied to model the evolution of f_r during the non-isothermal heat treatment and processing that was shown in Figure 3.2. The heat treatment process that is applied on the PA material is discretized to four steps of isothermal transformations:

(i) Fast heating from RT up to the warm forming temperature, *i.e.* 150°C (17 K/s).

(ii) Warm forming up to 10% plastic strain at 150°C (total time ~ 60s).

(iii) Air cooling to RT (0.7 K/s).

(iv) Artificial aging at 177 °C (by putting the PA+WF sample in the pre-heated furnace of 177°C).

For stage (i), the deformation process has not been started yet and the rate constant (k) in the f_r model should correspond to the non-deformed condition, *i.e.* k_v . However, once the deformation is started (stage (ii) and later), the rate constant should change to the effective value, *i.e.* k_{eff} (obtained from Eq. (5.50)), to account for the effect of dislocations on the precipitation reactions. It is worth mentioning that the dislocation density obtained through the model (Eq. (5.56)) for $\epsilon = 10\%$ is substituted in the k_{eff} model.

The modeling results for f_r, along with the experimental results obtained from the IC tests on the PA+WF AA7075 samples for three aging temperatures of 150, 165 and 177°C are shown in Figure 5.21. The comparison of the two results confirms their good agreement, with the exception of the earliest stage of the final artificial aging process.

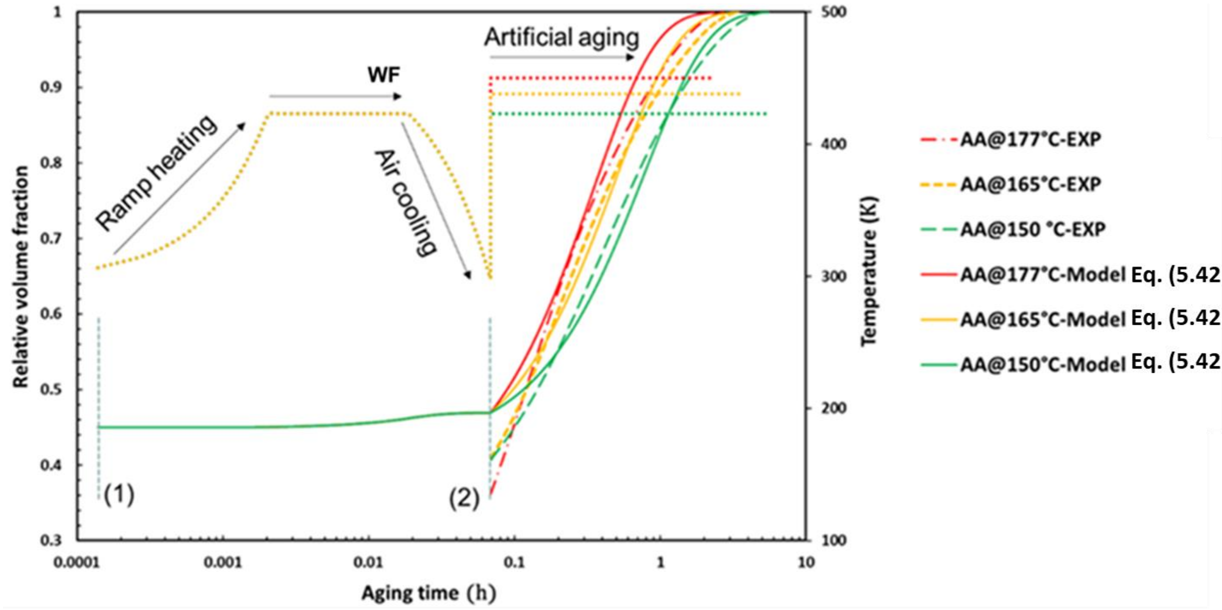

Figure 5.21. The comparison of the predicted and measured results of f_r during non-isothermal processing of AA7075, for three artificial aging temperatures of 150 °C, 165°C and 177°C (AA = artificial aging).

It can be inferred from the model predictions that the relative volume fraction of precipitates has slightly increased due to the warm-forming process, *i.e.* the f_r value has increased from 0.45 for the PA material, point (1), to ~ 0.47 for the PA+WF material, point (2). However, in all cases, the initial f_r values at the start of final artificial aging step in the experimental curves are smaller than those predicted by the models. This initial discrepancy between the results can be due to the following effects which are not considered in the model: (i) precipitate dissolution due to the change in aging temperature, *i.e.* from WF temperature (150°C) to the final artificial aging temperature (165 or 177°C), as was captured by SAXS measurements for the multi-step aging of AA7030 by Deschamps [96] (see Figure 5.10 (b)). This potential precipitate dissolution during early stages of the final artificial aging can be regarded as a strong possibility, since the initial difference between the predicted and measured values of f_r at 177°C is larger than that in 165°C, (ii) possible dissolution of some pre-aging zones during the warm-forming cycle and annihilation of the vacancy rich clusters (GP II zones). This dissolution effect has also been captured by the DSC and IC results shown in Figure 4.9 and Figure 5.17, respectively, (iii) potential dislocation recovery during WF and subsequent aging, and (iv) accelerated dynamic/static nucleation of precipitates in presence of dislocations.

5.4. Yield strength modeling for processing routes including a deformation step

5.4.1. Basic modeling approach

To model the yield strength of an artificially aged material with an intermediate deformation stage, in addition to the effect of dislocations on the precipitation kinetics, it is necessary to take into account the effect of strain hardening (σ_d) on the strengthening equation. Therefore, an appropriate superposition law is adopted to include the combined effects of σ_d and σ_{ppt} on the yield strength, σ_y. Accordingly, the general form of the yield strength equation is [5], [73]:

$$\sigma_y = \sigma_i + \sigma_{ss} + \left(\sigma_{ppt}^m + \sigma_d^m\right)^{1/m} \qquad (5.58)$$

where σ_{ss} and σ_{ppt} are the contributions of solid solution strengthening and precipitation hardening to the yield strength as defined by Eqs. (5.12) and (5.13), respectively. During the final aging of the PA+WF materials, it is assumed that the precipitates are grown enough to be considered as the strong obstacles. Using the strong obstacle assumption, C_1 is calculated by using the experimental yield strength data of the alloy at the peak aged condition:

$$C_1 = \sqrt[m]{(\boldsymbol{\sigma}_{y\,(peak)} - \boldsymbol{\sigma}_i)^m - \boldsymbol{\sigma}_d{}^m} \qquad (5.59)$$

σ_d is defined as [26,27,28,31]:

$$\sigma_d = \alpha_d M \mu b \rho^{1/2} \qquad (5.60)$$

in which, α_d is a constant of order 0.3, M is the Taylor factor (equal to 3.06 for fcc metals), μ is the shear modulus (25.4 GPa), b is the magnitude of the Burgers vector (0.286 nm) [5]. The dislocation density, ρ, is obtained through Eq. (5.56).

Although some authors have considered $m = 2$ in Eq. (5.58) [56], [72], generally the m value can vary between 1 and 2 [5]. Indeed, it is suggested that the exponent m equals 1 for shearable precipitates and increases to 2 for non-shearable precipitates [73]. Following Stolts and Pelloux [109], who suggested that the AA7075 in the T6 condition contains only shearable precipitates and non-shearable precipitates are only present in the over-aged condition, it is assumed here that $m = 1$. However, in some cases in which both shearable and non-shearable precipitates co-exist, the appropriate value for m falls between these two limits, *i.e.* $1 < m < 2$ [73]. It is also noted that if m is chosen as 1.5, the modeling results will not be significantly affected [5].

5.4.2. Implementation of the yield strength model

The experimental yield strength data for final aging of the PA+WF AA7075 at 177°C along with the predictions of the yield strength are shown in Figure 5.22. The model predictions are for the two sequential stages of warm-forming (at 150°C) and aging at 177°C. The predicted values of f_r obtained from Eq. (5.42) are substituted in Eqs. (5.12-5.13). Calibration parameters used for the model calculations are summarized in Table 5.21.

It is observed in Figure 5.22 that the modeling results slightly overestimate the experimental data. The maximum discrepancy between the modeling and the experimental results is about 3.5% which corresponds to 18 MPa. This error can be due to potential dislocation recovery that may occur during final aging at 177°C (recovery is not considered in the model).

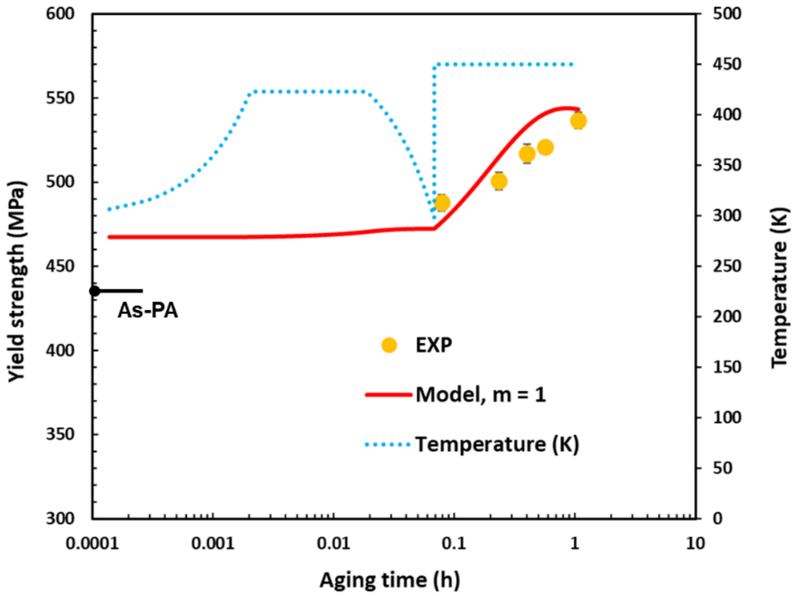

Figure 5.22. Comparison of modeling results using the strong obstacle assumption and the experimental values of yield strength during artificial aging of the PA+WF AA7075 at 177°C.

Table 5.21. The calibration parameters obtained for aging of the PA+WF AA7075 at 177℃.

Calibration Parameter	**Value**
σ_{0ss}	148 MPa [8]
C_1 (m =1)	513 MPa

5.5. Summary and concluding remarks

In this chapter, the precipitation kinetics of AA7050 alloy during direct and multi-step aging processes have been analyzed. A model for predicting the precipitate size evolution during the concurrent nucleation and growth of precipitates have been developed and validated. Consequently, a modified weak obstacle model has been introduced and validated.

The effects of deformation on the precipitation hardening kinetics of AA7075 have been studied. A kinetic model has been developed and validated for the warm-formed AA7075. The evolution of yield strength, as affected by the presence of dislocations, has been also predicted using these modeling techniques.

6. Conclusions and recommendations for future

6.1. Conclusions

The objectives of the present work were to: (i) evaluate the effects of various aging practices and deformation through an intermediate warm-forming stage, on the precipitation hardening response of AA7050 and AA7075, respectively; (ii) implement an existing kinetic model [2] to predict the precipitation kinetics of AA7050 upon various aging practices; (iii) expand the applicability of the weak obstacle (yield strength) model by developing a new model that predicts the evolution of precipitate radius as a function of the relative volume fraction of precipitates; (iv) expand the original kinetic model [2] to take into account the effect of dislocations on the precipitation kinetics, particularly in the context of warm forming and thus, model the yield strength evolution during the multi-step aging process coupled with a warm-forming stage.

The above objectives are met, and the important conclusions are summarized in the following subsections.

Effect of various heat treatments on age hardening - AA7050

The combination of hardness and calorimetry results of natural aging, direct-aging, and multi-step aging of AA7050 suggests the following findings:

- A prolonged natural aging process, *i.e.* up to 1-year, leads to the progressive formation of stable GP zones within the matrix which improves the hardening response of the material.
- The main precipitates that are formed during the artificial aging process, are most likely GP zones, η', and η precipitates. It is concluded that the combination of GP zones and η' precipitates are responsible for hardening up to the peak aged condition during artificial aging.
- During the direct aging process at the higher temperature of 177°C, the peak hardness is achieved earlier and has a smaller value compared to peak hardness for the lower temperature of 150°C. However, multi-step aging, *i.e.* final artificial aging of the pre-aged material at the temperatures of 150 and 177°C, results in a hardness comparable to the T6 hardness value (~ 186 HV). Indeed, the pre-aging process is beneficial for accelerated nucleation of higher amounts of η' during the final artificial aging treatment, particularly, for high temperatures such as 177°C.

- After artificial aging at the higher temperature of 177°C, the precipitates are larger and have a smaller volume fraction compared to those for the lower aging temperature of 150°C, for both direct and multi-step aging cases.
- The IC results for the as-quenched and the pre-aged materials suggest that the amount of total heat released (the area under the IC trace) is independent of the aging temperature and is substantially reduced for the pre-aged material compared to the as-quenched condition. This result shows that a considerable volume fraction of precipitates, *i.e.* GP zones, has been formed during the pre-aging process.

Effect of deformation on age hardening - AA7075

The combination of hardness and calorimetry results of the pre-aged and warm-formed (PA+WF) AA7075 material suggests the following findings:

- The increased hardness of the as-deformed material compared to the as-PA material is more likely due to the strain hardening effect caused by the generation of dislocations during the warm-forming stage. Also, potential dissolution of some pre-aging GP zones during the warm-forming stage may increase solid solution hardening contribution in the as-deformed material.
- The hardness values of the warm-formed material (PA+WF) are always higher than those for the non-deformed material (PA) during aging at 177°C. This result can be due to the combination of the remaining strain hardening (dislocation recovery will occur during aging at 177°C) and the improved precipitation hardening contribution in the PA+WF material due to the presence of dislocations.
- The peak hardening for both the PA and PA+WF materials is achieved after 1 hour of aging at 177°C. This similar peak aging time, which was also inferred from the IC test results, can be due to the offsetting factors that balance each other’s effects: The precipitation rate increases in the PA+WF material due to the (a) increased supersaturation of the matrix as a result of the GP zones dissolution during the warm-forming stage, and (b) presence of dislocations acting as favourable heterogeneous nucleation sites for precipitates. On the other hand, the presence of dislocations acting as vacancy sinks, leads to the reduction of vacancy concentration and decreases the precipitation rate in the PA+WF material. However, due to the faster growth and coarsening of precipitates on dislocations, the peak hardness reduces faster with aging time in the PA+WF material compared to the PA material.

Modeling analysis

- The kinetics of precipitation during direct and multi-step aging of AA7050 was studied using the IC test results and through implementing the previously developed kinetic models.
- The evolution of yield strength for the direct and multi-step aging processes is predicted through the linear addition of the contributions from precipitation hardening (considering weak and strong obstacle formulations), solid solution strengthening, and the intrinsic strength of the aluminum matrix.
- To implement the strong obstacle model, the only required variable is the relative volume fraction of precipitates, while to apply the weak obstacle model, knowledge of precipitate radius is required. Therefore, to expand the applicability of the weak obstacle formulation, a new model is developed (and validated) that predicts the precipitate size as a function of the relative volume fraction of precipitates. The developed model is described as the “Nucleation-affected growth” model. By implementing the new precipitate size model in the weak obstacle equation, a modified weak obstacle model is developed (and validated) which eliminates the need for knowledge of precipitate radius and is applicable to aging processes that are controlled by the concurrent nucleation and growth of precipitates.
- The modified weak obstacle model along with the strong obstacle model are implemented to predict the yield strength evolution during direct and multi-step aging of the current AA7050. According to the results, for the case of aging at 150°C of both as-quenched and pre-aged materials, the modified weak obstacle model has a better agreement with the experimental results compared to the strong obstacle model. In contrast, for the case of aging at 177°C, since the precipitates are larger, the experimental values of yield strength are better predicted by the strong obstacle model.
- Based on the theoretical descriptions of the effect of dislocation core diffusion on the precipitation kinetics, the original kinetic model is expanded to include the effect of dislocations (deformation) on the precipitation kinetics, particularly in the context of warm forming processes. Accordingly, a modeling relationship is developed that predicts the rate constant in the presence of dislocations, *i.e.* k_{eff}, as a function of the dislocation density and the rate constant in the absence of dislocations, *i.e.* k_v. Therefore, the necessity of performing IC tests on the PA+WF material is eliminated. In addition, a modeling relationship is developed that

predicts the dislocation density generated during the warm-forming process as a function of applied plastic strain.

- The new kinetic model is applied to the current AA7075 sheet to predict the evolution of f_r during the multi-step and non-isothermal process comprised of: ramp heating of the PA material to the WF temperature, warm forming, air cooling, and artificial aging at the temperatures in the range of 150-177°C. The good agreement between the predicted and measured values of f_r during the non-isothermal processing validates the modeling relationships.
- An appropriate superposition law is adopted to model the evolution of yield strength during the current multi-step and non-isothermal heat treatment of AA7075, considering final artificial aging at 177°C. The yield strength model includes the contributions from precipitation hardening, solid solution hardening, strain hardening, and the intrinsic strength of aluminum. The predicted values of f_r are implemented in the yield strength equations. The modeling and experimental results have a good agreement during final artificial aging of the PA+WF AA7075 at 177°C.
- Any discrepancies between the predicted and measured values of f_r and yield strength can be due to the factors that are not considered in the current modeling relationships, such as: (a) precipitate dissolution due to the change in aging temperature, *i.e.* from WF temperature to the final artificial aging temperature, (b) possible dissolution of some pre-aging GP zones during the warm-forming cycle and annihilation of the vacancy rich clusters (GP II zones), (c) potential dislocation recovery during WF and subsequent aging, and (d) accelerated dynamic/static nucleation of precipitates in presence of dislocations.

6.2. Recommendations for future work

- In the deformation-related modeling equations, the reduction of the strain hardening contribution due to dislocation recovery is neglected. In practice, the dislocation density gradually decreases as a result of the dislocation recovery that occurs due to exposure to high temperatures such as 177°C. A model should be developed to address this gradual decrease of the dislocation density as a function of the aging temperature.

- During the current warm-forming process, the strain rate has a pre-determined and constant value. The current modeling equations should be expanded to consider the variation in the strain rate during the warm-forming process.
- TEM analysis on the pre-aged and warm-formed materials will assist in improving our knowledge about the effects of dislocations on the precipitate microstructure, number density and distribution.

7. References

[1] S. Esmaeili, D. J. Lloyd, and W. J. Poole, *Acta Materialia*, 51, 2003, 2243–2257.

[2] S. Esmaeili and D. J. Lloyd, *Acta Materialia*, 53, 2005, 5257–5271.

[3] Y. B. J.C. Werenskiold, A. Deschamps, *Materials Science & Engineering A*, 293, 2000, 267–274.

[4] P. Guyot and L. Cottignies, *Acta Materialia*, 44, 1996, 4161–4167.

[5] L. M. Cheng, W. J. Poole, J. D. Embury, and D. J. Lloyd, *Metallurgical and Materials Transactions A: Physical Metallurgy and Materials Science*, 34 A, 2003, 2473–2481.

[6] G. Waterloo, V. Hansen, J. Gjønnes, and S. R. Skjervold, *Materials Science & Engineering A*, 303, 2001, 226–233.

[7] C. Cao, D. Zhang, L. Zhuang, and J. Zhang, *Journal of Alloys and Compounds*, 691, 2017, 40–43.

[8] K. Omer, A. Abolhasani, S. Kim, *et al.*, *Journal of Materials Processing Technology*, 257, 2018, 170–179.

[9] Y. S. Lee, D. H. Koh, H. W. Kim, and Y. S. Ahn, *Scripta Materialia*, 147, 2018, 45–49.

[10] M. Tajally and E. Emadoddin, *Materials & Design*, 32, 2011, 1594–1599.

[11] M. Kumar and N. G. Ross, *Advances in Materials Science and Engineering*, 2017, 1–10.

[12] M. Kumar, N. Sotirov, and C. M. Chimani, *Journal of Materials Processing Technology*, 214, 2014, 1769–1776.

[13] J. A. Österreicher, M. A. Tunes, F. Grabner, *et al.*, *Materials and Design*, 193, 2020, 108837.

[14] A. Deschamps and Y. Bréchet, *Scripta Materialia*, 39, 1998, 1517–1522.

[15] A. Deschamps, G. Fribourg, Y. Bréchet, J. L. Chemin, and C. R. Hutchinson, *Acta Materialia*, 60, 2012, 1905–1916.

[16] A. Deschamps, F. Livet, and Y. Bréchet, *Acta Materialia*, 47, 1998, 281–292.

[17] A. Deschamps, Y. Bréchet, P. Guyot, and F. Livet, *Zeitschrift fuer Metallkunde/Materials Research and Advanced Techniques*, 88, 1997, 601–606.

[18] A. Deschamps, F. Bley, F. Livet, D. Fabregue, and L. David, *Philosophical Magazine*, 83, 2003, 677–692.

[19] E. Pink and W. M. Webernig, *Acta Metallurgica*, 35, 1987, 127–132.

[20] C. R. Hutchinson, *Modeling the kinetics of precipitation in aluminium alloys*. 2010.

[21] G. E. Dieter, D. Bacon, and G. L. Wilkes, *Mechanical Metallurgy*. 1988.

[22] R. Abbaschian, L. Abbaschian, and R. E. Reed-Hill, *Physical metallurgy principles*. 2009.

[23] A. K. Vasudevan and R. D. Doherty, *Aluminum Alloys: Contemporary Research and Applications*. 1989.

[24] K. Ma, T. Hu, H. Yang, *et al.*, *Acta Materialia*, 103, 2016, 153–164.

[25] R. P. Carreker and W. R. Hibbard, *Met. Trans. A*, 209, 1957, 1157.

[26] H. R. Shercliff and M. Ashby, *Acta Metallurgica et Materialia*, 38, 1990, 1803–1812.

[27] H. Mecking and U. F. Kocks, *Acta Metallurgica*, 29, 1981, 1865–1875.

[28] T. Gladman, *Materials Science and Technology*, 15, 2004, 30–36.

[29] R. R. Ambriz and D. Jaramillo, "Mechanical Behavior of Precipitation Hardened Aluminum Alloys Welds," in *Light Metal Alloys Applications dissolution*, 2014, 35–59.

[30] A. J. Ardell, *Metallurgical Transactions A*, 16, 1985, 2131–2165.

[31] O. Wouters, "Dislocations and Precipitation Hardening," in *Plasticity in Aluminum Alloys at Various Length Scales*, 2006, 25–48.

[32] S. Esmaeili, "Precipitation Hardening Behaviour of Aa6111," 2002.

[33] J. Chen, L. Zhen, S. Yang, W. Shao, and S. Dai, *Materials Science and Engineering A*, 500, 2009, 34–42.

[34] V. Hansen, O. B. Karlsen, Y. Langsrud, and J. Gjønnes, *Materials Science and Technology*, 20, 2004, 185–193.

[35] J. Buha, R. N. Lumley, and A. G. Crosky, *Materials Science and Engineering A*, 492, 2008, 1–10.

[36] J. M. Papazian, *Metallurgical Transactions A*, 13, 1982, 761–769.

[37] W. Yang, S. Ji, M. Wang, and Z. Li, *Journal of Alloys and Compounds*, 610, 2014, 623–629.

[38] P. K. Rout, M. M. Ghosh, and K. S. Ghosh, *Materials Characterization*, 104, 2015, 49–60.

[39] G. Sha and A. Cerezo, *Acta Materialia*, 52, 2004, 4503–4516.

[40] G. Sha and A. Cerezo, *Surface and Interface Analysis*, 36, 2004, 564–568.

[41] L. K. Berg, J. Gjoønnes, V. Hansen, *et al.*, *Acta Materialia*, 49, 2001, 3443–3451.

[42] M. H. Li, Y. Q. Yang, Z. Q. Feng, *et al.*, *Transactions of Nonferrous Metals Society of China (English Edition)*, 24, 2014, 2061–2066.

[43] Z. Li, B. Xiong, Y. Zhang, B. Zhu, F. Wang, and H. Liu, *Materials Characterization*, 59, 2008, 278–282.

[44] J. X. Zang, K. Zhang, and S. L. Dai, *Transactions of Nonferrous Metals Society of China (English Edition)*, 22, 2012, 2638–2644.

[45] J. F. Chinella and Z. Guo, *Materials Science*, 2011.

[46] C. B. Fuller, M. W. Mahoney, M. Calabrese, and L. Micona, *Materials Science and Engineering A*, 527, 2010, 2233–2240.

[47] J. T. Staley, *Metall Trans*, 5, 1974, 929–932.

[48] S. Esmaeili, D. J. Lloyd, and W. J. Poole, *Acta Materialia*, 51, 2003, 3467–3481.

[49] H. Loffler, I. Kovacs, and J. Lendvai, *Journal of Materials Science*, 18, 1983, 2215–2240.

[50] S. V. Emani, J. Benedyk, P. Nash, and D. Chen, *Journal of Materials Science*, 44, 2009,

6384–6391.

[51] W. J. Poole, J. A. Seter, S. Skjervold, and G. Waterloo, *Metallurgical and Materials Transactions A: Physical Metallurgy and Materials Science*, 31, 2000, 2327–2338.

[52] A. Deschamps and Y. Bréchet, *Materials Science and Engineering: A*, 251, 1998, 200–207.

[53] D. A. Porter, K. E. Easterling, and M. Sherif, *Phase Transformations in Metals and Alloys*. CRC press, 2009.

[54] S. Ceresara and P. Fiorini, *Materials Science and Engineering*, 10, 1972, 205–210.

[55] D. Wang and Z. Y. Ma, *Journal of Alloys and Compounds*, 469, 2009, 445–450.

[56] A. Deschamps and Y. Brechet, *Acta Materialia*, 47, 1998, 293–305.

[57] J. Mittra, U. D. Kulkarni, and G. K. Dey, *Materials Science and Engineering A*, 500, 2009, 244–247.

[58] P. Sepehrband and S. Esmaeili, *Materials Science and Engineering A*, 487, 2008, 309–315.

[59] D. H. Bratland, Grong, H. Shercliff, O. R. Myhr, and S. Tjøtta, *Acta Materialia*, 45, 1997, 1–22.

[60] J.W.Christian, *The Theory of Transformations in Metals and Alloys*. 1959.

[61] W. A. Johnson and R. F. Mehl, *Trans AIME*, 135, 1939, 416.

[62] J. C. Avrami, *The Journal of chemical physics*, 7, 1939, 1103.

[63] A. N. Kolmogorov, *Izv. Akad. Nauk. USSR. Ser. Math.*, 1, 1937, 355.

[64] M. J. Starink, *Journal of Materials Science*, 32, 1997, 4061–4070.

[65] P. G. Boswell, *Journal of Thermal Analysis*, 18, 1980, 353–358.

[66] J. A. Augis and J. E. Bennett, *Journal of Thermal Analysis*, 13, 1978, 283–292.

[67] B. Rheingans and E. J. Mittemeijer, *The Journal of The Minerals*, 65, 2013, 1145–1154.

[68] O. Djema, M. Bouabdallah, R. Badji, A. Saadi, N. Kherrouba, and A. Sahli, *Materials Chemistry and Physics*, 240, 2020, 122073.

[69] R. Badji, N. Kherrouba, B. Mehdi, *et al.*, *Materials Chemistry and Physics*, 148, 2014, 664–672.

[70] A. Khalfallah, A. A. Raho, S. Amzert, and A. Djemli, *Transactions of Nonferrous Metals Society of China (English Edition)*, 29, 2019, 233–241.

[71] S. Esmaeili, X. Wang, D. J. Lloyd, and W. J. Poole, *Metallurgical and Materials Transactions A: Physical Metallurgy and Materials Science*, 34, 2003, 751–763.

[72] O. R. Myhr, Ø. Grong, and C. Schäfer, *Metallurgical and Materials Transactions A: Physical Metallurgy and Materials Science*, 46, 2015, 6018–6039.

[73] F. Fazeli, W. J. Poole, and C. W. Sinclair, *Acta Materialia*, 56, 2008, 1909–1918.

[74] W. J. Poole, X. Wang, D. J. Lloyd, and J. D. Embury, *Philosophical Magazine*, 85, 2005, 3113–3135.

[75] J. K. Park and A. J. Ardell, *Metallurgical Transactions A*, 14, 1983, 1957–1965.

[76] Y. Zou, L. Cao, X. Wu, Y. Wang, and X. Sun, *Journal of Alloys and Compounds*, 823, 2020, 153792.

[77] ASTM Standard E1097-1, *ASTM International*, 2012.

[78] H. Pishyar, S. DiCecco, and Michael Worswick, "38th International Deep Drawing Research Group Annual Conference (IDDRG 2019)."

[79] Z. Jis, *Japanese Standards Association*, 2011.

[80] Hossein Pishyar, "MASc Thesis, University of Waterloo, in preparation, 2021."

[81] M. Di Ciano, S. DiCecco, S. Esmaeili, M. A. Wells, and M. J. Worswick, *Journal of Materials Engineering and Performance*, 27, 2018, 939–947.

[82] Y. Liu, W. Li, and D. Jiang, *Journal of Materials Research*, 30, 2015, 3803–3810.

[83] O. N. Senkov, S. V. Senkova, and M. R. Shagiev, *Metallurgical and Materials*

Transactions A: Physical Metallurgy and Materials Science, 39 A, 2008, 1034–1053.

[84] A. Abolhasani, S. Esmaeili, M. Wells, and M. Worswick, *Unpublished results, 2021*.

[85] X. Fan, D. Jiang, Q. Meng, Z. Lai, and X. Zhang, *Materials Science and Engineering A*, 427, 2006, 130–135.

[86] Z. Li, B. Xiong, Y. Zhang, B. Zhu, F. Wang, and H. Liu, *Materials Characterization*, 59, 2008, 278–282.

[87] The Al-Zn (Aluminum-Zinc) System, 4, 1983, 55–73.

[88] M. Y. Lee, S. M. Sohn, C. Y. Kang, D. W. Suh, and S. Y. Lee, *Journal of Materials Processing Technology*, 155–156, 2004, 1337–1343.

[89] R. Ferragut, A. Somoza, and I. Torriani, *Materials Science and Engineering A*, 334, 2002, 1–5.

[90] A. Abolhasani, *PhD Thesis, University of Waterloo, in preparation, 2021*.

[91] M. B. Berkenpas, J. A. Barnard, R. V Ramanujan, H. I. Aaronson, and T. B. Equations, 20, 1986, 323–328.

[92] S. Esmaeili, D. Vaumousse, M. W. Zandbergen, W. J. Poole, A. Cerezo, and D. J. Lloyd, *Philosophical Magazine*, 87, 2007, 3797–3816.

[93] R. C. Picu and D. Zhang, *Acta Materialia*, 52, 2004, 161–171.

[94] D. S. MacKenzie, “Quench rate and aging effects in aluminum-zinc-magnesium-copper aluminum alloys”, University of Missouri, 2000.

[95] A. Deschamps, Y. Bréchet, and F. Livet, *Materials Science and Technology*, 15, 2013, 993–1000.

[96] A. Deschamps, *Unpublished results*, 2007.

[97] G.E. Totten, D. S. MacKenzie, (Eds.) , *Alloy Production and Materials Manufacturing, Marcel Dekker, Incorporated*, 2, 2003, 155–192.

[98] P. Sepehrband and S. Esmaeili, *Unpublished results*, 2007.

[99] J. D. Robson, *Metallurgical and Materials Transactions A*, 51, 2020, 5401–5413.

[100] R. E. Hoffman, D. Turnbull, and E. W. Hart, *Acta Materialia*, 3, 1955, 417.

[101] H. J. Frost and M. F. Ashby, *Deformation mechanism maps: the plasticity and creep of metals and ceramics*. Pergamon press, 1982.

[102] M. Gholamirad, S. Soltani, and P. Sepehrband, *Microelectronics Reliability*, 81, 2018, 210–217.

[103] S. Soltani, N. Abdolrahim, and P. Sepehrband, *Scripta Materialia*, 133, 2017, 101–104.

[104] Y. Chen, Y. Yang, Z. Feng, *et al.*, *Materials Characterization*, 123, 2017, 189–197.

[105] J. Yao, Y. W. Cui, H. Liu, H. Kou, J. Li, and L. Zhou, *Calphad: Computer Coupling of Phase Diagrams and Thermochemistry*, 32, 2008, 602–607.

[106] W. J. Poole, H. R. Shercliff, and T. Castillo, *Materials Science and Technology*, 13, 1997, 897–904.

[107] M. F. Ashby, *Philosophical Magazine*, 21, 1970, 399–424.

[108] O. R. Myhr, Ø. Grong, and C. Schäfer, *Metallurgical and Materials Transactions A: Physical Metallurgy and Materials Science*, 46, 2015, 6018–6039.

[109] R. E. Stoltz and R. M. Pelloux, *Metallurgical Transactions A*, 7, 1976, 1295–1306.